THE UNIVERSITY OF
SYDNEY

THE FABRICATION AND APPLICATIONS OF CARBON NANOTUBE-BASED HYBRID NANOMATERIALS

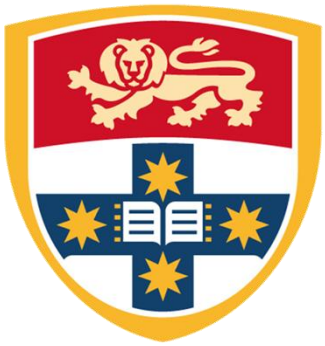

A thesis submitted in fulfilment of the requirements for the completion of a Doctor of Philosophy in Physics at The University of Sydney.

Samuel King Lok Yick

School of Physics,

Faculty of Science,

The University of Sydney

2014

Statement of Student Contribution

I certify that this thesis contains original research carried out by myself except where otherwise acknowledged.

Signature: ……..

Samuel King Lok Yick

Date: ……

Abstract

The evolution of technology has reached a stage where the performances and dimension needed are outpacing what conventional materials can deliver. This has been made more acute with the further necessity of miniaturisation. Therefore, new materials which can overcome this bottleneck are required. Over the past few decades, it was found that when a material is reduced to the nanoscale, they can exhibit properties unparallel by their bulk counterparts. Therefore these nanomaterials poise as a promising candidate for future applications.

Of the many nanomaterials, carbon nanotube (CNT) is among the most emblematic. CNT is a hollow one-dimensional structure comprising solely of carbon atoms in a graphitic lattice. They are fascinating as they exhibit physical attributes which surpass many conventional materials and their nanoscale dimension allows greater flexibility in their deployments. However, the utilisation of CNTs is currently frustrated by a host of intrinsic and extrinsic factors. These include chirality dependent behaviours and the inability to impose deterministic growth, difficulties in integrating CNTs into device applications, and the cytotoxicity of CNTs. As a result, there are usually significant disparity between their predicted capability and real-world performance. Therefore, the practical application of CNTs remains unfeasible.

The premise of this thesis is that by employing CNTs in conjunction with other materials, the problems which plague their utilisation may be overcome. Here, the concept of CNT-based hybrid nanomaterials is presented. The aim of this work is to look beyond merely placing CNTs in physical proximity with other materials but to control their coupling so that synergistic interactions can occur.

In specific, the thesis will cover the following,

1) Controlling the physical properties of as-grown single-walled CNT networks
2) Fabrication of a CNT-metal core-shell structure and their application in resistive-based hydrogen sensing

3) Mask-less patterning and the fabrication of plasmonic sensor from on gold decorated CNT arrays
4) Direct growth of CNT on graphene nanostructures for energy storage application
5) Studying the effects of plasma treatment on the biocompatibility of CNT arrays

These topics will be covered in separate chapters where I will first outline the problems faced by CNTs in the related fields and then offer solutions backed by experimental results to these issues. Most of these chapters are based on articles which I had authored and have already been published in peer-reviewed journals.

This thesis demonstrates that by engineering complementary interaction between two materials, many challenges which hamper the utilisations of CNTs and other nanomaterials can indeed be negated. Furthermore, their synergistic interaction allows the performance of the CNT-based hybrid nanomaterials to be superior to their uncoupled precursors. Therefore, this could be a viable strategy to incorporating nanomaterials in a range of applications.

Acknowledgement

As I reflected upon my academic journey, I realised that this experience was not as solitary as I often ascribe it to be. Throughout my postgraduate study, there are many people who had contributed in various capacities. Therefore, I would like to express my thanks. For without them, I doubt I would be where I am today.

I would like to thank my academic supervisor, Professor Kostya (Ken) Ostrikov for his tutorage and support over my doctoral candidature. I am blessed for the opportunity to interact and learn from a man who possesses such an immense passion for science. To Dr Zhao Jun Han, my utmost thanks to you. I am grateful for your guidance, advices and for being my mentor. Thank you for shaping my scientific approach and teaching me the skills needed in scientific communication. I sincerely appreciated your patience over the years and your thoroughness in critiquing my work.

I was fortuitous to be part of a wonderful research group who had consistently challenged and encouraged me. To my office companions Dr Amanda Rider and Mr Dong Han (Michael) Seo, I appreciate our many discussions (both scientific and otherwise) and joint research ventures. To the other members of the group, Dr Igor Levchenko, Dr Shailesh Kumar, Dr Jinghua Fang, Dr Massoud Aghili, Dr Winston Yan, Mr Timothy van-der Laan and Mr Fabricio Borghi thank you for the many helpful conversations. Beyond my immediate group, I would also acknowledge other members of CSIRO who I had the opportunities to interact with and learn from. Thus, I would like to acknowledge Dr Cathy Foley, Dr Tony Murphy, Dr Avi Bendavid, Dr Tristan Temple, and Dr Murali Venkatraman. It was a true blessing to be among such innovative and devoted professional.

To the University of Sydney, I would like to acknowledge their financial provision through the University Postgraduate Award and the Postgraduate Research Support Scheme. I would like to further thank Professor Iver Cairns for being my co-supervisor.

To my Father, Ping Chuen Yick; mother, Kitty Yick; and sister, Sarah Yick, words fail to express the extent of my gratitude for all that you had done. Thank you for your patience over the years and for the constant physical, emotional and spiritual support.

To my Christian brothers and sisters from West Sydney Chinese Christian Church, Summerhill Anglican Church and Postgraduate Bible Fellowship, thank you for your ceaseless prayers and acceptance of me despite of my constant urge to go on strange scientifically fuelled tangents.

Lastly, thanks, praises, and glory to God the creator. As I ventured into the realms of electrons, atoms, and molecules, I continue to see your wisdom and magnificent. I do at times wish that you had made the world in a simpler fashion though. (Perhaps I might have a fuller head of hair then) Thank you for creating humanity with a sense of curiosity and a thirst for knowledge. Most of all, thank you for revealing yourself to us through Jesus Christ. From whom, the purpose of creation can be understood.

Table of Contents

List of Figures

List of Publications and Presentations

Papers included in the thesis

1) D.H Seo, S. Yick, Z. J. Han and K. Ostrikov, *Synergistic Fusion of Vertical Graphene Nanosheets and Carbon Nanotubes for High Performance Supercapacitor Electrodes*, ChemSusChem, (2014) 7, 8, 2317
   (S.Yick and D.H Seo contributed equally to this work)

2) S. Yick, Z. J. Han and K. Ostrikov, *Controlled Growth of Single-Walled Carbon Nanotube Networks by Catalyst Interfacial Diffusion,* Advanced Materials Interface, (2014), 1, 1300151

3) S. Yick, M. M. A Yajadda, A. Bendavid, Z. J. Han and K. Ostrikov, *Physisorption-induced electron scattering on the surface of carbon-metal core-shell nanowire arrays for hydrogen sensing,* Applied Physics Letters, (2013) 102, 233111

4) S. Yick, Z. J. Han and K. Ostrikov, *Atmospheric microplasma-functionalized 3D Microfluidic strips within dense carbon nanotube arrays confine Au nanodots for SERS sensing*, Chemical Communications, (2013) 49, 28, 2861
   (The issue included a cover image based on our publication which I had designed upon an invitation from the publisher)

Relevant Papers not included in the thesis

1) A. Kondyurin, I. Levchenko, Z.J. Han, S. Yick, A. Mai-Pronchnow, J. Fang, K. Ostrikov and M.M.M Bilek, *Hybrid graphite film – carbon nanotube platform for enzyme immobilization and protection*, Carbon, (2013) 65, 287

2) W. Cher, S. Yick, S. Xu, Z. J. Han, K. Ostrikov, *Structural, optical and electrical properties of Al-doped ZnO transparent conducting oxide for solar cell applications*, Functional Materials Letters, (2011), 4, 401.

3) S.Yick, Z.J. Han, K. Ostrikov, *Control of Density of self-organized carbon nanotube arrays by catalyst pretreatment through plasma immersion ion implantation*, Journal of Applied Physics, (2011), 110, 094303

4) Z. J. Han, I. Levchenko, S. Yick, K. Ostrikov, *3-order-of-magnitude density control of single-walled carbon nanotube networks by maximizing catalyst activation and dosing carbon supply*, Nanoscale, (2011), 3, 4848

5) S. Yick, I. Levchenko, S. Kumar, Z. J. Han, M. M. A. Yajadda, and K. Ostrikov, *Current Control in the Magnetron Systems for Nanofabrication: a Comparison,* IEEE Transactions on Plasma Science, (2011), 40, 4, 1094

6) Z. J. Han, S. Yick, I. Levchenko, E. Tam, M. M. A. Yajadda, S. Kumar, P. J. Martin, S. Furman and K. Ostrikov, *Controlled synthesis of a large fraction of metallic single-walled carbon nanotube and semiconducting carbon nanowire networks*, Nanoscales, (2011), 3, 3214

7) K. Ostrikov, S. Kumar, Q. J. Cheng, A. Rider, M. M. A. Yajadda, Z. J. Han, D. H. Seo, Tim van der Laan, S. Yick, E. Tam, I. Levchenko, *Different Nanostructures from Different Plasmas: Nanoflowers and Nanotrees on Silicon*, IEEE Transactions on Plasma Science, (2011), 39, 11, 2796

8) Z. J. Han, I. Levchenko, S. Kumar, M. M. A. Yajadda, S. Yick, D. H. Seo, P. J. Martin, S. Peel, Z. Kuncic and K. Ostrikov, *Plasma nanofabrication and nanomaterials safety*, Journal of Physics D: Applied Physics (2011), 44, 174019

Conference Presentations

1) Samuel Yick, Zhao Jun Han and K.Ostrikov (2010):
iPlasma-Nano- II, 12 – 15th December 2010, Murramarang Resort, Batemans Bay, New South Wales, Australia

2) Samuel Yick, Zhao Jun Han and K.Ostrikov (2011):
AIP Industry Day, 10th November 2011, CSIRO Material Science and Engineering, Lindfield, Sydney, New South Wales, Australia

3) Samuel Yick, Zhao Jun Han and K.Ostrikov (2012):
ICONN2012, 5-9th February 2012, Perth Convention and Exhibition Centre, Perth, Western Australia, Australia

4) Samuel Yick. Zhao Jun Han and K.Ostrikov (2012):
NT12: 12th International Conference on the Science and Application of Nanotubes, 24-29th June 2012, Brisbane Convention and Exhibition Centre, Australia

5) Samuel Yick, Michael Seo, Zhao Jun Han and Kostya (Ken) Ostrikov (2013):
A IP Physics in Industry Day, 7th November 2013, CSIRO Material Science and Engineering, Lindfield, Sydney, New South Wales, Australia

6) Samuel Yick, Michael Seo, Zhao Jun Han and Kostya (Ken) Ostrikov (2013):
New Horizons Collaborative Workshop, 21st November 2013, Monash University, Melbourne, Victoria, Australia

List of Acronyms and Abbreviations

Although all acronyms and abbreviations are defined where they first appeared, for ease of reading a list is provided here as well.

1D	One-Dimensional
2D	Two-Dimensional
3D	Three-Dimensional
4-ATP	4-Aminothiophenol
AFM	Atomic Force Microscope/Microscopy
APMPJ	Atmospheric-Pressure Microplasma Jet
B.subtilis	Bacillus subtilis
BE	Binding Energy
cfu	Colony Forming Units
CNT	Carbon Nanotube
CPD	Critical Point Drying
CVD	Chemical Vapour Deposition
CV	Cyclic Voltammetry
D-peak	Defect Induced Peak
E. coli	Escherichia coli
EDL	Electrical Double-Layer
EDS	Energy- Dispersive X-Ray Spectroscopy
EIS	Electrochemical Impedance Spectroscopy
FE-SEM	Field Emission Scanning Electron Microscope/Microscopy
FWHM	Full Width Half Maximum
G-peak	Graphitic Peak
ICP	Inductively-Coupled Plasma
m-SWCNT	Metallic Single-Walled Carbon Nanotubes
nm	Nanometre
PBS	Phosphate Buffered Saline
PECVD	Plasma Enhanced Chemical Vapour Deposition
PPMS	Physical Property Mesurement System

RBM	Radial Breathing Mode
ROS	Reactive Oxygen Species
sccm	Standard Cubic Centimetre per Minute
SERS	Surface-Enhanced Raman Scattering
SN	Supernatant
s-SWCNT	Semiconducting Single-Walled Carbon Nanotubes
SWCNT	Single-Walled Carbon Nanotube
TCVD	Thermal Chemical Vapour Deposition
TEM	Transmission Electron Microscope/Microscopy
VGNS	Vertical Graphene Nanosheets
XPS	X-ray Photoelectron Spectroscopy

1

Introduction

From the fantastical materials which can construct a future of bionics and towering space elevators to a "grey goo" apocalypse bring forth by sentinel nanomachinaries, the concepts of nanoscience and its application in nanotechnology continue to intrigue the imaginations of many.[1,2] Nanoscience is more than just a plot device for science-fictions or a wild fantasy of a projected future. From the quantities of high impact journals dedicated to nanoscience and the abundances of high quality peer-reviewed scientific publications regarding this topic, it is clear that the topic of nanoscience and nanotechnology are being actively engaged by the academic community.

Why are there such fascinations with nanoscience though? In 1959, R. Feynman addressed the American Physical Society with the now famous presentation "*There's plenty of room at the bottom*". This talk, retrospectively associated with initiating the field of nanoscience suggested the possibility of utilising materials with dimensions comparable to the world of molecules and atoms for applications. At such sizes, he expects *"atoms on a small scale behave like nothing on a large scale, for they satisfy the laws of quantum mechanics"*.[3] Thus, materials constructed at this scale can exhibit properties otherwise unobtainable. He asked the question, *"what would the properties of materials be if we could really arrange the atoms the way we want them?"*.[3] Ultimately, the incentives which drives our endeavour in the field of nanoscience lay with the possibilities that achieving precise control over the interactions between atoms and molecules can deliver. Despite the fifty-five years which had since lapsed, the question posed by R. Feynman still serves as the underlying query in the pursuit of nanoscience.

What though is nanoscience? At what point does a bulk material transition into a nanomaterial in which their properties reflect or become relevant to nanoscience? In order to understand this thesis, it is prudent to have a clear concept about what makes up the "nano" portion of nanomaterials. Nanomaterials can be defined as materials where the characteristic length scale (i.e. diameter, grain size, layer thickness, *etc*) is less than about a hundred nanometres ($\leq 10^{-7}$ m).[4] This serves as a useful demarcation, for then the characteristic length scale of the nanomaterial becomes comparable to the bond lengths and atomic radii (typically on the order of 10^{-10} m). At this regime, quantum effects and the large fraction of surface atoms can exert strong influence to the intrinsic behaviours of the material. The utilisation of nanomaterials had demonstrated their potential for both applied and fundamental science. For example, the utilisation of nanostructure had enabled the creation of self-cleaning hydrophobic surface, whereas recent work on single-atom transistors is an example of the latter.[5,6] These and many other examples demonstrate the benefit of incorporating nanoscience in various fields of study. Thus, there are strong interests in fabricating and utilising materials with nanoscale dimensions.

This thesis aims to present the research which I, the author had conducted in the field of nanoscience. In particular, this work looks at two things, the coupling of carbon nanotubes (CNTs) with other nanomaterials to form hybrid nanostructures and also their implementation into various applications. At this point, one might question why I had chosen to focus on the coupling of CNTs with other nanomaterials when there remain unsolved challenges within the field of CNTs. Is it not prudent for one to first solve those issues before considering their combination with other materials? It is true that challenges remain within the field of CNTs; in fact this is true for all the nanomaterials presented in this work. However in my struggle to overcome these problems, I thought of a near eastern saying, "*Two are better than one, because they have a good reward for their toil; for if they fall, the other will lift up his fellow*."[7] This describe a simple observation about the human condition; individuals benefit from being in communities because of mutual support. By

working in concert, the expertise of an individual can augment and enhance the performance of the community. Similarly, complementary interaction can also be beneficial in nanoscience. Ultimately, every nanomaterial possesses limitations induced from both extrinsic and intrinsic factors. Yet, by using nanostructures in concert, the shortcoming of one can be negated via the attribute of another. Furthermore, their combination can be engineered so that additional ability maybe imparted. Therefore, the creation of hybrid-CNTs allows better control over the material's attributes and opens up new avenues to understand CNTs and how they can be utilised. Thus, the author believes that hurdles which currently prevent the utilisation of CNTs may be solved or circumvented through their combination with other nanomaterials.

A group in MIT recently demonstrated the beneficial influence of a CNT-based hybrid. In their work, the process of photosynthesis was enhanced *in vivo* via the coupling of biomolecules with CNTs. Photosynthesis is the bedrock of life, it allows light to be converted into chemical energy and oxygen to be produced. However, the fact that plant can only utilise the visible spectrum of light limits their efficiency. It was shown that photosynthesis can be augmented by inserting semiconducting CNTs into chloroplast. This enhancement was due to CNTs' broad absorption spectrum which extended the usable wavelengths from ultraviolet to infrared.[8] Thus, this illustrates the benefit of complementary interaction in nanoscience. By working in concert, the performance of the CNT-hybrid was superior to its original as the innate shortcoming of the biological system was compensated by the attributes of the CNTs.

However, prior to discussing CNT based hybrid nanomaterials, it is necessary to briefly introduce the concept of CNT and the origins of their physical properties. Therefore, the remainder of this chapter will be devoted to discussing what CNT is and why they have been the darling of the nanoscience community for the past two decades. The chapter will conclude with an executive summary, specifying the areas which my research had covered and an outline of the remaining chapters.

1.1 Carbon Nanotubes

Since their discovery, CNTs with their nanoscale diameter, structural dependant characteristics and self-assembled growth have become emblematic with nanoscience. The discovery of CNTs is commonly attributed to Iijima with his 1991 publication in the journal *Nature*.[9] Though reports dated since 1952 regarding hollow one dimensional carbon nanostructures have been published,[10] his paper showcased many characteristic features of CNTs which delivered insight to both its morphology and compositions.[11] These features included both the resolved graphitic walls and the hollow cavity obtained from transmission electron microscopy (TEM). Furthermore, he used electron diffraction to demonstrate the lattice orientation of the graphitic walls and variability to the number of walls which the structure can be comprised of. These are shown in Figure 1.1a. Two years after this work, two publications which reported on the fabrication and characterisation of single-walled CNTs were concurrently published by *Nature*.[12,13] Apart from demonstrating the growth of a single-walled tubular structure shown in Figure 1.1b, these papers also speculated on the influence which the graphitic morphology can exerted onto the energy band structure of the tubes. These findings demonstrated the ability to experimentally fabricate one dimensional carbon nanostructures, tune their properties via their structure and postulated their properties for a range of applications. As a result, interests in CNTs began in earnest and had since thrived in both fundamental studies and commercial applications.[14]

Yet, what are carbon nanotubes? In their nomenclature, two aspects namely; their composition and morphology are used to define what constitute a CNT. From their name, it is obvious that CNT is a hollow one dimensional nanostructure composed of carbonaceous materials. More precisely, the carbon atoms within this structure are arranged into a one atom thick hexagonal lattice. This planar carbon structure is seamlessly joined to form tubular side walls and terminating end-caps. In order for such a hexagonal arrangement to occur, the carbon atoms are joined exclusively via sp^2 bonding, identical to the atomic ordering of graphite, graphene and fullerene. From this, it is evident that

CNTs are comprised of graphitic carbon in a tubular orientation. Therefore, carbon atoms which are not in such an arrangement and the presence of foreign elements will cause perturbation to the properties of CNTs.

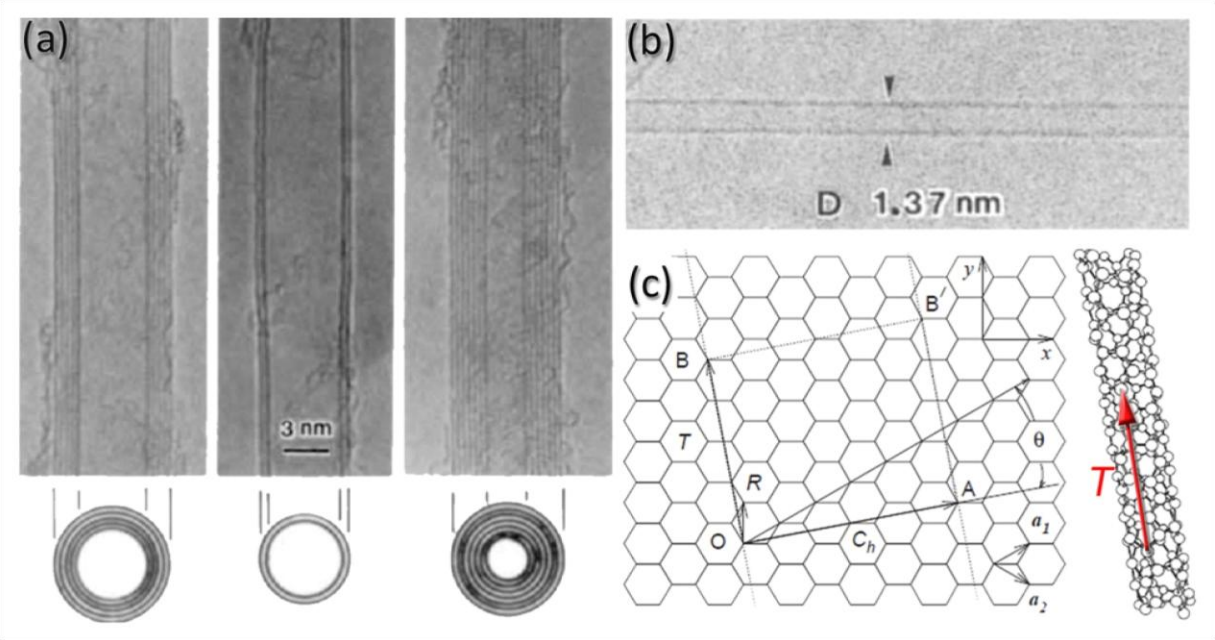

Figure 1.1 *First TEM images showing, (a) the layered graphitic walls and tubular nature of CNTs*[11] *and (b) a CNT composed of a single wall. (c) The unrolled graphitic lattice of a nanotube, the vectors OA and OB define the chiral vector* $\boldsymbol{C}_h$ *and the translational vector* ***T*** *of the nanotube respectively.*[15]

CNTs are commonly segregated into multi-walled CNTs, metallic single-walled CNTs and semiconducting single-walled CNTs. At this point, it is worthwhile to consider how this can be? As all three are one dimensional structures comprised solely of carbon atoms in graphitic ordering, how can nanostructures with identical composition and chemical bonding exhibit such a drastic range of electronic band structure? To answer this question, it is necessary to consider the possible orientation of a graphitic lattice and how that variation can affect the conductivity of a material.

If a CNT is unzipped along its axis, a graphene sheet is obtained as illustrated by Figure 1.1c. As one can imagine, the sheet can have various orientation based on the way it is rolled up. The different configurations commonly referred to as chirality or helicity, which can be expressed by the chiral vectors $\boldsymbol{C}_h$.

$$\boldsymbol{C}_h = n\boldsymbol{a}_1 + m\boldsymbol{a}_2 \qquad \text{- (1)}$$

This vector provides information regarding the chirality of the tube, from which the diameter could be calculated. Therefore, the indices (*n,m*) are a common way used to express the various graphitic configurations of CNTs. It is known that difference in chirality, along with the tube diameter, can influence the subsequent electronic energy structure. Yet why is it so?

At a glance, one would postulate that CNT should be a zero-bandgap semiconductor from the similarity between the structure of an unravelled CNT and that of pristine graphene. However, due to the strain induced by the curvature of the side-walls and the aforementioned chiral variability, the numbers of permissible *k*-vector states are limit and structurally dependant. As a result, difference in tube diameter and side wall chirality will vary the electronic band structures. Even though this is the case, the chiral and diameter dependent conductivity is not observed in multi-walled CNTs. This is due to the inter-wall interaction, which causes the energy level within the bands to become degenerate.[16] However, these inter-wall interactions are eliminated upon reducing the constituting side wall to a single graphitic shell (i.e. in the case of single-walled CNT). Therefore, single-walled CNTs can exhibits metallic or semiconducting properties according to the chirality and diameter of the tube. Based on the relationship between chirality and band gap, approximately 67% of chiral configurations are semiconducting and 33% are metallic at room temperature. The intrinsically tunable band gap of CNTs makes them an attractive and potentially versatile material.

1.1.1 Growth of Carbon Nanotubes

To grow CNTs, three things are needed: heat, carbon precursor, and catalyst particles. At the right conditions, the thermal energy allows the catalytic decomposition of the carbon sources. These carbon atoms are then diffused into the catalyst nanoparticles. As the carbon solubility of the nanoparticle reaches their supersaturation threshold, a graphitic layer precipitated onto the surface of the catalyst. The continuous incorporation of carbon material into the nanoparticle will subsequently lead to an extrusion of a tubular graphitic structure. Depending on the adhesion between the catalyst nanoparticle and the substrate, the process could be either base-growth or tip-

growth.[17] The growth of CNT stops once the diffusion of carbon into the catalyst nanoparticles ceases, this could happen either upon oversaturation of the nanoparticle or if the source of the hydrocarbons is terminated.[18] The growth of CNTs is an example of bottom-up nanofabrication, where the atoms self-assemble into a predetermined nanostructure under the right condition.

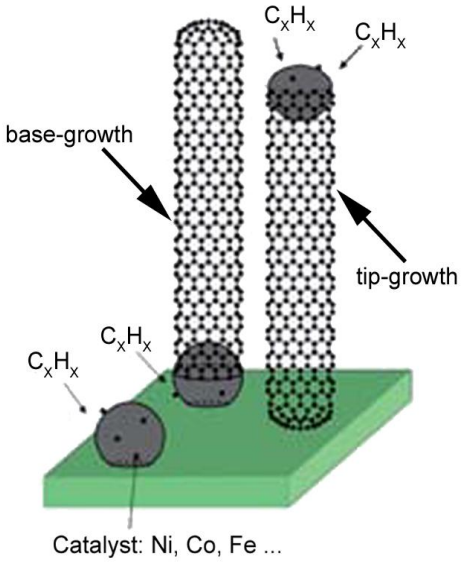

Figure 1.2 *Schematic of the growth process, where the hydrocarbons decomposed and defused into the nanoparticles, eventually leading to tube extrusion via either tip or base-growth. Figure is adapted from Nessim, Nanoscale 2, 1306 (2010).*[19]

In addition to exhibiting self-assembled growth, the growth of CNTs can also be tuned to spontaneously form a CNT-collective with vertical alignment. Such an array structure had found many uses in applications where a high density of CNTs is necessary. Yet, how does vertical alignment arise? It had been shown that the vertical alignment of CNTs is enabled by a high density of nucleating tubes. Figure 1.3a illustrates this effect. It was found that when the catalyst spacing is below a certain threshold, the simultaneous nucleation of many CNTs will lead to their growth in the vertical direction in order to minimise the disturbance from neighbouring CNTs. This is commonly referred to as the “crowding effect”. Therefore, the degree of alignment in the arrays could be controlled by tuning the catalyst spacing. Furthermore, there is a strong correlation between the diameter of the tubes and the required catalyst spacing for vertical alignment (Figure 1.3b).[20] As

vertical alignment from the crowding effect occurs simultaneously and can be controlled, it is desirable to preserve them in functional devices.

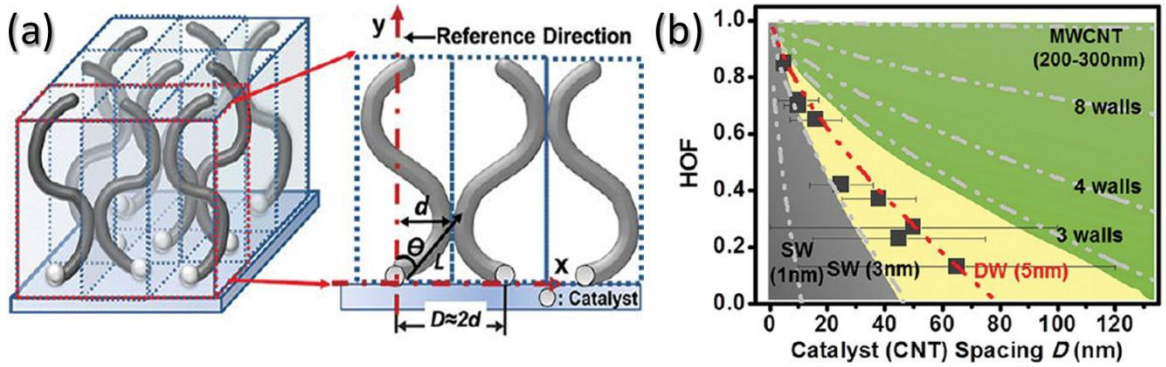

Figure 1.3 *Schematic of the crowding effect (a) and graph of alignment as a function of catalyst (CNT) spacing to qualitatively explain how crowding effect dominates the alignment control (b).*[20]

Apart from the variability in their electronic structures and their self assembled growth, CNT also exhibits many unique and often unparallel physical properties which elevate them from a mere scientific curiosity to a material of interest for a range of applications. In the next portion of this chapter, I will briefly discuss the origin of these attributes.

1.1.2 Physical Properties of Carbon Nanotubes

Electrical Properties

Other than having a tuneable band gap, CNTs are known to possess superb charge transport ability. This arises from their graphitic ordering which minimises the electron's interaction with the carbon lattice and prevents current induced displacement of atoms (i.e. electromigration). It had been experimentally confirmed that due to the low interaction between the electrons and the lattice, CNT can support long range ballistic transport at room.[21] This allows CNT to possess a larger mean free path (~1 μm at room temperature) than copper (~40 nm at room temperature).[22,23] Transport measurement of CNTs have further shown them to exhibit a carrier mobility of $1x10^5$ cm^2 V^{-1} s^{-1} which is an order of magnitude higher than what is observed in silicon.[24] Due to their good transport properties and their resistance to electromigration, CNTs have the capability to sustain

high current densities (> 10^{10} A/cm^2) for an extended period of time.[25] This is similar to the current carrying ability of gold and a few orders of magnitude higher than commercially used conductors such as copper.[26,27] The good electrical attributes of CNTs, coupled with their nanoscale dimension, are of specific interest to many industries.[28] As currently, the limitations of conventional materials inhibit the miniaturisation and impede the development of next generation technologies.

Thermal Properties

The graphitic ordering of CNTs also grants them extraordinary thermal properties; as exhibited by their high thermal conductivity. Experimental measurements of CNTs have commonly shown a thermal conductivity of 3000-3500 W m^{-1} K^{-1} at room temperature.[29,30] This exceeds that of even diamond (2300 W m^{-1} K^{-1}), which is the highest known naturally occurring bulk thermal conductor. Furthermore, theory predicts that CNTs can possess a thermal conductivity of 7000 W m^{-1} K^{-1} at room temperature.[31] The high thermal conductivity of CNTs comes from its crystallinity and enclosed sp^2 structure.[32] The lack of defects and edge sites minimises phonon scattering; this allows the phonon transport to be dominated by the ballistic regime rather than the diffusive regime. The high thermal conductivity of CNTs allows them to be utilised in numerous applications, these include thin film transparent heaters,[33] microelectronic heat sinks,[34] and thermo-based energy generation.[35,36]

Surface Area

The one-dimensional nature of CNTs allows them to possess a high specific surface area. Theoretically, single-walled CNTs is expected to possess a specific surface area of 1315 m^2 g^{-1}.[37] This value is derived by taking into account the exterior surface of the graphitic structure, while neglecting area of the interior void. Owing to the stacked arrangement of the graphitic side wall, the theoretical maximum specific surface area of multi-walled CNTs will be lower than that of single-walled CNTs.[37] The following expression is used to determine their relationship:

$$\text{specific surface area} = \frac{1315 \times d_e}{n d_e - 0.68\left[\sum_1^{n-1} i\right]} \quad \text{- (2)}$$

where d_e is the external diameter of the multi-walled CNT in nanometres and n is the number of walls. The large amount of available surface makes CNTs a potential candidate for storage applications.[38] The morphology of CNTs also allows a high percentage of their constituent atoms to be on the surface; in fact 100% of the atoms of single-walled CNTs are surface atoms. Unlike atoms which are in the bulk, surface atoms are more sensitive to environmental perturbation. This coupled with their large specific surface area makes CNTs an interesting material for sensing application.[39]

Mechanical Properties of Carbon Nanotubes

The sp^2 bonding of carbon within a graphitic structure is one of strongest chemical bond known. As such, CNTs are expected to have exceptional mechanical properties. Experimental measurements had already demonstrated that CNTs possess a high tensile strength. In the work conducted by Yu *et. al.*,[40] the tensile strength of a shell within an individual multi-walled CNT was shown to range from 11-63 GPa. The author realised that this value was below theoretical prediction due to the presences of defects and a mismatch between the tensile-loading direction and the tube's alignment. A more recent study utilising higher-quality multi-walled CNTs showed them to possess a tensile strength of 100 GPa, which is close to the theoretical prediction of CNTs with a small concentration of defects.[41] Theoretically, defect free single-walled CNTs should possess an even larger tensile strength of >300 GPa.[42] Due to the strength of the graphitic lattice, CNT also displays a high Young's modulus (expected to be around 1 TPa) along the tubular axis. However as this stiffness is anistropic, CNTs have been shown to be flexible. This allows CNTs to be resilient to large strains and repeated bending.[43] The mechanical properties of CNTs have led them to be utilised as an addictive in polymers-based composites to increase their mechanical properties.[44]

Till now, this chapter had briefly described what constitutes a CNT, their growth and outlined their known properties. Currently, numerous fields have reached a bottleneck in their advance due to the

lack of suitable materials. This occurs as the traditional materials such as metals, polymers and organic fibres have reached their materials limits upon miniaturisation. Therefore CNT is fascinating as their possessing performances surpass many conventional materials. As such, there are tremendous interests in applying CNTs for both fundamental and applied research.

Electron mobility at room temperature	$1x10^5$ cm^2 V^{-1} s^{-1}
Current Density	$1\text{-}10x10^9$ A cm^{-2}
Thermal conductivity	3000-3500 W m^{-1} K^{-1}
Surface Area	1315 m^{-2}
Tensile Strength	100 GPa
Young's Modulus	1 TPa

Table 1.1 Summary of the physical attributes of CNTs

1.1.3 Challenges confronted by Carbon Nanotubes

So far, the introduction for this thesis almost reads like a marketing pitch for CNTs, with words such as "unparallel", "extraordinary" and "surpass" being used unsparingly to describe their abilities. From reading so many superlatives, a cautious reader would ask the question, "What's the catch?" After all, if this material is vastly superior to conventional materials, why haven't CNTs completely replaced them?

Despite the many desirable features of CNTs, there are various challenges which hinder their adoption. In this thesis, I will focus on the following: inability to impose deterministic growth; difficulties in integrating CNTs into device applications; and the cytotoxicity of CNTs. These issues are significant as while they remain unsolved, the utilisation of CNTs will continue to remain restricted. Firstly, the inability to impose deterministic growth of CNTs impairs our ability to control the attributes of the resulting CNTs. As such, the performances of experimentally obtained CNTs remain below what are theoretically predicted. Secondly, though CNTs possess many attribute attractive to various devices application, challenges in their integration due to the shortcomings of current

process methods prevent the full potential of the CNTs to be utilised for the desire application. Lastly, though the large surface area, unique morphology, carbon-based composition and stability of CNTs have made them attractive to a range of biological applications; their perceived intrinsic cytotoxicity prevents their deployment.

1.2 Executive Summary of the Thesis

Having discussed the potential attractiveness of CNTs and various problems which had impeded their utilisation, my work aims to explore the concept and application of CNT-based hybrid nanomaterials as a way to augment the ability of CNTs while overcoming their shortcoming. The thesis will consist of seven chapters (including this), five of which will be dedicated to address specific issues. The concluding chapter will summarize the achievement of this work and provide a brief discussion of future work. The list of chapters and a brief description of their contents are as follow.

- **Chapter 2: Controlling the Growth of Single-Walled Carbon Nanotubes via Catalyst Nanostructure Engineering**

Chapter 2 will present my work in developing a strategy for controlling the growth of single-walled CNTs and influence their subsequent attributes. Though the main focus of this chapter will be on CNT rather than CNT-based hybrids, it will discuss in details the deterministic factors regarding the growth of CNTs and serve to introduce key concepts for subsequent chapters. This portion of the thesis is based on my article "**Controlled Growth of Single-Walled Carbon Nanotube Networks by Catalyst Interfacial Diffusion**" which was published in *Advanced Materials Interfaces*.[45]

- **Chapter 3: Coupling Metal Nanostructures and Carbon Nanotube Arrays for Hydrogen Sensing**

Chapter 3 will be the first in a series of chapters regarding the implementation of CNT-based hybrid in devices and the first of two chapters focused on sensing applications. The chapter will examine

the coupling of CNTs with metal nanostructures for gas sensing. Specifically, the chapter will discuss the formation and the sensing mechanism of a Pd-CNT core-shell structure for hydrogen detection. This work was based on the published articles, "**Physisorption-induced electron scattering on the surface of carbon-metal core-shell nanowire arrays for hydrogen sensing**" which was published in *Applied Physics Letters* and was done in collaboration with Dr Massoud Aghili Yajadda.[46]

- **Chapter 4: Plasma Scribing, a Mask-less Patterning of Carbon Nanotube Arrays for Plasmonic Sensing**

Chapter 4 will continue the exploration of CNT-based hybrids in chemical sensing. This chapter will focus on two elements, chemical modification of a three dimensional CNT arrays while preserving their microstructure and controlling the spatial distribution of decorating metal nanostructures within a CNT array. Rather than using a resistive mechanism, the chemical sensing will be achieved via plasmonic mechanisms. This chapter is based on my published articles **"Atmospheric microplasma-functionalized 3D microfluidic strips within dense carbon nanotube arrays confine Au nanodots for SERS sensing"** which was published in *Chemical Communications*.[47]

- **Chapter 5: Enhanced Supercapacitor Performance via the Fusion of Vertical Graphene Nanosheets and Carbon Nanotubes**

Chapter 5 will continue the discussion regarding the utilisation of CNTs in devices and present the collaborative work which I had conducted with Mr Dong Han Seo on the direct growth of CNTs on Vertical Graphene Nanosheets for the purpose of supercapacitor applications. This chapter will discuss the process of combining two carbon nanomaterials and factors which influences their device performance. The work presented here is based on my equal contribution manuscript titled "***Synergistic Fusion of Vertical Graphene Nanosheets and Carbon Nanotubes for High Performance Supercapacitor Electrodes***" which was published in *ChemSusChem*.[48]

- **Chapter 6: Bacterial Interactions of Carbon Nanotube Arrays**

Chapter 6 will examine the biological interaction of CNT arrays via bacteria models. This research was conducted collaboratively with Dr Anne Mai-Prochnow and was inspired by a previous research project about protein-CNT hybrids which I was part of.[49] This chapter examines the effects of CNTs with a vertically aligned microstructure has on *Escherichia Coli* and *Bacillus Subtilis*. The purpose of this work is to extend our understanding of the biological interaction possessed by CNT arrays.

- **Chapter 7: Conclusion and Future Outlook**

The final chapter of the thesis will summarise the work presented and discuss the relevance of CNT-based hybrid in overcoming the problem within the field of CNTs. I will also offer suggestions for future work and end this thesis with some concluding remarks.

In summary this thesis will explore the fabrication of CNT-based hybrid nanomaterials and their implications for sensing, energy storage and biological applications. The following chapters will present methods to controlling the growth of CNTs; the integration of CNT-based hybrid into sensor applications; the performance enhancement of energy storage devices via the utilisation hybrid nanomaterials; and the feasibility of CNTs as a platform to interact with biological species.

1.3 References

[1] Drexler E. K., **Engines of Creation 2.0**, 20th Anniversary Edition, *WOWIO LLC*, 2006.

[2] Ziemelis K., **Going Up**, *New Scientist*, 2001. (2289): 24-7.

[3] Feynman R. P. **There's plenty of room at the bottom**. *Journal of Microelectromechanical Systems* 1992; 1 (1): 60-6.

[4] Edelstein A. S., Cammaratra R. Nanomaterials: synthesis, properties and applications: CRC Press; 1998.

[5] Feng L., Li S., Li Y. *et al.* **Super-Hydrophobic Surfaces: From Natural to Artificial**. *Adv. Mater.* 2002; 14 (24): 1857-60.

[6] Fuechsle M., Miwa J. A., Mahapatra S. *et al.* **A single-atom transistor**. *Nat. Nanotechnol.* 2012; 7 (4): 242-6.

[7] **Ecclesiastes 4:9-10**, *The Holy Bible,* English Standard Version; 2001.

[8] Giraldo J. P., Landry M. P., Faltermeier S. M. *et al.* **Plant nanobionics approach to augment photosynthesis and biochemical sensing**. *Nat. Mater.* 2014;10.1038/nmat3890.

[9] Monthioux M., Kuznetsov V. L. **Who should be given the credit for the discovery of carbon nanotubes?** *Carbon*. 2006; 44 (9): 1621-3.

[10] Radushkevich L. V., Lukyanovich V. M. **O strukture ugleroda, obrazujucegosja pri termiceskom razlozenii okisi ugleroda na zeleznom kontakte (About the structure of carbon formed by thermal decomposition of carbon monoxide on iron substrate)**. *Zurn. Fisic. Chim.* 1952; 26: 88-95.

[11] Iijima S. **Helical Microtubules of Graphitic Carbon**. *Nature*. 1991; 354 (6348): 56-8.

[12] Iijima S., Ichihashi T. **Single-shell carbon nanotubes of 1-nm diameter**. *Nature*. 1993; 363 (6430): 603-5.

[13] Bethune D. S., Klang C. H., de Vries M. S. *et al.* **Cobalt-catalysed growth of carbon nanotubes with single-atomic-layer walls**. *Nature*. 1993; 363 (6430): 605-7.

[14] Zhang Q., Huang J.-Q., Qian W.-Z. *et al.* **The Road for Nanomaterials Industry: A Review of Carbon Nanotube Production, Post-Treatment, and Bulk Applications for Composites and Energy Storage**. *Small*. 2013; 9 (8): 1237-65.

[15] Dresselhaus M. S., Dresselhaus G., Saito R., Jorio A. **Raman spectroscopy of carbon nanotubes**. *Phys. Rep.* 2005; 409: 47.

[16] Green A. A., Hersam M. C. **Properties and Application of Double-Walled Carbon Nanotubes Sorted by Outer-Wall Electronic Type**. *ACS Nano*. 2011; 5 (2): 1459-67.

[17] Wang Y., Li B., Ho P. S. *et al.* **Effect of supporting layer on growth of carbon nanotubes by thermal chemical vapor deposition**. *Appl. Phys. Lett.* 2006; 89 (18): -.

[18] Ostrikov K. **Reactive plasmas as a versatile nanofabrication tool**. *Rev. Mod. Phys.* 2005; 77: 489-511.

[19] Nessim G. D. **Properties, synthesis, and growth mechanisms of carbon nanotubes with special focus on thermal chemical vapor deposition**. *Nanoscale*. 2010; 2 (8): 1306-23.

[20] M. Xu, D. N. Futaba, M. Yumura, K. Hata. **Alignment Control of Carbon Nanotube Forest from Random to Nearly Perfectly Aligned by Utilizing the Crowding Effect**. *ACS Nano*. 2012; 6 (7): 5837-44.

[21] Urbina A., Echeverría I., Pérez-Garrido A. *et al.* **Quantum Conductance Steps in Solutions of Multiwalled Carbon Nanotubes**. *Phys. Rev. Lett.* 2003; 90 (10): 106603.

[22] Steinhögl W., Schindler G., Steinlesberger G. *et al.* **Comprehensive study of the resistivity of copper wires with lateral dimensions of 100 nm and smaller**. *J. Appl. Phys.* 2005; 97 (2): -.

[23] Mann D., Javey A., Kong J. *et al.* **Ballistic Transport in Metallic Nanotubes with Reliable Pd Ohmic Contacts**. *Nano Lett.* 2003; 3 (11): 1541-4.

[24] Zhou X., Park J.-Y., Huang S. *et al.* **Band Structure, Phonon Scattering, and the Performance Limit of Single-Walled Carbon Nanotube Transistors**. *Phys. Rev. Lett.* 2005; 95 (14): 146805.

[25] Wei B. Q., Vajtai R., Ajayan P. M. **Reliability and current carrying capacity of carbon nanotubes**. *Appl. Phys. Lett.* 2001; 79 (8): 1172-4.

[26] Karim S., Maaz K., Ali G., Ensinger W. **Diameter dependent failure current density of gold nanowires**. *J. Phys. D: Appl. Phys.* 2009; 42 (18): 185403.

[27] Hong S., Myung S. **Nanotube Electronics: A flexible approach to mobility**. *Nat. Nanotechnol.* 2007; 2 (4): 207-8.

[28] Naeemi A., Meindl J. D. **Carbon nanotube interconnects**. *Annu. Rev. Mater. Res.* 2009; 39 (1): 255-75.

[29] Pop E., Mann D., Wang Q. *et al.* **Thermal Conductance of an Individual Single-Wall Carbon Nanotube above Room Temperature**. *Nano Lett.* 2005; 6 (1): 96-100.

[30] Kim P., Shi L., Majumdar A., McEuen P. L. **Thermal Transport Measurements of Individual Multiwalled Nanotubes**. *Phys. Rev. Lett.* 2001; 87 (21): 215502.

[31] Donadio D., Galli G. **Thermal Conductivity of Isolated and Interacting Carbon Nanotubes: Comparing Results from Molecular Dynamics and the Boltzmann Transport Equation**. *Phys. Rev. Lett.* 2007; 99 (25): 255502.

[32] Balandin A. A. **Thermal properties of graphene and nanostructured carbon materials**. *Nat. Mater.* 2011; 10 (8): 569-81.

[33] Janas D., Koziol K. K. **A review of production methods of carbon nanotube and graphene thin films for electrothermal applications**. *Nanoscale*. 2014;10.1039/C3NR05636H.

[34] Kordás K., Tóth G., Moilanen P. *et al.* **Chip cooling with integrated carbon nanotube microfin architectures**. *Appl. Phys. Lett.* 2007; 90 (12): 123105.

[35] Choi W., Hong S., Abrahamson J. T. *et al.* **Chemically driven carbon-nanotube-guided thermopower waves**. *Nat. Mater.* 2010; 9 (5): 423-9.

[36] Kim S. L., Choi K., Tazebay A., Yu C. **Flexible Power Fabrics Made of Carbon Nanotubes for Harvesting Thermoelectricity**. *ACS Nano*. 2014; 8 (3): 2377-86.

[37] Peigney A., Laurent C., Flahaut E. *et al.* **Specific surface area of carbon nanotubes and bundles of carbon nanotubes**. *Carbon*. 2001; 39 (4): 507-14.

[38] Züttel A., Sudan P., Mauron P. *et al.* **Hydrogen storage in carbon nanostructures**. *Int J. Hydr. Energy*. 2002; 27 (2): 203-12.

[39] Zhang T., Mubeen S., Myung N. V., Deshusses M. A. A. **Recent progress in carbon nanotube-based gas sensors**. *Nanotechnology*. 2008; 19 (33): 332001.

[40] Yu M.-F., Lourie O., Dyer M. J. *et al.* **Strength and Breaking Mechanism of Multiwalled Carbon Nanotubes Under Tensile Load**. *Science*. 2000; 287 (5453): 637-40.

[41] Peng B., Locascio M., Zapol P. *et al.* **Measurements of near-ultimate strength for multiwalled carbon nanotubes and irradiation-induced crosslinking improvements**. *Nat. Nanotechnol.* 2008; 3 (10): 626-31.

[42] Ogata S., Shibutani Y. **Ideal tensile strength and band gap of single-walled carbon nanotubes**. *Phys. Rev. B*. 2003; 68 (16): 165409.

[43] Falvo M. R., Clary G. J., Taylor R. M. *et al.* **Bending and buckling of carbon nanotubes under large strain**. *Nature*. 1997; 389 (6651): 582-4.

[44] Hamedi M. M., Hajian A., Fall A. B. *et al.* **Highly Conducting, Strong Nanocomposites Based on Nanocellulose-Assisted Aqueous Dispersions of Single-Wall Carbon Nanotubes**. *ACS Nano*. 2014; 8 (3): 2467-76.

[45] Yick S., Han Z. J., Ostrikov K. **Controlled Growth of Single-Walled Carbon Nanotube Networks by Catalyst Interfacial Diffusion**. *Adv. Mater. Inter.* 2014;10.1002/admi.201300151.

[46] Yick S., Yajadda M. M. A., Bendavid A. *et al.* **Physisorption-induced electron scattering on the surface of carbon-metal core-shell nanowire arrays for hydrogen sensing**. *Appl. Phys. Lett.* 2013; 102 (23): 233111.

[47] Yick S., Han Z. J., Ostrikov K. **Atmospheric microplasma-functionalized 3D microfluidic strips within dense carbon nanotube arrays confine Au nanodots for SERS sensing**. *Chem. Commun.* 2013; 49 (28): 2861-3.

[48] Seo D. H., Yick S., Han Z. J. *et al.* **Synergistic Fusion of Vertical Graphene Nanosheets and Carbon Nanotubes for High-Performance Supercapacitor Electrodes**. *ChemSusChem*. 2014;10.1002/cssc.201402045.

[49] Kondyurin A., Levchenko I., Han Z. J. *et al.* **Hybrid graphite film–carbon nanotube platform for enzyme immobilization and protection**. *Carbon*. 2013; 65 (0): 287-95.

Controlling the Growth of Single-Walled Carbon Nanotubes via Catalyst Nanostructure Engineering

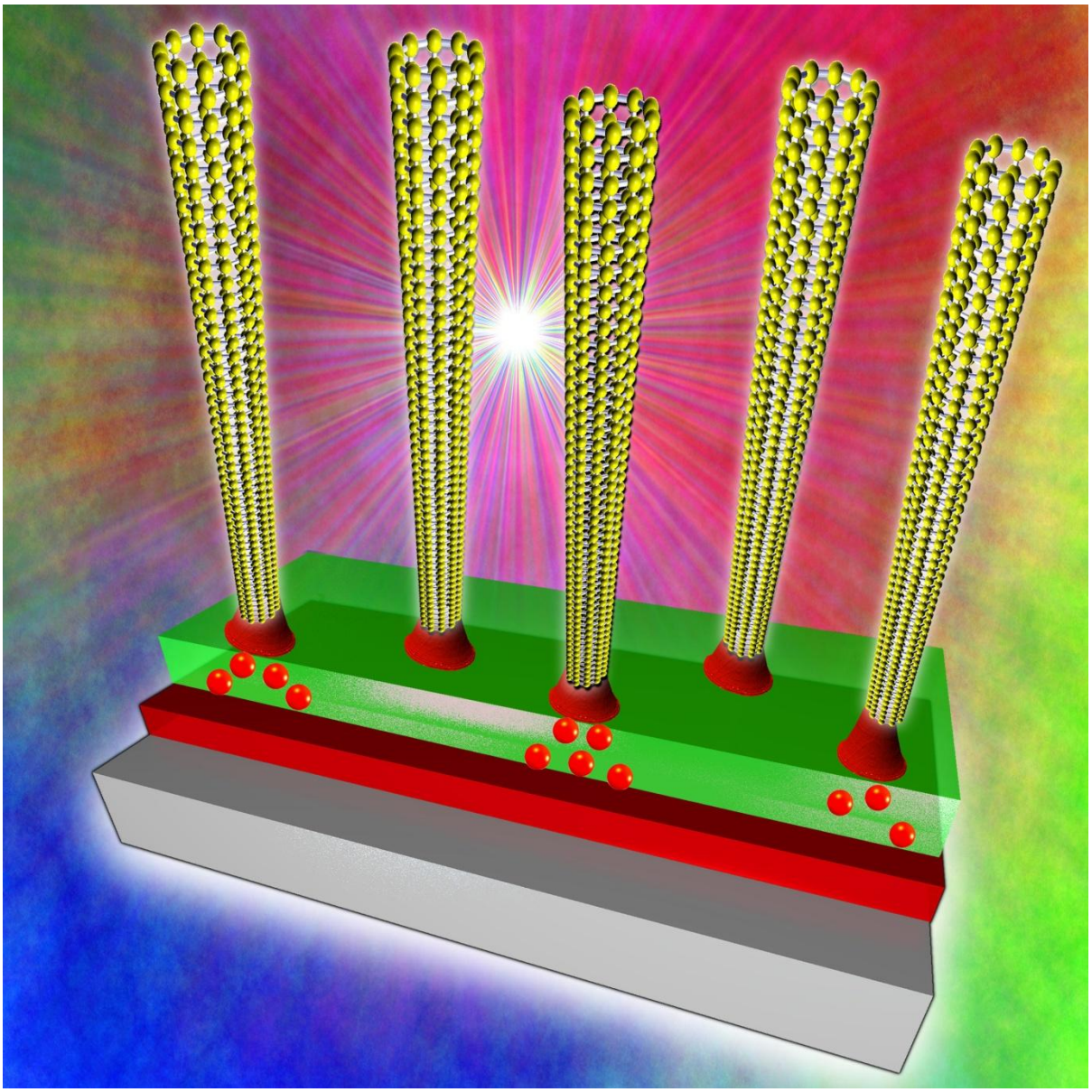

Frontispiece which accompanied the article “Controlled Growth of Single-Walled Carbon Nanotube Networks by Catalyst Interfacial Diffusion” by Yick *et. al*.[1]

Chapter Summary

This chapter discuss factors which influence the growth of CNTs and on strategies to control the growth of single-walled CNTs (SWCNTs). Though SWCNTs possess many unique properties that make them promising for many applications, their implementation has been hampered by the inability to impose deterministic growth. The lack of control over the size and chirality distributions of the as-grown SWCNTs results in a non-uniformity to their physical attributes. This chapter aims to demonstrate the relationship between the catalyst size and the resulting electronic structures of the as-grown tubes. By using a tri-layered Al_2O_3/Fe(Mo)/Al_2O_3 catalyst, the formation of the catalyst nanoparticles can be controlled by modulating the diffusion of the Fe atoms through the top buffer layer. Therefore, by varying the thickness of the top Al_2O_3 layer, effective control over the density, diameter, and conductivity of the as-grown nanotube networks can be achieved. The work presented here may thus represent a promising strategy for tailoring the properties of as-grown SWCNT networks for their proposed applications. This chapter is based on the paper "Controlled Growth of Single-Walled Carbon Nanotube Networks by Catalyst Interfacial Diffusion" by Yick *et. al*.[1]

2.1 Why is Control Difficult?

As presented in chapter 1, SWCNT is an one-dimensional nanostructure which exhibits properties depending on its diameter and chirality.[2-4] By controlling the chirality, the electronic structure of as-grown SWCNTs can be tailored to be either metallic or semiconducting.[5] This allows SWCNTs to be exploited in a wide range of applications according to their electrical conductivity; for example, metallic-SWNTs (m-SWCNTs) have been used for electrical interconnects and transparent conducting films, whereas sensors and transistors are typically fabricated from semiconducting-SWCNTs (s-SWCNTs).[6-9] However, the utilization of SWCNTs in many applications has been hampered by the limitations of their synthesis processes, which so far have been unable to produce high-purity single chirality SWCNTs.[10,11]

To understand why it is difficult to control the growth of SWCNTs, it is necessary to discuss the current understanding of how chirality of the SWCNTs is determined during growth. There are three main hypotheses regarding how chirality are determined during the growth of SWCNTs, these include chiral-selective nucleation, chiral-dependent growth rate, and chiral-dependent lifetime.[12] Until recently, the chiral-selective nucleation hypothesis was thought to explain the chiral selectivity of CNTs. In this hypothesis, the chirality of CNTs was thought to depend on the structure of the end-caps formed prior to the extrusion of the tube. Yet, it had been demonstrated that the arrangements of the hemispherical end-cap have very little intrinsic preference to the subsequent chiral arrangement of the tube.[13] This, therefore, discredited the chiral-selective nucleation hypothesis as a viable explanation for chiral selectivity during CNT growth. In the chiral-dependent lifetime hypothesis, it is proposed that inclinations for growth termination or chiral change are dependent to the chiral-structure of the tube. Therefore, certain growth conditions can promote the formation of SWCNTs with specific chiralities while prohibiting others.[14,15] Though this could be plausible, it currently lacks experimental validation. Therefore, chiral-dependent growth rate is the preferred mechanism of late for understanding chiral-selectivity in SWCNTs. This hypothesis proposed that carbon atoms attempting to be integrated into different chiral sites face different energy barriers. Therefore, the chirality of an as-grown tube reflects the most energetically favourable configuration during growth. This theory has found experimental support when the growth rates of individual SWCNTs with different chirality were measured.[16,17] Regardless of the exact mechanism, all these hypotheses indicate that the catalyst nanoparticles play a deterministic role in influencing the as-grown chirality.

So what does the catalyst do? Aforementioned, the catalyst particles serve the critical function in nucleating the cap of the CNT and facilitating the addition of carbon atoms during the tube extrusion phase. Apart from serving as a physical template (i.e. size of the cap and tube diameter), it also determines the chiral angle through its interaction with the graphitic edge. This interaction depends strongly on the diameter of the nanoparticle and the chemical potential, a factor dictated by the

materials composition.[18] It is for this reason that different catalysts system had exhibited different chirality preference. For example, a cobalt/molybdenum catalyst system can exhibit a strong preference for growing semiconducting SWCNTs,[19] where as γ-phase iron nanoparticles are more prone to growing metallic SWCNTs.[20] However, despite being able to control the composition of the catalyst nanoparticles, it was found that controlling the size of the nanoparticles remains non-trivial. This is because the thermal energy necessary for the growth process will also result in diffusion and sublimation of the catalyst material; this will inevitably cause a variability to the size of the nanoparticles.[21] As the size of the catalyst becomes heterogeneous, the as-grown tubes will also possess a diverse morphology. This results in an inconsistency in their physical properties and thus, hindering their utilisation. Currently, one of the most detrimental factors which prevent the utilisation of SWCNTs in many applications is the mutual presence of both m-SWCNTs and s-SWCNTs.[10,11] In order for the capability of SWCNTs to be fully exploited, large quantity of SWCNT with minimal deviation in electrical properties is required. Therefore, the ability to control the relative fraction of a specific type of SWCNTs is of particular interest.

To this end, various strategies to enrich specific types of SWCNTs are available. These strategies fall on two approaches, post-growth enrichment or direct-growth modulation. The existing post-growth separation techniques exploit the subtle physical differences (i.e. conductivity, size, chemical stability) between m-SWCNTs and s-SWCNTs. Examples of these techniques include electrical breakdown, dielectrophoresis, gel chromatography, ultra-centrifugation, and selective etching.[22-25] However, these processes can also introduce external contaminants and structural defects which inevitably compromise the properties of the materials.[26-29] For this reason, the performance of device based on post growth enriched SWCNTs still lag behind the theoretical expectations.[30,31]

Direct growth modulation provides an alternate strategy in narrowing the variation within SWCNTs. From the growth mechanism presented before, the structure of SWCNTs is determined by the catalyst particles and growth conditions.[12] Controlling these factors offers a possibility to reduce the

distribution of diameters and chiralities of the as-grown SWCNTs.[32-35] There are numerous techniques which have been shown to grow SWCNTs, these include laser ablation, arc discharge, and chemical vapour deposition (CVD).[36] The last process could be further divided into purely thermal based process (TCVD) and plasma enhanced process (PECVD). These processes provide different means of controlling the decomposition of the hydrocarbons and the condition experienced during growth. Of the techniques listed above, TCVD is particularly attractive as it is a scalable thermal process, offering tunability to various growth parameters as well as the ability to assemble the as-grown SWCNTs into functional three-dimensional vertical arrays, two-dimensional interconnected networks, or individually nanotube devices. Nevertheless, the preferential growth of SWCNTs in a CVD process remains challenging. Firstly, due to the inter-dependence of various parameters, varying a single condition may influence other aspects of the growth.[37] This subsequently complicates one's ability to exert precise control over the entire growth process. Secondly, in order to nucleate a large number of SWCNTs, a high density of small catalyst nanoparticles with a narrow size distribution is needed. However, this is very difficult to achieve at the high temperatures required for SWCNT nucleation and growth. At such temperature, the coagulations of nanoparticles arising from surface diffusion and Ostwald ripening broadens the size distribution and hence lower the density of active catalyst nanoparticles.[38,39] It is thus highly desirable to develop a method which can effectively reduce the size distribution while preserving the population of catalytically active nanoparticles.

Here I will demonstrate control over the as-grown SWCNTs through catalyst interfacial diffusion. This was achieved through engineering a tri-layered catalyst system which consists of an Al_2O_3 layer on top of the Fe/Mo catalyst supported by another Al_2O_3 underlayer. The tri-layered catalyst has been previously utilized to control the bandgap s-SWNCTs.[40] It is based on the principle that, upon annealing, the Al_2O_3 top layer allows interfacial diffusion of the catalyst atoms to form small-size nanoparticles which can subsequently nucleate and grow SWCNTs. Compared to previous works, I showed that by solely varying the thickness of the Al_2O_3 top layer, the size and density of Fe/Mo

catalyst nanoparticles can be controlled. Hence, the density, diameter and conductivity of the as-grown SWCNT networks were also modulated. This approach may thus be promising for the controlled synthesis of SWCNTs for a variety of advanced electronic and optical devices.

2.2 Methodology

Catalyst Layer Deposition. 10 nm of Al_2O_3 underlayer was first prepared by the reactive sputtering of an Al target with oxygen onto a Si/SiO_2 substrate (AJA Sputtering System). This was followed by the deposition of 1 nm Mo and 0.5 nm Fe by magnetron sputtering. The thickness of Mo layer was chosen through a series of optimization experiments for the maxmium network density. On top of these layers, an additional Al_2O_3 layer with the thickness varying from 0 to 50 nm was finally deposited using the same reactive sputtering procedure.

Growth of SWCNT Networks. To generate the catalyst nanoparticles, a thermal furnace (MTI, model OTF-1200X) with a 50 mm quartz tube was heated to 900 °C in air prior to sample insertion. Then, continuous co-flows of Ar and H_2 were introduced at 100 square cubic centimetre (sccm) into the quartz tube and the tri-layered catalyst structures were annealed for 5 minutes at atmospheric pressure (*i.e.*, the "fast-heating" pretreatment stage).[41] To grow SWCNTs, 400 sccm of CH_4 was introduced for 10 minutes, *i.e.*, the growth stage. After that, the CH_4 gas was terminated and the samples were cooled down to room temperature under the continuous flow of Ar and H_2.

Annealing of Catalyst Layer. To generate the catalyst nanoparticles for surface analysis, samples were exposed to the as-described growth conditions with no carbon precursors added, *i.e.*, only Ar and H_2 were introduced at 100 sccm and the catalyst structures were annealed for 5 minutes under atmospheric pressure. The furnace was then fast-cooled (within 10 minutes) to room temperature under a continuous co-flow of Ar and H_2 so as to prevent further evolution of the surface topography.

Characterisation Methods. The as-grown SWCNTs were characterized using field-emission scanning electron microscopy (FE-SEM; Zeiss Auriga) operated at electron beam energy of 1 keV with an InLens secondary electron detector. Transmission electron microscopy (TEM; JOEL 2100) was operated at electron beam energy of 200 keV. Samples for TEM characterization were prepared by ultrasonicating the SWCNTs in ethanol, the SWCNT suspension was dropped onto the holey carbon-coated copper grids and dried naturally in air. Micro-Raman spectroscopy was conducted using a Renishaw *inVia* spectrometer with laser excitations of 514 and 633 nm at a spot size of ~1 μm^2. Raman spectra from multiple spots were collected to obtain the average statistic analysis of the samples. The atomic force microscopy (AFM; Asylum Research MFP-3D) was operated in a tapping mode with an Al-coated monolithic silicon probe (Budget Sensors) which has a force constant of ∼5 N/m and a resonant frequency at ∼130 kHz.

Raman Analysis. The spectral analysis is illustrated in Figure 2.1. The Raman spectra were compiled from data collected at numerous points of the sample. In a sample with an area of 1 cm^2, Raman responses generated from a laser excitation wavelength of 633 nm were collected at 200 μm intervals. Only spectra with an observable peak at wavenumber of 1590 cm^{-1} (G-peak) were incorporated into the data set. These spectra were firstly normalised to the intensity of Si peak at 303 cm^{-1}, followed by subtraction of the Si spectra. The spectra were then averaged and incorporated into a single spectrum.

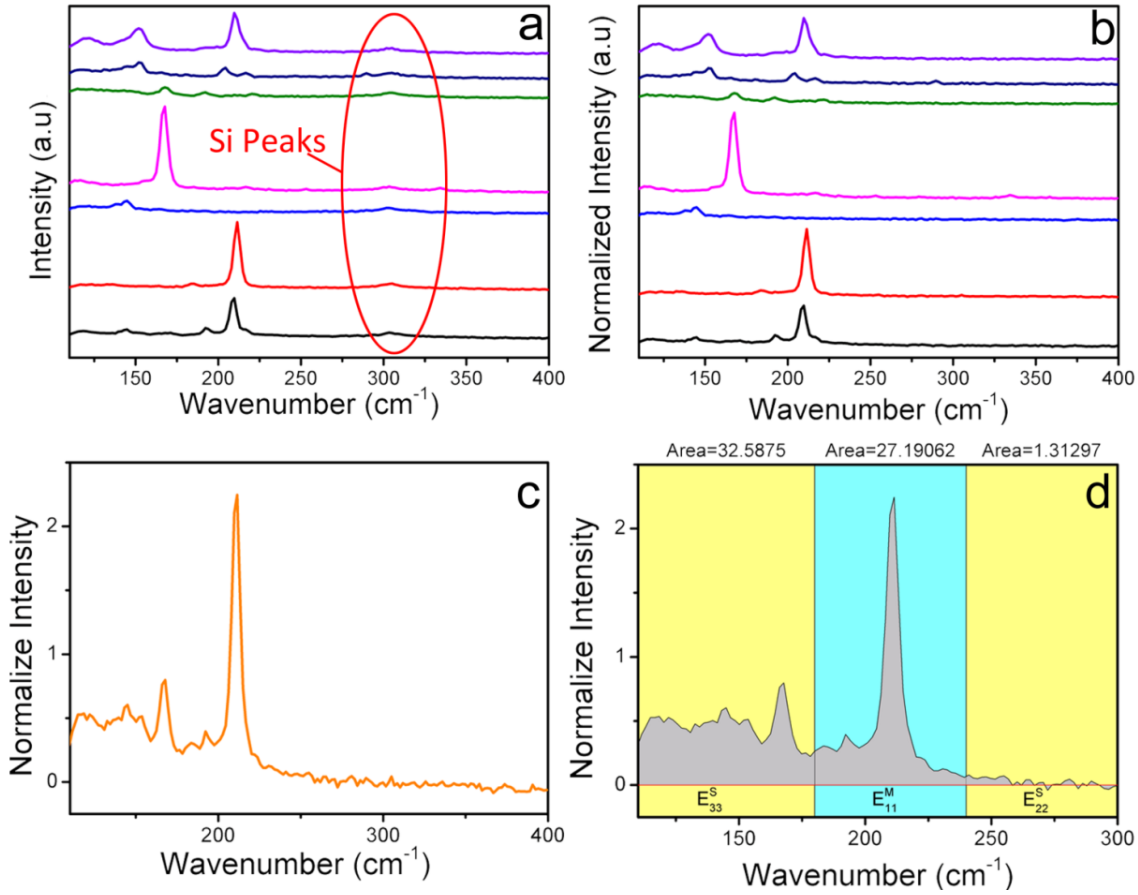

Figure 2.1 *The Raman analysis carried out. (a) Raman spectra collected from multiple spots on the sample. (b) Raman spectra after normalization to the Si peak at 303 cm^{-1}, followed by the subtraction of Si background. (c) The averaged Raman spectrum as plotted in a single spectrum. (d) The regions of E_{33}^{S}, E_{11}^{M} and E_{22}^{S} transitions and the determination of metallic fractions in the sample by integration (shaded areas).*[1]

In order to determine the metallic fraction of the nanotube in the sample, the averaged Raman spectrum was divided into three regions. The regions at 110 – 160 cm^{-1} and 240 – 300 cm^{-1} corresponded to the energy transition of E_{33}^{S} and E_{22}^{S} of the semiconducting SWCNT, respectively; whereas the regions between 160 to 240 cm^{-1} corresponded to the E_{11}^{M} transition of the metallic nanotubes.[42] By integrating the respective areas, the fractional percentage of the metallic nanotubes could be calculated as follows[43]

$$metallic\ fraction\ (\%) = \frac{E_{11}^{M}}{E_{33}^{S} + E_{11}^{M} + E_{22}^{S}} \times 100\%$$

2.3 Results and Discussion

2.3.1 Effects of diffusion on the density of SWCNT networks

The schematic diagram in Figure 2.2 depicts the tri-layered catalyst structure and the growth procedure. The catalyst consists of three components, namely, Al_2O_3 top buffer layer, Fe/Mo catalyst layer, and Al_2O_3 underlying buffer layer. The provision of thermal energy during the pretreatment and growth stages enables the interfacial diffusion of Fe through the Al_2O_3 top layer.[40] Transport of Fe atoms across Al_2O_3 can be described by the following expression,[44,45]

$$D = D_0 \exp(-E_A / k_B T) \qquad (2.1)$$

where D is the diffusivity (cm^2/s) of Fe through the Al_2O_3 layer at the temperature T, D_0 is the maximum diffusion coefficient (cm^2/s), E_A is the material's activation energy for diffusion (J/mol), and k_B is the Boltzman's constant. Furthermore, the diffusion length L of Fe atoms in the top layer can be expressed as a function of the diffusivity D and time t,

$$L = 4\sqrt{Dt} \qquad (2.2)$$

It was noted that in the report of *Song et al.*, the thickness of top Al_2O_3 buffer layer was fixed at 10 nm and the thermal annealing duration was varied in order to obtain differently sized catalyst nanoparticles.[40] Here, instead of varying the thermal annealing time, the thickness of the top buffer layer was varied from 0 – 50 nm while the thermal annealing time was kept constant in all growth processes. This should minimise the effect of thermal evaporation on nanoparticles and the size of catalyst nanoparticles could be primarily determined by the proposed diffusion process.[40]

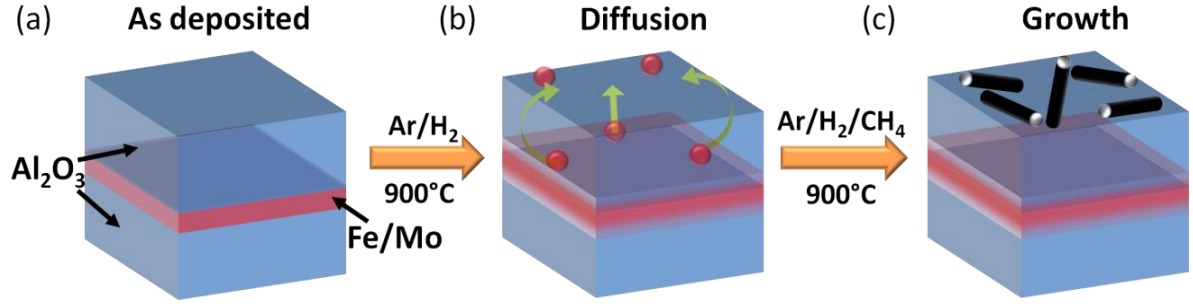

Figure 2.2 *Illustration of the experimental procedure, (a) the structure of the tri-layered catalyst system, (b) The catalyst system is annealed at high temperatures, which promotes diffusion of the catalyst material to the surface, (c) the nucleated catalyst nanoparticles are then able to induce the SWCNT growth.*[1]

Furthermore, Mo was used in conjunction with Fe in our catalyst system as it had been suggested that Mo allows better growth efficiency of SWCNTs by stabilizing the catalyst nanoparticles formed at high temperatures.[46] As Mo served merely as a stabilizer but not catalyst for SWCNT growth, the results shown in Figure 2.3 indicated that some Mo may also diffuse onto the surface (*e.g.*, through the grain boundaries within the interlayer) and affected the Fe-catalysed growth of SWCNTs.

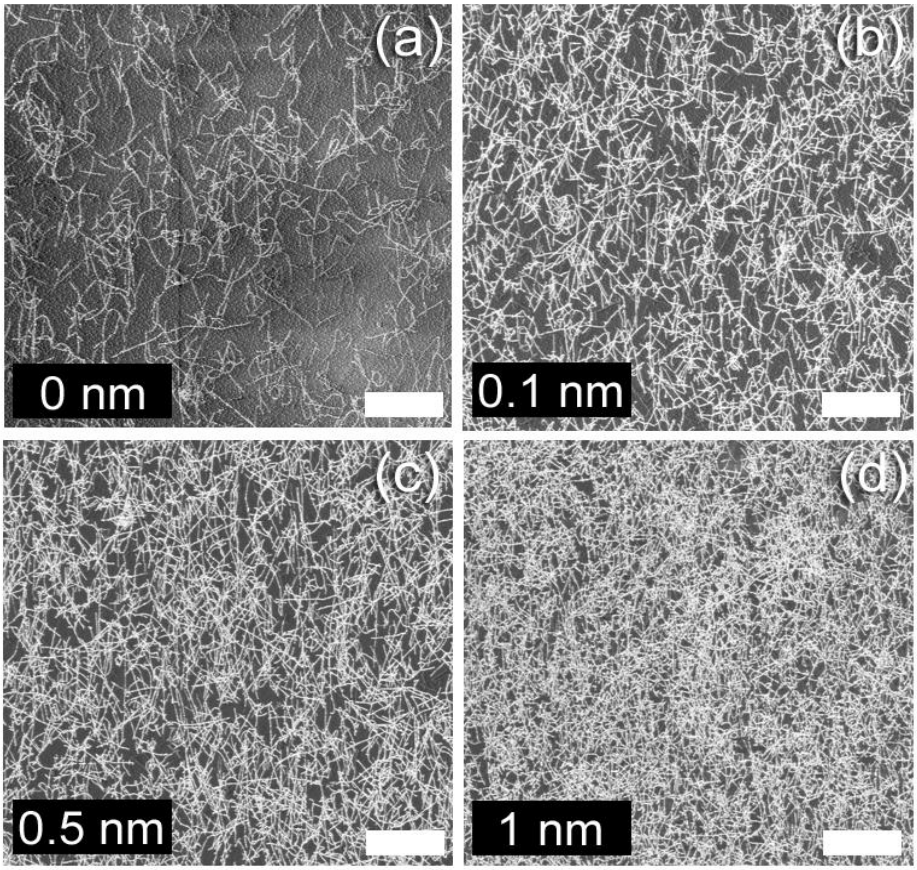

Figure 2.3 *The SEM images of the as-grown SWCNTs networks with varying Mo content. The thickness of the Mo layer were 0, 0.1, 0.5, 1 nm. Scale bars are 1 μm in all images.*[1]

The interfacial diffusion typically occurs *via* interstitial hopping (*i.e.,* bulk diffusion). However, the presence of grain boundaries and dislocations can increase the permeability of the buffer layer and facilitate the mass transport of Fe.[38] The diffusivity of Fe through the grain boundaries of Al_2O_3 was determined to be 5×10^{-16} cm^2/s, much higher than the diffusivity of interstitial hopping.[47] Thus, during the 15 minute-long thermal process at 900 °C (*i.e.,* the pretreatment and growth stages), the diffusion length of Fe atoms was estimated to be 26.8 nm according to Eq. (2.2). Consequently, by tuning the thickness of the Al_2O_3 top layer relative to this diffusion length, the density and size of catalyst nanoparticles can be controlled.

Figure 2.4 shows the SEM images of the as-grown SWCNTs from different tri-layered catalyst structures. One can see that when the Al_2O_3 top layer was absent (Figure 2.4a), the SWCNT network appeared sparse. As the thickness of the Al_2O_3 top layer increased to 5 nm, the density of the SWCNT networks increased drastically (Figure 2.4b). With both 10 and 20 nm Al_2O_3 top layers, the as-grown SWCNTs became "free-standing" (Figures 2.4c and d), in contrast to the "sub-monolayer to monolayer" coverage observed on thinner Al_2O_3 top layers (*i.e.*, a "surface-bound" state). This change in morphology correlated well with the "crowding effect" due to an increased nanotube density, where the substrate was unable to accommodate further nanotubes on the surface.[48,49] When the thickness of the Al_2O_3 top layer increased beyond 20 nm, the densities of nanotubes were found to decrease (Figures 2.4e and f). Nevertheless, it was still higher as compared to the networks grown without an Al_2O_3 top layer (Figure 2.4a).

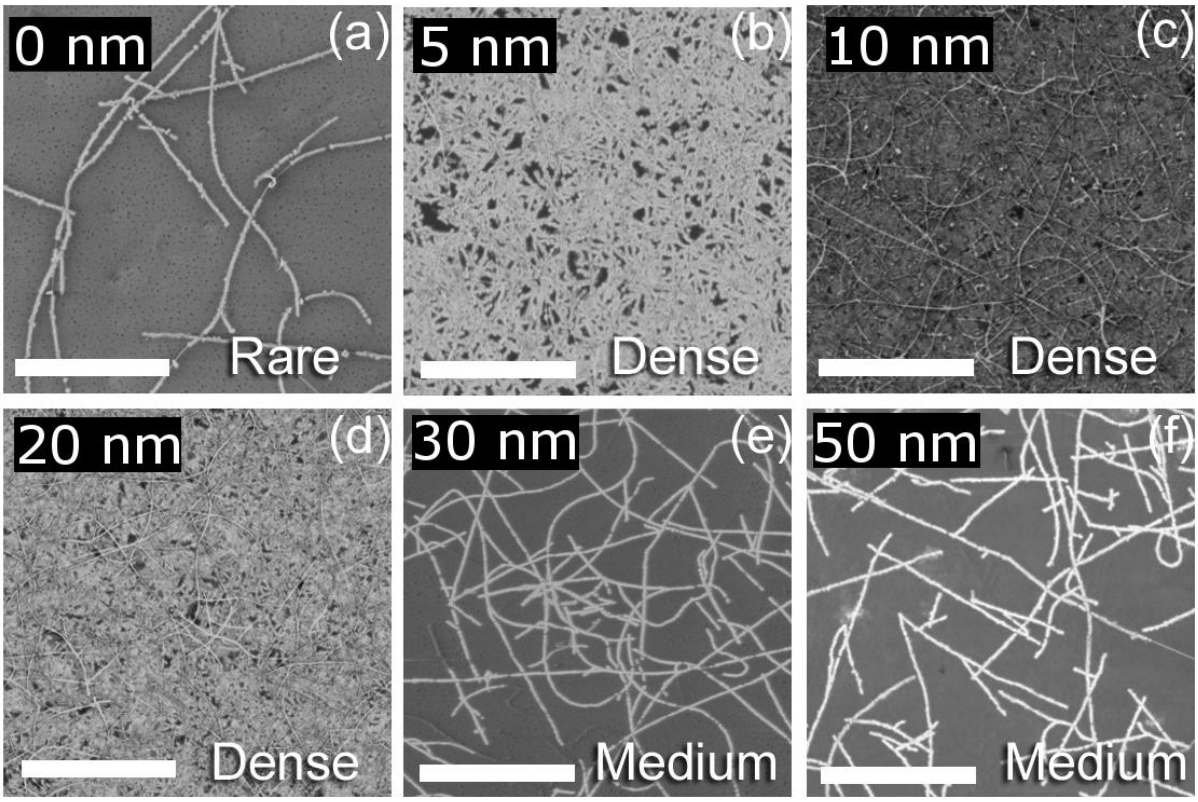

Figure 2.4 *(a-f) SEM images of the as-grown SWCNTs with the varied thickness in the Al_2O_3 top layer (labelled on each panel). The scale bars correspond to 2 µm in all images. The SWCNT networks are designated as rare, medium or dense according to their density.*[1]

The densities of SWCNTs produced from different catalyst structures were quantified by counting the number of nanotubes visible in the respective SEM micrographs. Figure 2.5 plots the density of SWCNT networks as a function of the thickness of Al_2O_3. As expected, the SWCNT network density reached a maximum of 35 tubes/μm^2 when the thickness of the top layer was 10 nm. A further increase of the thickness of top buffer layer resulted in a 20-fold reduction to the network density. Such observed trend in network density can be explained by considering how the Al_2O_3 top layer affected the Fe interfacial diffusion; in the absence of a top layer, Ostwald ripening of Fe catalyst nanoparticles was favoured during the entire pretreatment and growth stages.[38]

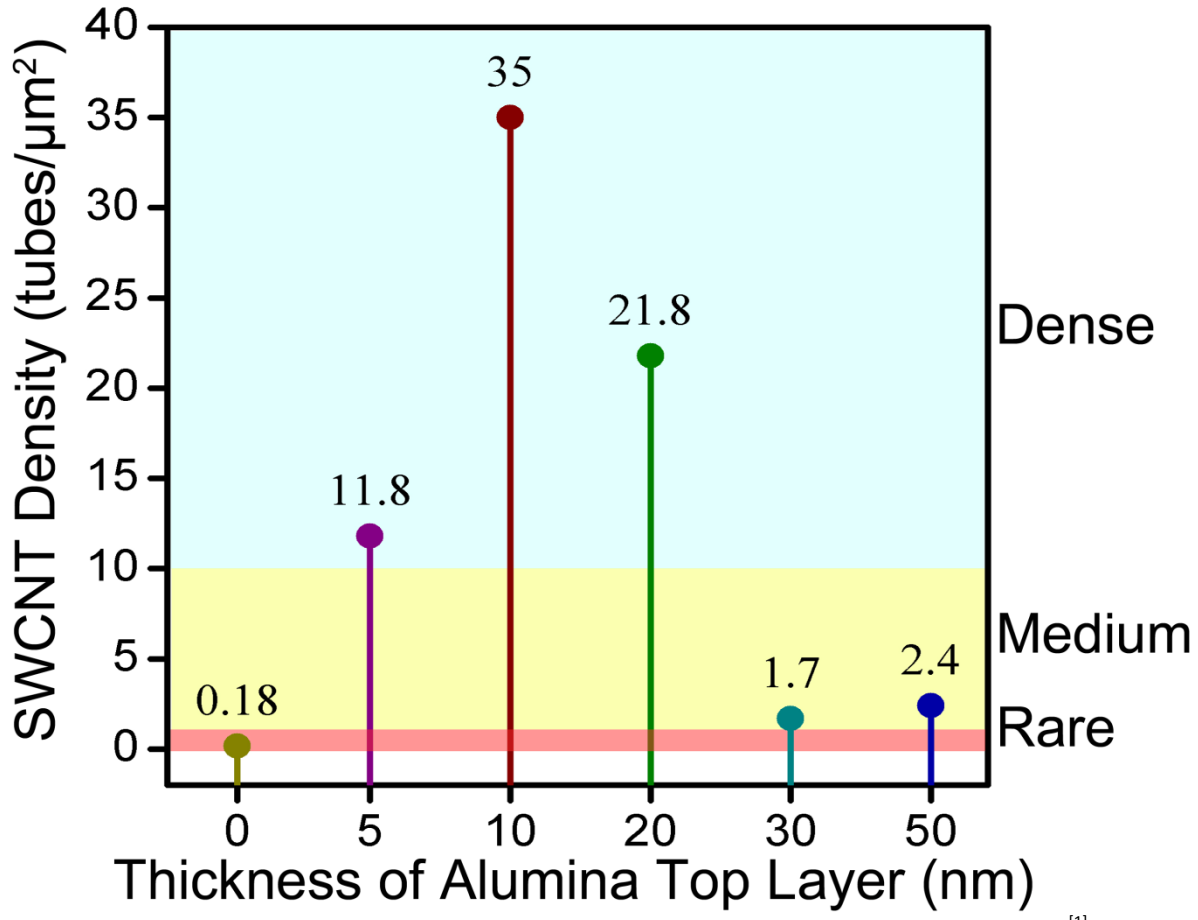

Figure 2.5 *The density of SWCNT networks plotted as a function of the thickness of Al_2O_3 top layer.*[1]

This enlarged the diameter of catalyst nanoparticles while simultaneously decreasing their surface density. Since the growth of SWCNTs is best supported by small- or medium-sized catalyst nanoparticles (<5 nm), the process of Ostwald ripening reduced the number of catalytically active nanoparticles suitable for SWCNT nucleation.[48,50] As such, the catalyst was less effective in the absence of an Al_2O_3 top layer; and subsequently sparse SWCNT networks were obtained as shown in Figure 2.4a.

On the other hand, for Al_2O_3 top layer with a thickness ranging from 5 to 20 nm, it would take Fe atoms approximately 0.5 – 10 minutes to diffuse through the top layer at 900 °C.[47] This implies that most of the catalyst material could be transported to the surface for nucleation and growth of SWCNTs. It has also been shown that interfacial diffusion of Fe through the Al_2O_3 could suppress Ostwald ripening and results in the formation of *γ*-phase Fe nanoparticles.[44,45] This meant that a

larger population of smaller catalyst nanoparticles could be maintained and the precipitation of Fe nanoparticles in the *γ*-phase also increased carbon solubility of the catalyst particle.

Indeed, our surface analysis of catalyst nanoparticles using atomic force microscopy (AFM) illustrated that the size and density of catalyst nanoparticles were greatly affected by the Al_2O_3 top layer (Figure 2.6). The annealed samples were fast cooled to prevent further evolution of the surface topography and thus the AFM images reflect the surface morphology prior to the growth of nanotubes. Figure 2.6a depicts the Al_2O_3 buffer layer in the absences of the catalyst layer. After being annealed at 900°C, the sample displayed an averaged surface roughness (R_a) of 0.173 nm. This indicates that the annealing process did not cause the Al_2O_3 buffer layer to fragment. By exposing the different catalyst systems to the same growth conditions with no carbon precursor (*i.e.*, no nanotube growth), it was found that in the absence of an Al_2O_3 top layer, large catalyst islands were formed with an average diameter of 30 – 50 nm, in consistent with the Ostwald ripening effect. In contrast, a much higher density of smaller nanoparticles were observed with the alumina top layer (Figure 2.6c). These observations were advantageous, as the resulting nanoparticles could have the suitable size, density and phase for nucleating SWCNTs.[51] This thus allowed the catalyst structures to support the observed high yield of SWCNTs (Figures 2.4b – d).

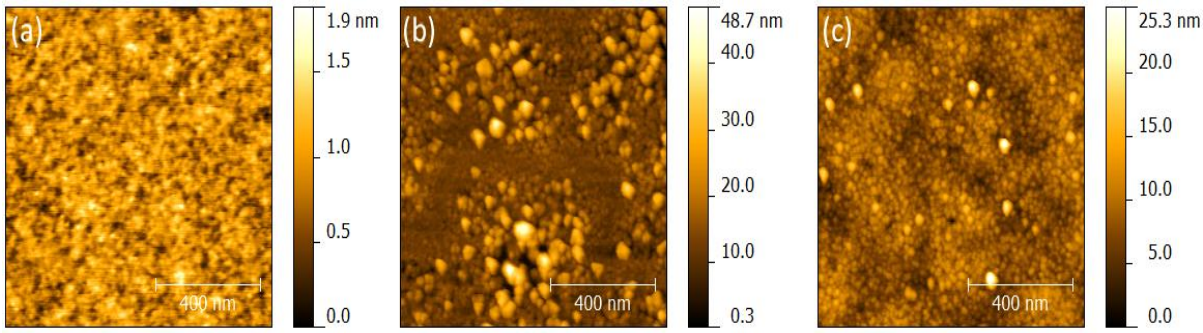

Figure 2.6 *AFM images of the different catalyst structures after being exposed to the same growth condition in the absence of a carbon precursor source: (a) the Al_2O_3 buffer layer in the absence of Fe catalyst, (b) the catalyst structure without an alumina top layer, and (c) the tri-layered catalyst structure with a 10 nm thick Al_2O_3 top layer. Note that the colour scale bars represent the topography of these images.*[1]

Upon further thickening of the Al_2O_3 top layer (>20 nm), the time required for Fe interfacial diffusion exceeded the growth process. Apart from decreasing the amount of available catalyst particles

emerged on the surface, this also shortened the overall duration for nucleating and growing SWCNTs. It is also possible that catalyst nanoparticles formed from less Fe diffusion were too small to nucleate SWCNTs due to the over-saturation of carbon atoms, and/or the nucleation conditions for such small particles were not met at the given surface temperature and supply of carbon precursor.[50,52] The yield of SWCNT networks thus dropped abruptly. These results indicated that the density of as-grown SWCNT networks can indeed be controlled by simply tuning the thickness of Al_2O_3 top layer. Such ability to control the tube density is of vital importance as different applications often requires different tube densities for optimal performance.[9,42,53]

2.3.2 Effect of diffusion on the graphitic crystallinity of SWCNT networks

Besides the yield of nanotubes, the presence of Al_2O_3 top layer also influenced the structures of the as-grown SWCNTs. This was investigated by performing micro-Raman measurements on these samples with different laser excitations and constructed the spectra using a method involving two normalization steps, similar to the one reported recently.[54] Briefly, the entirety of the 1×1 cm^2 samples were examined by collecting spectra at 200 μm intervals. Only the spectra with an observable peak at wavenumber of ~1590 cm^{-1} (*i.e.*, the G-peak) were considered for further analysis. These spectra were then normalised to the reference Si peak at 303 cm^{-1}, as it was the signal originated from the substrate and was constant at different locations. The choice of reference peak was different from that of *Orbaek et al*., as vertically-aligned SWCNT forests usually have too weak Si signals.[50] This was followed by subtracting the Si background obtained from a clean Si wafer with thermally grown SiO_2 layer. The spectra were then compiled and incorporated into a single spectrum using the inbuilt functions within Origin 8.

The same procedure was conducted for all samples grown with different Al_2O_3 top layer thicknesses. These compiled spectra were again normalized to the highest Raman G-peak. I emphasize here that the first normalization removed the experimental deviations from laser excitation or signal detection, while the second normalization enabled the direct comparison across different data sets.

The processed spectra thus represented the global characteristics of the as-grown SWCNT networks produced from the specific catalyst structures. These steps allowed the structure, diameter, and metallic fraction of the as-grown SWCNT networks to be analysed.

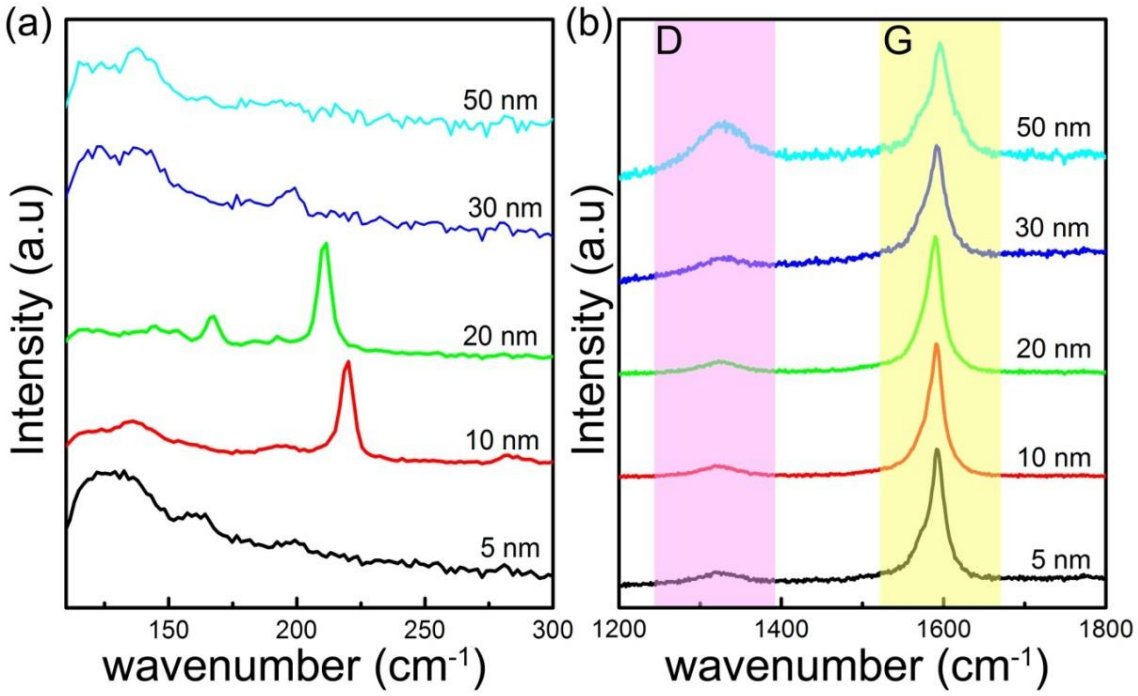

Figure 2.7 *(a) Raman spectra showing the RBM band. (b) D and G features corresponding to the as-grown SWCNT networks produced with different catalyst structures. The spectra are normalized to the respective G-peak and the Si background contribution is subtracted.*[1]

Figures 2.7a and b display the main peak features observed in the regions of 110 – 350 cm^{-1} and 1300 – 1700 cm^{-1} from these spectra obtained at 633 nm laser excitation. The former is attributed to the radial-breathing-modes (RBM) whereas the latter includes the disorder-induced feature (D-peak) at 1320 cm^{-1} and the ordered graphitic feature (G-peak) at 1590 cm^{-1}.[55] The spectrum corresponding to the sample without an Al_2O_3 top layer was omitted because the sparsity of SWCNT network prevented a meaningful Raman response. Additionally, though the laser excitation at 514 nm was performed, RBM modes were rarely observed. As indicated by the Kataura plot, the absence of RBM peaks from the 514 nm laser excitation could imply that this excitation was non-resonant with the as-grown SWCNTs or the densities of SWCNT which are in resonant were too low to generate meaningful signals.[56] Thus, in the present case only the RBM spectra from the 633 nm laser excitation were analysed.

It was found that variation to the Al_2O_3 top layer influenced the crystalline order of the as-grown structures, as evidenced by the change in the ratio of D- and G-peaks (*i.e.,* I_D/I_G). When the Al_2O_3 top layer was 5 nm, the I_D/I_G value was 0.125. This value decreased to 0.0625 upon the Al_2O_3 thickness at 10 nm, indicating that the crystallinity of SWCNTs grown on such Al_2O_3 top layers was improved. However, when the thickness of the Al_2O_3 top layer exceeded 20 nm, the I_D/I_G value increased to 0.5, implying a higher concentration of defects or the emergence of multi-walled nanotubes in the as-grown structures from these catalysts.

The variations in the I_D/I_G value could again be explained by the interfacial diffusion model and the commonly accepted growth mechanism of SWCNTs, which is based on the proposition that carbon saturation of catalyst nanoparticles precedes the extrusion and growth of the nanotubes.[57,58] At a relatively thin Al_2O_3 top layer, diffusion-based formation of catalyst nanoparticles could be within the appropriate size range for the nanotube nucleation.[59] This facilitated the growth of nanotubes with a high quality of graphitic structure. However, as the thickness of Al_2O_3 top layer increased, it created a higher barrier for catalyst diffusion, which may lead to incomplete mass transport of the catalytic materials (see Eq. (2.2)). Consequently, some nanoparticles remained at a very small size (instead of the optimum size for nucleation) which were more likely to be de-activated due to carbon oversaturation.[59] The presence of these oversaturated nanoparticles thus contributed to the higher intensity of D-peak, resulting in the increased I_D/I_G ratio.[60]

2.3.3 Effect of diffusion on the diameter and metallicity of SWCNT networks

The RBM peaks originated from out-of-plane vibration of the carbon atoms on the graphitic walls. As such, the wavenumbers of these features are inversely proportional to the tube's diameter[61]

$$\omega = 12.5 + 223.5/d \,, \tag{3}$$

where *d* is the diameter of the nanotube (nm) and *ω* is the wavenumber of the corresponding RBM peak position (cm^{-1}). By analyzing the RBM peak positions of individual spectra, the average diameter of the nanotubes in each sample can be calculated, as plotted in Figure 2.7a.

The tube diameters extrapolated from the RBM analysis indicated that the average nanotube diameter decreased to a minimum of 1.36 nm when the Al_2O_3 top layer had a thickness of 20 nm. The observed decrease of the tube diameter between 5 and 20 nm of Al_2O_3 could be attributed to the suppression of nanoparticle coarsening and coagulation by the top layer. On the other hand, a noticeable increase in the nanotube diameter was observed when the top Al_2O_3 layer was thicker than 20 nm. This indicated that the catalytically active nanoparticles formed on thicker Al_2O_3 top layers had a larger average diameter. Though the exact mechanism is still to be understood, a possible explanation to this phenomenon could be due to the presence of a large number of grain boundaries in thicker Al_2O_3 layers, which provided effective diffusion pathways for Fe catalyst.[38] These grain boundaries guided the diffusional pathways of the Fe atoms, leading to the precipitation of larger catalyst nanoparticles (albeit at a low density) on the top surface; thus the resulting SWCNTs would feature a larger average diameter. It is also possible that when the number of Fe atoms on the surface was reduced, the nucleation of a high density of small catalyst nanoparticles were suppressed so that only a few large particles were formed.

The diameter ranges as determined above showed the values from 1.0 to 2.0 nm for all samples. In this range, it has been reported that nanotubes resonate with roughly equal populations of both semiconducting and metallic types using the 633 nm laser excitation (514 nm laser excitation gave little RBM peaks on all samples).[3] The RBM of Raman spectra was then divided into three regions according to the Kataura plot.[62] The regions at 110 – 160 cm^{-1} and 240 – 300 cm^{-1} corresponded to the energy transition of E_{33}^S and E_{22}^S of semiconducting SWCNTs; whereas the regions between 160 and 240 cm^{-1} corresponded to the E_{11}^M transition of the metallic nanotubes.[42] The fractional percentage of m-SWCNTs in the networks were then determined by comparing the integrated area

under regions of E_{33}^{S}, E_{22}^{S} and E_{11}^{M}, as plotted in Figure 2.8b.[63] This plot showed a particular feature that the metallic fraction of SWCNTs grown on catalysts with 10 and 20 nm thick Al_2O_3 top layers (>40%) was much higher than in other cases (~20%).

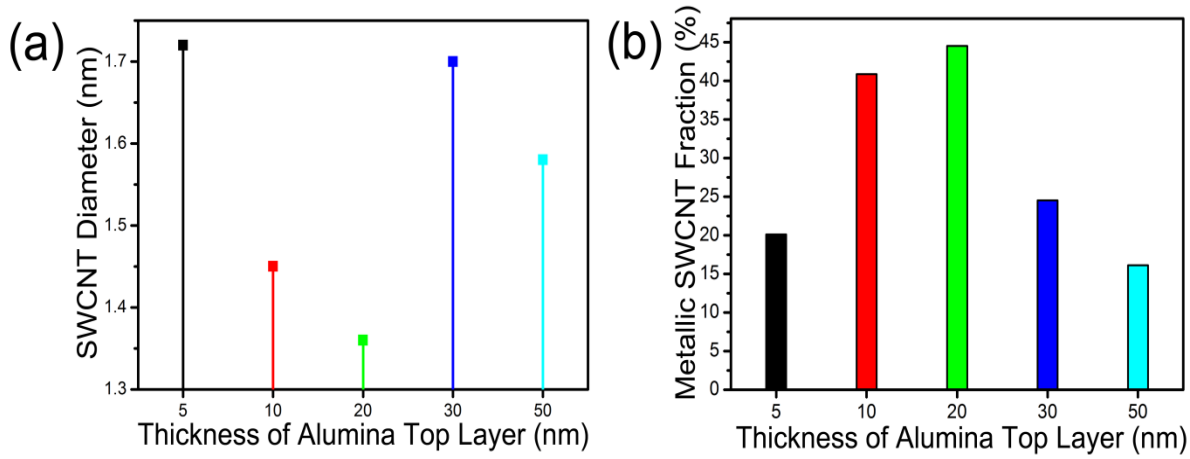

Figure 2.8 *Plots of (a) the average SWCNT diameter and (b) the metallic SWCNT fraction as a function of Al_2O_3 top layer's thickness.*[1]

It has been known that the preferential growth of m-SWCNTs *via* a CVD process is very challenging. This is due to the fact that m-SWNTs, with their higher reactivity and fewer contributing chiralities, are easier to be suppressed and removed.[64] By controlling the thickness of the top Al_2O_3 layer, the metallicity could be increased by over 20%. Two contributions might have resulted in this observed high metallicity. Firstly, as mentioned above, the diffusion of Fe through thicker Al_2O_3 layers gave rise to metallic Fe in the *γ*-phase.[44] *γ*-phase Fe was found to favour the growth of SWCNTs with an armchair chirality, which always feature metallic behaviours.[20] Secondly, it was shown that Fe nanoparticles after Ostwald ripening tended to exhibit larger diameter and less clear faceting, and were less likely to yield metallic SWCNTs.[43] As discussed above, the samples with 10 – 20 nm Al_2O_3 top layer produced the optimum catalyst particle size and were most effective at inhibiting the Ostwald ripening effect. These factors together allowed the catalyst structures to yield a higher portion of m-SWCNTs in the grown networks.

Although further studies with more laser excitations in the Raman measurements and/or advanced characterization techniques such as transmission electron microscopy (TEM) and photoluminescence

excitation (PLE) are needed, the present results clearly demonstrated that this tri-layered catalyst system offered a simple and effect way to control the growth of SWCNT networks.

2.4 Chapter Conclusion

In this chapter, I presented the current challenge in controlling the growth of CNTs and the problem this pose on the conductive behaviour of the as-grown tubes. As a response, a method to control the as-grown SWCNTs was demonstrated. By using a tri-layered catalyst system, the density, diameter, and conductivity of the as-grown SWCNT networks can be controlled by varying the thickness of the Al_2O_3 top layer. The mechanism behind this controllability is based on the interfacial diffusion of Fe atoms through the Al_2O_3 top layer to nucleate the nanotubes. The ability to manipulate the interfacial diffusion and reduce the effect of Ostwald ripening allowed us to effectively control the density of SWCNT networks from 0.18 to 35 tubes/μm^2, to vary the nanotube's diameters from 1.72 to 1.36 nm, and to increase the fraction of m-SWCNTs in the network from 20% to nearly 45%. This method allows us to influence the growth of SWCNTs and could be promising for the development of advanced SWCNT-based devices for a variety of applications.

2.5 References

[1] Yick S., Han Z. J., Ostrikov K. **Controlled Growth of Single-Walled Carbon Nanotube Networks by Catalyst Interfacial Diffusion**. *Adv. Mater. Inter.* 2014;10.1002/admi.201300151.

[2] Pint C. L., Nicholas N., Pheasant S. T. *et al.* **Temperature and gas pressure effects in vertically aligned carbon nanotube growth from Fe–Mo catalyst**. *J. Phys. Chem. C*. 2008; 112 (36): 14041-51.

[3] Han Z. J., Yick S., Levchenko I. *et al.* **Controlled synthesis of a large fraction of metallic single-walled carbon nanotube and semiconducting carbon nanowire networks**. *Nanoscale*. 2011; 3 (8): 3214-20.

[4] Sun C. Q., Bai H. L., Tay B. K. *et al.* **Dimension, strength, and chemical and thermal stability of a single C–C bond in carbon nanotubes**. *J. Phys. Chem. B*. 2003; 107 (31): 7544-6.

[5] Wildoer J. W. G., Venema L. C., Rinzler A. G. *et al.* **Electronic structure of atomically resolved carbon nanotubes**. *Nature*. 1998; 391 (6662): 59-62.

[6] Ates E. S., Kucukyildiz S., Unalan H. E. **Zinc Oxide Nanowire Photodetectors with Single-Walled Carbon Nanotube Thin-Film Electrodes**. *ACS Appl. Mater. Interfaces*. 2012; 4 (10): 5142-6.

[7] Chen Z., Yang Y., Chen F. *et al.* **Controllable interconnection of single-walled carbon nanotubes under AC electric field**. *J. Phys. Chem. B*. 2005; 109 (23): 11420-3.

[8] Wu Z., Chen Z., Du X. *et al.* **Transparent, conductive carbon nanotube films**. *Science*. 2004; 305 (5688): 1273-6.

[9] Park H., Afzali A., Han S. J. *et al.* **High-density integration of carbon nanotubes via chemical self-assembly**. *Nat. Nanotechnol.* 2012; 7 (12): 787-91.

[10] Rouhi N., Jain D., Burke P. J. **High-performance semiconducting nanotube inks: progress and prospects**. *ACS Nano*. 2011; 5 (11): 8471-87.

[11] Naeemi A., Meindl J. D. **Carbon nanotube interconnects**. *Annu. Rev. Mater. Res.* 2009; 39 (1): 255-75.

[12] Jourdain V., Bichara C. **Current understanding of the growth of carbon nanotubes in catalytic chemical vapour deposition**. *Carbon*. 2013; 58 (0): 2-39.

[13] Penev E. S., Artyukhov V. I., Yakobson B. I. **Extensive Energy Landscape Sampling of Nanotube End-Caps Reveals No Chiral-Angle Bias for Their Nucleation**. *ACS Nano*. 2014;10.1021/nn406462e.

[14] Yao Y., Li Q., Zhang J. *et al.* **Temperature-mediated growth of single-walled carbon-nanotube intramolecular junctions**. *Nat. Mater.* 2007; 6 (4): 283-6.

[15] Börjesson A., Bolton K. **First Principles Studies of the Effect of Ostwald Ripening on Carbon Nanotube Chirality Distributions**. *ACS Nano*. 2011; 5 (2): 771-9.

[16] Rao R., Liptak D., Cherukuri T. *et al.* **In situ evidence for chirality-dependent growth rates of individual carbon nanotubes**. *Nat. Mater.* 2012; 11 (3): 213-6.

[17] Dumlich H., Reich S. **Chirality-dependent growth rate of carbon nanotubes: A theoretical study**. *Phys. Rev. B*. 2010; 82 (8): 085421.

[18] Liu Y., Dobrinsky A., Yakobson B. I. **Graphene Edge from Armchair to Zigzag: The Origins of Nanotube Chirality?** *Phys. Rev. Lett.* 2010; 105 (23): 235502.

[19] Bachilo S. M., Balzano L., Herrera J. E. *et al.* **Narrow (n,m)-Distribution of Single-Walled Carbon Nanotubes Grown Using a Solid Supported Catalyst**. *J. Am. Chem. Soc.* 2003; 125 (37): 11186-7.

[20] Kohno H., Komine T., Hasegawa T. *et al.* **Formation of a carbon nanoribbon by spontaneous collapse of a carbon nanotube grown from a γ-Fe nanoparticle via an origami mechanism**. *Nanoscale*. 2013; 5 (2): 570-3.

[21] Evans J. W., Thiel P. A., Bartelt M. C. **Morphological evolution during epitaxial thin film growth: Formation of 2D islands and 3D mounds**. *Surface Science Reports*. 2006; 61 (1–2): 1-128.

[22] Keidar M., Raitses Y., Knapp A., Waas A. M. **Current-driven ignition of single-wall carbon nanotubes**. *Carbon*. 2006; 44 (5): 1022-4.

[23] Kang S. J., Kocabas C., Ozel T. *et al.* **High-performance electronics using dense, perfectly aligned arrays of single-walled carbon nanotubes**. *Nat. Nanotechnol.* 2007; 2 (4): 230-6.

[24] Arnold M. S., Green A. A., Hulvat J. F. *et al.* **Sorting carbon nanotubes by electronic structure using density differentiation**. *Nat. Nanotechnol.* 2006; 1 (1): 60-5.

[25] Wei D., Liu Y., Cao L. *et al.* **Selective electrochemical etching of single-walled carbon nanotubes**. *Adv. Funct. Mater.* 2009; 19 (22): 3618-24.

[26] Bekyarova E., Itkis M. E., Cabrera N. *et al.* **Electronic properties of single-walled carbon nanotube networks**. *J. Am. Chem. Soc.* 2005; 127 (16): 5990-5.

[27] Gómez-Navarro C., Pablo P. J. D., Gómez-Herrero J. *et al.* **Tuning the conductance of single-walled carbon nanotubes by ion irradiation in the Anderson localization regime**. *Nat. Mater.* 2005; 4 (7): 534-9.

[28] Geng H.-Z., Kim K. K., So K. P. *et al.* **Effect of acid treatment on carbon nanotube-based flexible transparent conducting films**. *J. Am. Chem. Soc.* 2007; 129 (25): 7758-9.

[29] Barman S. N., LeMieux M. C., Baek J. *et al.* **Effects of Dispersion Conditions of Single-Walled Carbon Nanotubes on the Electrical Characteristics of Thin Film Network Transistors**. *ACS Appl. Mater. Interfaces*. 2010; 2 (9): 2672-8.

[30] Hong S., Myung S. **Nanotube Electronics: A flexible approach to mobility**. *Nat. Nanotechnol.* 2007; 2 (4): 207-8.

[31] Zhou X., Park J.-Y., Huang S. *et al.* **Band Structure, Phonon Scattering, and the Performance Limit of Single-Walled Carbon Nanotube Transistors**. *Phys. Rev. Lett.* 2005; 95 (14): 146805.

[32] Chiang W.-H., Mohan Sankaran R. **Linking catalyst composition to chirality distributions of as-grown single-walled carbon nanotubes by tuning Ni_xFe_{1-x} nanoparticles**. *Nat. Mater.* 2009; 8 (11): 882-6.

[33] Kanzow H., Ding A. **Formation mechanism of single-wall carbon nanotubes on liquid-metal particles**. *Phys. Rev. B*. 1999; 60 (15): 11180-6.

[34] Fouquet M., Bayer B. C., Esconjauregui S. *et al.* **Highly chiral-selective growth of single-walled carbon nanotubes with a simple monometallic Co catalyst**. *Phys. Rev. B*. 2012; 85 (23): 235411.

[35] Volotskova O., Fagan J. A., Huh J. Y. *et al.* **Tailored distribution of single-wall carbon nanotubes from arc plasma synthesis using magnetic fields**. *ACS Nano*. 2010; 4 (9): 5187-92.

[36] Nessim G. D. **Properties, synthesis, and growth mechanisms of carbon nanotubes with special focus on thermal chemical vapor deposition**. *Nanoscale*. 2010; 2 (8): 1306-23.

[37] Picher M., Anglaret E., Arenal R., Jourdain V. **Processes controlling the diameter distribution of single-walled carbon nanotubes during catalytic chemical vapor deposition**. *ACS Nano*. 2011; 5 (3): 2118-25.

[38] Amama P. B., Pint C. L., Kim S. M. *et al.* **Influence of alumina type on the evolution and activity of alumina-supported Fe catalysts in single-walled carbon nanotube carpet growth**. *ACS Nano*. 2010; 4 (2): 895-904.

[39] Kim S. M., Pint C. L., Amama P. B. *et al.* **Evolution in catalyst morphology leads to carbon nanotube growth termination**. *J. Phys. Chem. Lett.* 2010; 1 (6): 918-22.

[40] Song W., Jeon C., Kim Y. S. *et al.* **Synthesis of bandgap-controlled semiconducting single-walled carbon nanotubes**. *ACS Nano*. 2010; 4 (2): 1012-8.

[41] Huang S., Cai X., Liu J. **Growth of millimeter-long and horizontally aligned single-walled carbon nanotubes on flat substrates**. *J. Am. Chem. Soc.* 2003; 125 (19): 5636-7.

[42] Robertson J., Zhong G., Telg H. *et al.* **Growth and characterization of high-density mats of single-walled carbon nanotubes for interconnects**. *Appl. Phys. Lett.* 2008; 93 (16): 163111.

[43] Harutyunyan A. R., Chen G., Paronyan T. M. *et al.* **Preferential growth of single-walled carbon nanotubes with metallic conductivity**. *Science*. 2009; 326 (5949): 116-20.

[44] Lenoble O., Bobo J. F., Kennet L. *et al.* **Structure, magnetism and thermal stability of Fe-Al_2O_3 multilayers**. *Thin Solid Films*. 1996; 275 (1–2): 64-8.

[45] Fei G. T., Barnes J. P., Petford-Long A. K. *et al.* **Structure and thermal stability of Fe : Al_2O_3 nanocomposite films**. *J. Phys. D: Appl. Phys.* 2002; 35 (9): 916-22.

[46] Hart A. J., Slocum A. H., Royer L. **Growth of conformal single-walled carbon nanotube films from Mo/Fe/Al_2O_3 deposited by electron beam evaporation**. *Carbon*. 2006; 44 (2): 348-59.

[47] Harding J. H., Atkinson K. J. W., Grimes R. W. **Experiment and theory of diffusion in alumina**. *J. Am. Ceram. Soc.* 2003; 86 (4): 554-59.

[48] Seidel R., Duesberg G. S., Unger E. *et al.* **Chemical vapor deposition growth of single-walled carbon nanotubes at 600°C and a simple growth model**. *J. Phys. Chem. B*. 2004; 108 (6): 1888-93.

[49] Edgeworth J. P., Wilson N. R., Macpherson J. V. **Controlled growth and characterization of two-dimensional single-walled carbon-nanotube networks for electrical applications**. *Small*. 2007; 3 (5): 860-70.

[50] Han Z. J., Levchenko I., Yick S., Ostrikov K. **3-Orders-of-magnitude density control of single-walled carbon nanotube networks by maximizing catalyst activation and dosing carbon supply**. *Nanoscale*. 2011; 3 (11): 4848-53.

[51] Kato T., Hatakeyama R. **Direct growth of short single-walled carbon nanotubes with narrow-chirality distribution by time-programmed plasma chemical vapor deposition**. *ACS Nano*. 2010; 4 (12): 7395-400.

[52] Ostrikov K., Mehdipour H. **Thin Single-Walled Carbon Nanotubes with Narrow Chirality Distribution: Constructive Interplay of Plasma and Gibbs-Thomson Effects**. *ACS Nano*. 2011; 5: 8372.

[53] Han Z. J., Mehdipour H., Li X. *et al.* **SWCNT networks on nanoporous silica catalyst support: morphological and connectivity control for nanoelectronic, gas-sensing, and biosensing devices**. *ACS Nano*. 2012; 6 (7): 5809-19.

[54] Orbaek A. W., Barron A. R. **Complications pertaining to the detection and characterization of individual and embedded single walled carbon nanotubes by scanning electron microscopy**. *Nanoscale*. 2013; 5 (7): 2790-7.

[55] Dresselhaus M. S., Dresselhaus G., Jorio A. *et al.* **Raman spectroscopy on isolated single wall carbon nanotubes**. *Carbon*. 2002; 40 (12): 2043-61.

[56] Strano M. S. **Probing chiral selective reactions using a revised kataura plot for the interpretation of single-walled carbon nanotube spectroscopy**. *J. Am. Chem. Soc.* 2003; 125 (51): 16148-53.

[57] Neyts E. C., van Duin A. C. T., Bogaerts A. **Changing chirality during single-walled carbon nanotube growth: a reactive molecular dynamics/Monte Carlo study**. *J. Am. Chem. Soc.* 2011; 133 (43): 17225-31.

[58] Ostrikov K., Neyts E. C., Meyyappan M. **Plasma nanoscience: from nano-solids in plasmas to nano-plasmas in solids**. *Adv. Phys.* 2013; 62 (2): 113-224.

[59] Lu C., Liu J. **Controlling the diameter of carbon nanotubes in chemical vapor deposition method by carbon feeding**. *J. Phys. Chem. B*. 2006; 110 (41): 20254-7.

[60] Baughman R. H., Zakhidov A. A., de Heer W. A. **Carbon nanotubes--the route toward applications**. *Science*. 2002; 297 (5582): 787-92.

[61] Bachilo S. M., Strano M. S., Kittrell C. *et al.* **Structure-assigned optical spectra of single-walled carbon nanotubes**. *Science*. 2002; 298 (5602): 2361-6.

[62] LeMieux M. C., Roberts M., Barman S. *et al.* **Self-sorted, aligned nanotube networks for thin-film transistors**. *Science*. 2008; 321 (5885): 101-4.

[63] Krupke R., Hennrich F., Löhneysen H. v., Kappes M. M. **Separation of metallic from semiconducting single-walled carbon nanotubes**. *Science*. 2003; 301 (5631): 344-7.

[64] Gavillet J., Loiseau A., Ducastelle F. *et al.* **Microscopic mechanisms for the catalyst assisted growth of single-wall carbon nanotubes**. *Carbon*. 2002; 40 (10): 1649.

3

Coupling Metal Nanostructures and Carbon Nanotube Arrays for Hydrogen Sensing

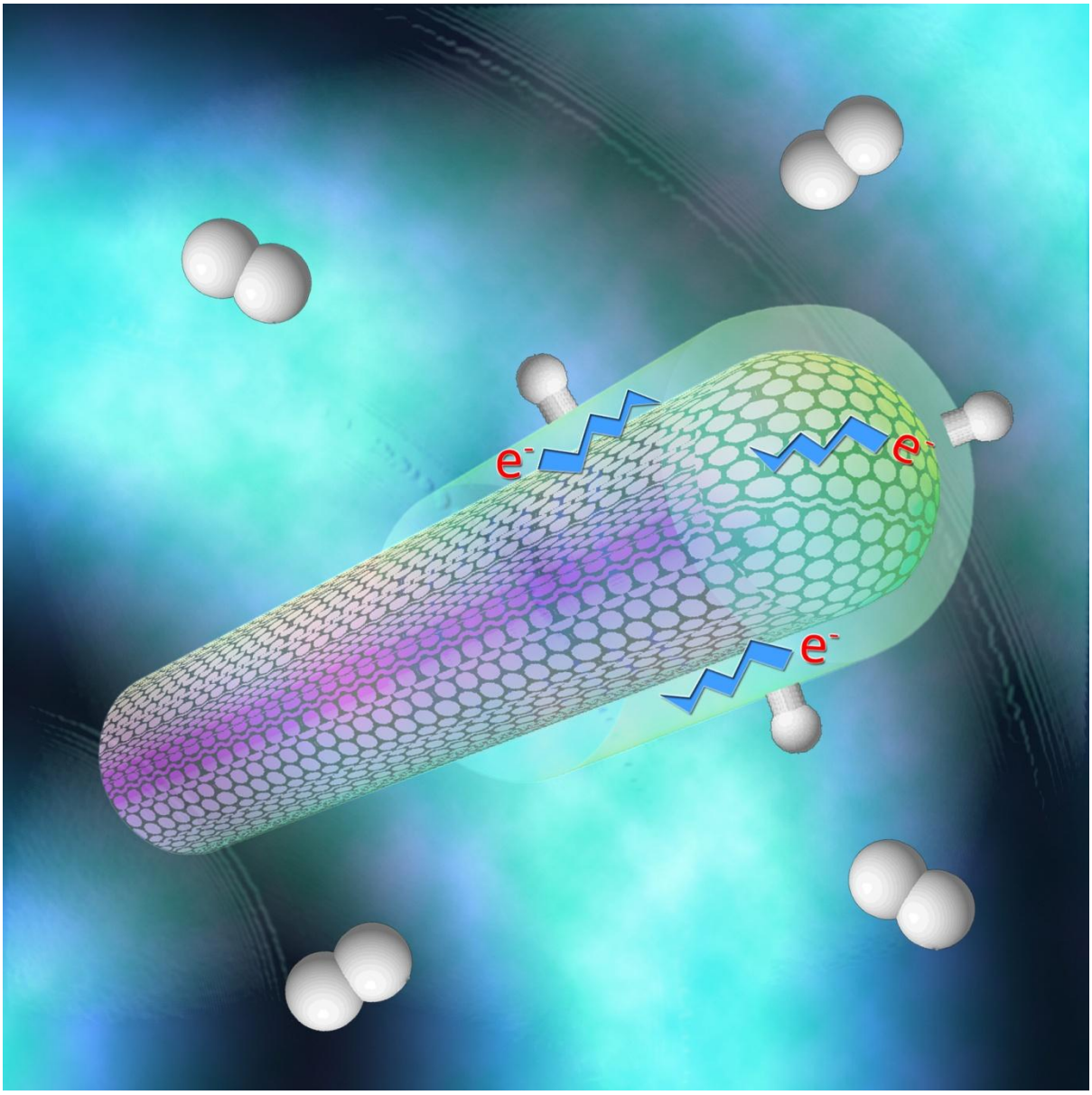

A schematic illustration showing electron surface scatterings caused by the CNT-Pd coreshell hybrid structure adsorption of H_2.

Chapter Summary

Upon the coupling with functional components, CNT-based hybrid nanomaterials have shown the ability to act as a sensing platform. However, in order for CNT-hybrid based sensor to be fully utilised, chiral independent and reversible sensing mechanisms are required. In this chapter, a core-shell hybrid nanowire structure was formed by sputtering palladium onto vertically aligned CNT arrays. The hybrid nanostructures exhibited resistive responses upon the exposure to hydrogen with an excellent baseline recovery at room temperature. The magnitude of the response was shown to be tuneable by an applied voltage. This demonstrates that the hydrogen response mechanism of the CNT-Pd core-shell hybrid nanostructure was due to electron scattering induced by physisorption of hydrogen rather than the charge-transfer mechanism commonly attributed to Pd nanoparticle-decorated single-walled CNTs. This chapter is based on the paper, "Physisorption-induced electron scattering on the surface of carbon-metal core-shell nanowire arrays for hydrogen sensing" by Yick *et. al.*[1]

3.1 Sensing with CNTs

The ability to accurately quantify an analyte is vital to many industries. This is especially true for the field of environmental monitoring, which is in constant demand for sensors with better performance (i.e. better sensitivity, quicker response and shorter recovery time). Broadly speaking, a sensor is composed of two modules, an active component which can exhibit an electrochemical or optical response upon the presences of the analyte and a system to extract these signals. CNTs are seen as a promising sensing platform as they possess high conductivity, good mechanical strength, and a large surface-to-volume ratio.[2-4] Pristine SWCNTs are extremely sensitive to charge transfer from their surroundings.[5] Therefore, the presences of electron donating species or electron withdrawing species can modulate the conductance of the tube.[6] Using this property, gas sensing devices based on pristine SWCNTs both as collective network or individual tubes have been fabricated. However, the usage of pristine CNTs as a chemical sensor faces numerous challenges. Firstly, for consistent

response, the tubes have to be semiconducting with a narrow band gap distribution which as mentioned in chapter two is non-trivial. The extra processing steps required would significantly increase the complexity and cost of production. Secondly, due to the chemical inertness of the graphitic sidewalls, there are only a limited range of analytes which CNTs can interact with. Lastly, CNTs can exhibit a strong physisorption mechanism. This significantly degrades the reversibility of the sensing interaction and increase their recovery time which hinders their practical usage.[7]

In order to overcome these problems, CNTs are often functionalised prior to being used as a sensor. There are two general approaches in functionalising CNTs. Firstly, foreign atoms such as nitrogen and boron are directly incorporated into the graphitic lattice.[8] By doping CNTs, they have displayed enhanced electrocatalytic activity to oxygen reduction reactions and can respond to the presences of biomolecules.[9] However, the doping process often employs undesirable and toxic agents such as NH_3 and BF_3.[10,11] Furthermore, the presences of foreign atoms in the graphitic lattice can compromise their physical properties as discussed in Chapter 1.[12] Alternatively, CNTs can be combined with foreign structures such as metallic nanostructure to form hybrid materials. The feasibility of a sensing device based on CNT-metal hybrid structure was first demonstrated in hydrogen sensing by *Kong et al*.[13] In their work, SWCNTs were decorated with palladium nanoparticles. Upon the exposure to H_2, the Pd nanoparticles modulated the conductance of the tubes via electron transfer.

However, despite recent progress, the device performance of CNT-based sensor had yet been sufficient for commercial applications.[14] Firstly, SWCNT based sensors which utilise the charge-transfer sensing mechanism are hampered by the chiral diversity of unsorted tubes, as the heterogeneous band gap prevents uniform response. Secondly, the coupling between the two materials in the CNT-hybrid requires further optimization. For example, the formation of Schottky barrier between the decorating metal nanostructure and CNTs can impede the charge transfer. These issues need to be resolved before applying CNTs into commercially viable gas sensors.

In this chapter, the application of CNT-based hybrid materials as a gas sensor is examined. In particular, their application as a hydrogen sensing devices will be studied. H_2 can potential be source of clean energy which can replace fossil fuel. Their attraction lies in its high energy density and zero carbon emission during combustion.[15] However, being an explosive gas with both a low minimum ignition energy and wide flammable range, the monitoring of H_2 is necessary for its wide-spread utilization.[16,17]

Nominally, metallic palladium is used as the active component for hydrogen sensing. Upon being exposed to H_2, the gas is dissociates by the surface of the Pd and the atomic hydrogen incorporated into its lattice. This reversible structural transformation results in a change to the electrical resistance and lattice properties of the metal. Based on this principle, resistive H_2 sensor using a thin film of Pd was demonstrated.[18] Despite this success, the key performance indicators of such devices (i.e., response stability, H_2 sensitivity and responses time) still need to be substantially improved to satisfy numerous requirements in applications.[19]

H_2 sensor based on Pd nanowires have demonstrated superior performance in comparison to their thin-film counterparts.[20] The observed improvement is attributed to the increased surface-to-volume ratio and quantum confinement effect.[21] These factors allow the Pd nanowires to exhibit shorter response time and higher sensitivity.[22,23] Current methods of production are dominated by two approaches, namely nanoscale patterning and template synthesis. The former utilises lithography or selective etching to transform thin films into one-dimensional nanostructures.[24-26] Although these technique can directly integrate the Pd nanowires into devices, their resolutions are limited to hundreds of nanometres.[27] The latter approach involves the deposition of Pd onto templates with pre-formed nanoscale features.[28,29] However, the desired nanostructures often require a labour intensive extraction and assembly process prior to use. As the device requires simple synthetic methods that can be scaled for large areas and quantities,[30] the complexity in production and device fabrication has hindered the applications of Pd nanowires hydrogen sensors.

Here, I demonstrate how a carbon-metal core-shell hybrid nanostructure can resolve the aforementioned issues associated with both Pd-based and CNT-based hydrogen sensors. The good wettability between Pd and CNTs allows the formation of a continuous cladding around the tubes.[31] By encapsulating CNTs in another material, a core-shell hybrid structure is produced. Such hybrid nanostructures retain the merits of CNTs and provide additional properties specific to the coating. As a result, the complementary integration of the two materials yields core-shell nanostructures highly desirable for various applications.[32-35] Additionally, the growth of CNTs was tuned to result in closed-packed vertically aligned arrays. The array exhibits a larger specific surface area as compared to non-aligned CNTs. Furthermore, the conductivity of the forest also increases due to inter-tube contacts. Such features are highly desirable in sensing applications as they lead to an enhancement in sensitivity and reduction of the response time.[36-38] The CNT-Pd core-shell nanowire arrays display a significant variation in electrical resistance in the presence of H_2 as well as excellent recovery at room temperature. The magnitude of the response was also shown to vary with applied voltage. This implies that the mechanism for the hydrogen response exhibited by the core-shell nanowire arrays was due to the physisorption of H_2 by the Pd shell, which increases the electron scattering on the surface of the nanostructure. As compared to the commonly proposed charge-transfer mechanism found in SWCNT-based devices. This work thus illustrates a reversible, chiral independent sensing mechanism.

3.2 Methodology

Growth of CNT arrays. Vertically aligned CNT arrays were synthesized *via* a thermal chemical vapor deposition (TCVD) process. Briefly, a silicon wafer with a 500 nm thick oxide layer was sequentially sonicated in a bath of acetone and isopropyl alcohol respectively. The wafer was then washed with de-ionized water and baked at 110 °C for 5 minutes. A 10 nm buffer layer of alumina was deposited by reactively sputtering an Al target with an Ar/O_2 gas mixture. The catalyst layer was then formed by sputtering 1.8 nm thick iron layer onto the alumina-coated wafer. The Si wafer layered with the catalyst was cut into 1x1cm^2 pieces and inserted into the thermal furnace (MTI, OTF-1200X with a quartz tube 50 mm in diameter) and heated to 700°C in 35 min under an 800 sccm flow of Ar. Upon reaching the desired temperature, C_2H_2 and H_2 were introduced for 10 minutes at a rate of 56 and 240 sccm, respectively. The samples were finally cooled to room temperature under an Ar flow.

Deposition of Pd shell. Pd was deposited onto the CNT forests by magnetron sputtering. The thickness of the Pd was set to 15 nm to allow the formation of a continuous coating around each tube. The sample was annealed at 200 °C for 10 minutes in an Ar atmosphere.

Electrical Measurements. Au was sputtered on the Pd-CNT core-shell nanowire arrays through a shadow mask to form a pair of electrodes and electrical contacts were attached by silver paint. The device is depicted in figure 3.1 The resistance of the sample was measured in a Physical Property Measurement System (PPMS) Quantum Design model 6000 over a broad temperature range (4 -300 K). In order to investigate the voltage dependency of the sensor's response to H_2, we also swept the applied voltage from 0.002 to 8 V in 100% H_2 ambience.

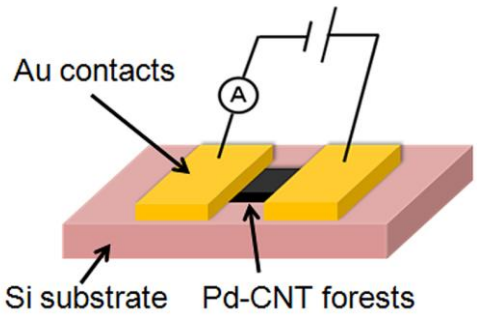

Figure 3.1 *Schematic of the electrical measurement setup for the H_2 sensing.*[1]

Gas Sensing Measurements. The hydrogen response of our core-shell structures was tested in a specially designed chamber. The core-shell structure was exposed to different H_2 concentration (0.5 -1% H_2 in N_2 ambient) at a constant voltage to determine their resistive response to the gas.

Characterisation Methods. The Pd-CNT hybrids were characterized using field-emission scanning electron microscopy (FE-SEM; Zeiss Ultraplus) operated at electron beam energies ranging from 15 to 20 keV with an InLens secondary electron detector. Elemental composition was determined via Energy-Dispersive X-ray spectroscopy (EDS) from the same system.

3.3 Results and Discussion

The morphology of the decorated CNT arrays was examined by the SEM as shown in Figure 3.2. From the cross-sectional SEM micrograph depicted in Figure 3.2 a, the average density of the CNT arrays was estimated at 3 to 5 $\times 10^{10}$ tubes/cm^2 with an average height of 40 µm. The SEM insets depicted the Pd-coated CNTs at various positions of the forest (Figures 3.2 b and c). From these micrographs, the metal coating showed to extended at least 1 µm beyond the tip of the CNT-array (Figure 3.2 c). The high-resolution SEM taken at the top of the forest showed the typical morphology of the Pd coating. The sputtered palladium was observed to form a continuous nano-shell around the CNTs rather than discrete nanoparticles (Figure 3.2 d). The composition of the coating material was determined to be Pd by EDS (Figure 3.2 e). These results confirmed that the CNTs were encapsulated by Pd.

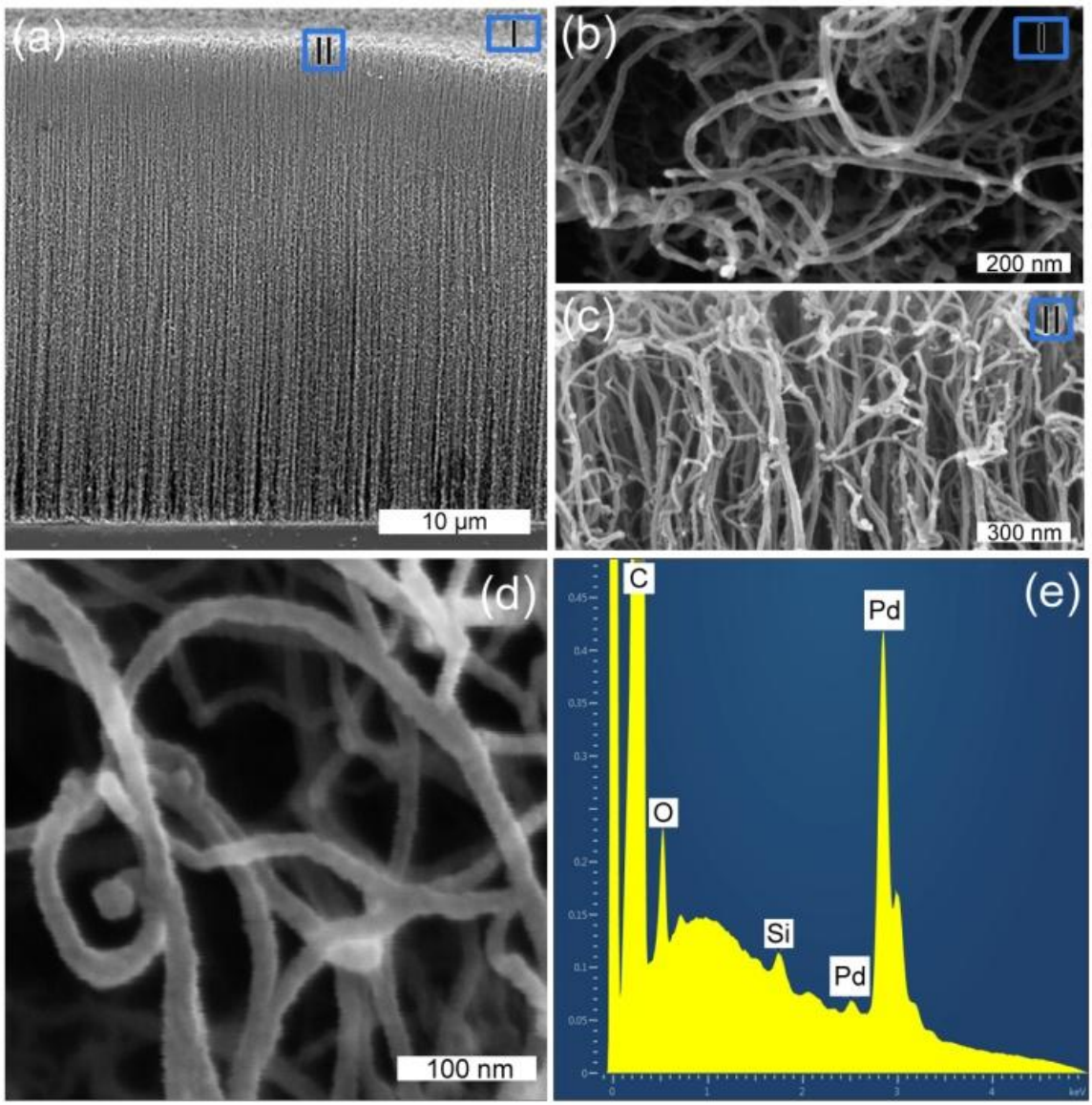

Figure 3.2 *SEM micrographs of the CNT-Pd core-shell nanowire arrays. (a) A cross-sectional SEM image of the Pd coated CNT arrays, with high magnifications at positions I (top view of the array), position II (cross sectional view of the tip of the decorated CNT array). These correspond to (b) and (c), respectively. (d) A high-resolution image of (b) to illustrate the continuous coating of Pd on the surface of CNTs. (e) The EDS spectrum taken at position I.*[1]

Figure 3.3 shows the resistance change of the CNT-Pd core-shell structure when exposed to different concentration of H_2 (0.05-1%) at room temperature. The sample demonstrated a stable resistive response and it was able to detect H_2 concentration as low as 0.05%. The response time (measured as the duration required to reach 37% of the peak response) of the hybrid structure was between 5-17 seconds. This remained consistent throughout the range of the H_2 concentrations tested. Upon the termination of

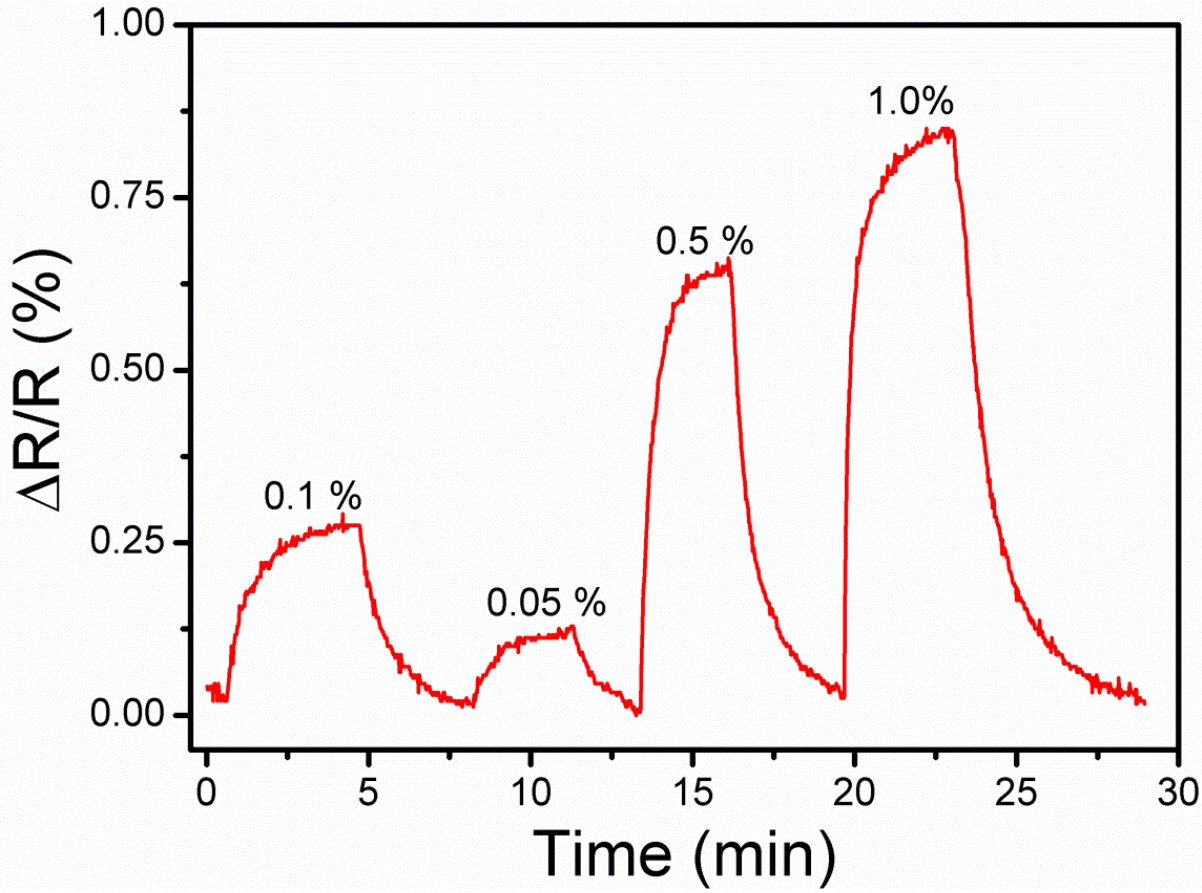

Figure 3.3 *Resistance variations in the CNT-Pd core-shell nanowires when exposed to different concentrations of H_2 gas at room temperature.*[1]

the H_2 gas flow, the hybrid nanostructure recovered within 2-5 minutes at room temperature and without the need of any external agitation or heating. These results demonstrate a significant reduction in response time when compared to other Pd-CNT structures, such as Pd decorated single-walled CNT films, Pd-decorated multi-walled CNT thin films, and Pd-decorated multi-walled CNT yarns, exposed to a similar H_2 concentration.[38-40]

In order to understand the sensing mechanism of the CNT-Pd core-shell nanowire arrays, the H_2 concentration was fixed at 100% while the resistive response of the hybrid structure was measured in room temperature at different voltages. Figure 3.4 shows that the magnitude of resistive change due to the presence of to H_2 increased as the applied voltage was increased.

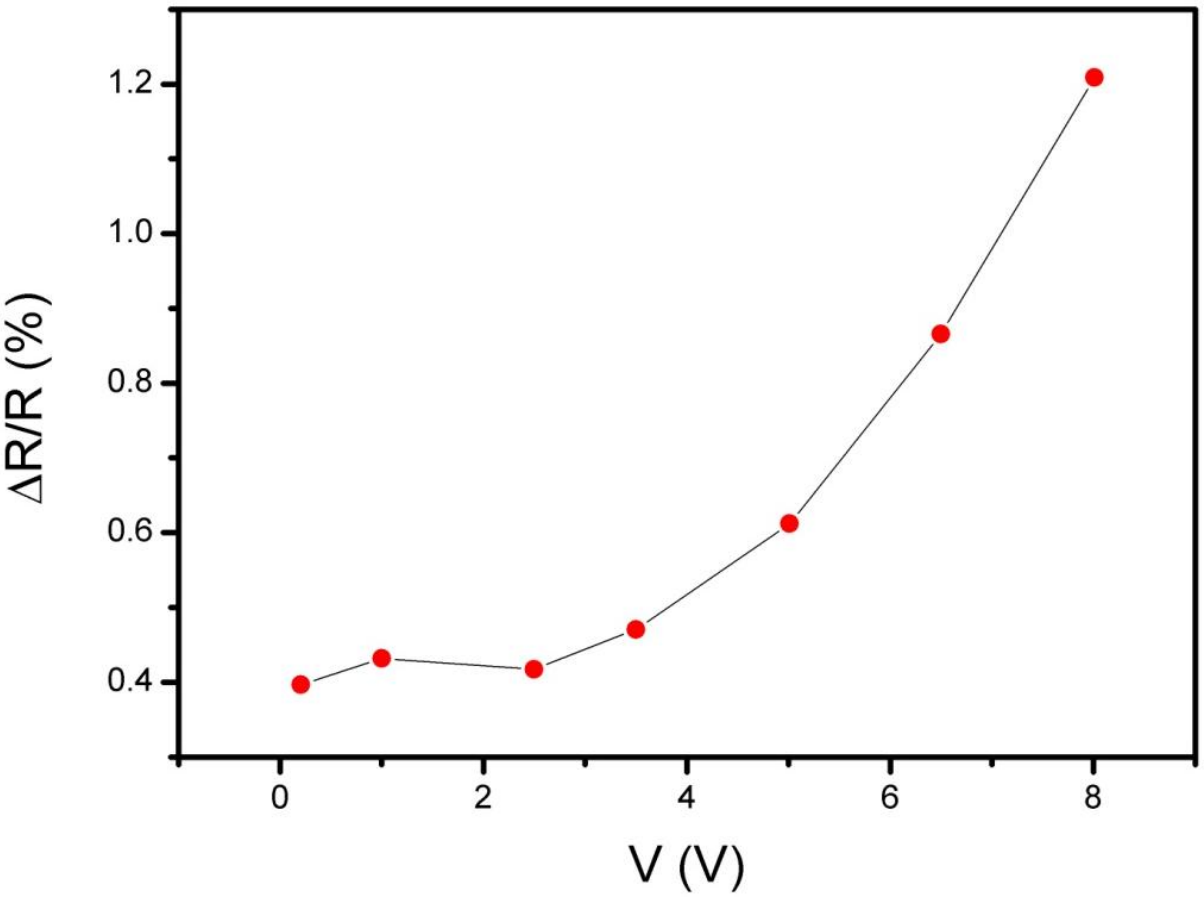

Figure 3.4 Resistance variations as a function of applied voltage as the CNT-Pd core-shell nanowire arrays were exposed to 100% of H_2 at room temperature.[1]

To understand the mechanism which enabled this trend, the resistance of the sample was measured at different applied voltages over a broad temperature range (4-300 K) in the absence of H_2. Figure 3.5 suggests that the conduction mechanism within the nano-hybrid array was due to thermally activated tunnelling. This could be seen by the variation between the dependencies of resistance with temperature as the applied voltage changed. Indeed, electrons require additional energy from phonons to overcome the Coulomb blockade at low voltages. As the temperature decreases, it becomes more difficult for electrons to overcome the Coulomb blockade and hence, the sample resistance increases. By applying higher voltages, the electrostatic energy of electrons will increase. Therefore, it becomes easier for electrons to overcome the Coulomb blockade; thus, the resistance variation becomes less sensitive to the variation of temperature.[41]

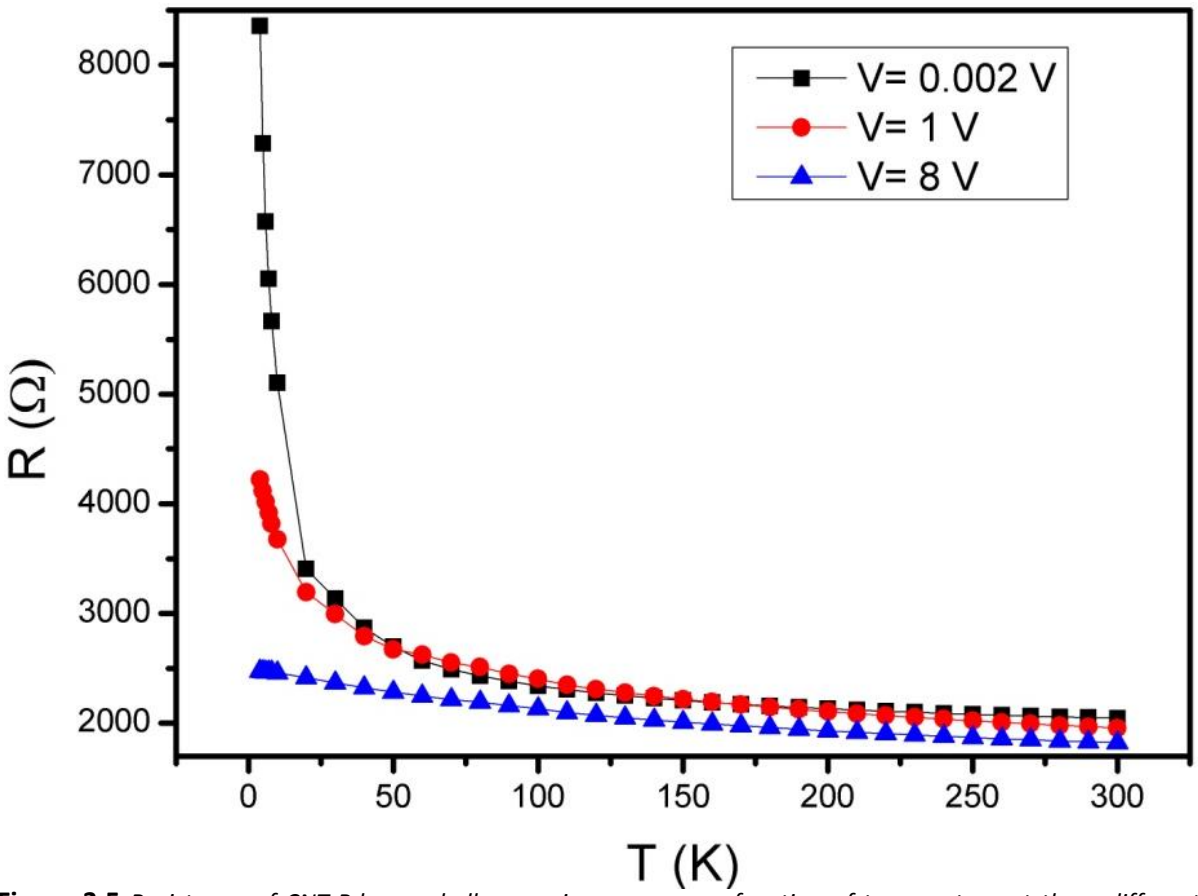

Figure 3.5 *Resistance of CNT-Pd core-shell nanowire arrays as a function of temperature at three different applied voltages in the absence of H_2.*[1]

This also indicates that any temperature change due to the physisorption of H_2 by Pd did not exert a significant effect on the sensing mechanism. For if the thermal effect was to dominate, the resistance variation should then be less sensitive to the applied voltage. However, Figure 3.4 clearly indicated that the resistance variation from the presences of H_2 was enhanced as the applied voltage increased. One can use the following equation to calculate the change of resistance at high temperatures:[41]

$$\Delta R = Ce^{\frac{E_C}{3kt}}, \qquad (3.1)$$

where C is a constant, E_c the Coulomb blockade energy, and k the Boltzmann constant. Figure 3.4 shows that the change of resistance at applied voltages of 0.002, 1.0, and 8.0 V were 0.4, 0.43, and 1.2%, respectively. At applied voltages of 0.002, 1.0, and 8.0 V by fitting Eq. (3.1) to the experimental data in a temperature range of 250-300 K, the calculated E_c are 12.88, 11.88, and 10.45 meV,

respectively. From Equation 3.1, the temperatures corresponding to the resistance change at applied voltages of 0.002, 1.0, and 8.0 *V* are 293, 291.8, and 275.6 K, respectively. This shows that the change of resistance is not due to a thermal effect, as the change of temperature due to interaction with H_2 does not depend on the applied voltages.

To explain the change of resistance upon the introduction of H_2, it is known that the surface potential of the Pd layer is changed upon the physisorption of H_2. Since the thickness of the Pd layer in the samples (15 nm) was comparable to the mean free path of electrons, electrons will encounter significant scattering from the surface. This implies that the resistance of the Pd layer becomes more sensitive to surface changes. As the total resistance of the sample is the sum of both the resistances of the Pd layer and the tunnelling resistances between the respective core-shell nanowires, by increasing the applied voltage the tunnel resistance will decrease.[41] Hence, resistance of the Pd layer becomes more important and consequently, the total resistance of the sample becomes more sensitive to H_2 at higher voltages.

The above results demonstrated that the H_2 interaction with the CNT-Pd carbon-metal core-shell nanostructure array is dominated by the resistive change to the Pd layer alone, with the CNTs acting as a conductive support. This differs from the common reports on H_2 response in Pd decorated CNTs, which attribute the sensing mechanism to a charge transfer between the two materials.[13,38] Such mechanism ascribed the hydrogen response of Pd-CNTs to the modulation of carrier population by charge transfer between Pd and CNTs. Upon the adsorption of H_2, the work function of Pd is lowered. This results in the injection of electrons from Pd to CNTs, which lowers the population of holes and results in a decrease of the conductance of the decorated structure. However, such mechanism makes the Pd-CNTs response sensitive to variation in the internal band structure (most prominent in as-grown single-walled CNTs with different tube diameters)[42] and external perturbation such as temperature flux and gaseous impurities (e.g., water vapor or oxygen) which could affect the charge transfer process. Furthermore, such interference from external perturbation

were shown to be more prevalent in CNT arrays.[43] By only utilizing the Pd layer for H_2 sensing, the core-shell nanostructure has the advantage of being less affected by the perturbation mentioned.

To understand how the sensor performance is impacted by the coupling between the Pd and the CNTs, the morphology of the Pd nanostructure was altered via annealing at a higher temperature. By increasing the annealing temperature to 500°C, the Pd cladding precipitated into nanoparticles with an average diameter of 80 nm as seen in Figure 3.6a. This change in morphology led to a change in the sensing mechanism and device performance as observed in Figure 3.6b. Contrary to the performance exhibited by the core-shell structure as seen in Figure 3.3 the resistance of the nanocomposite decreased non-reversibly in proportion to the concentration of H_2 present.

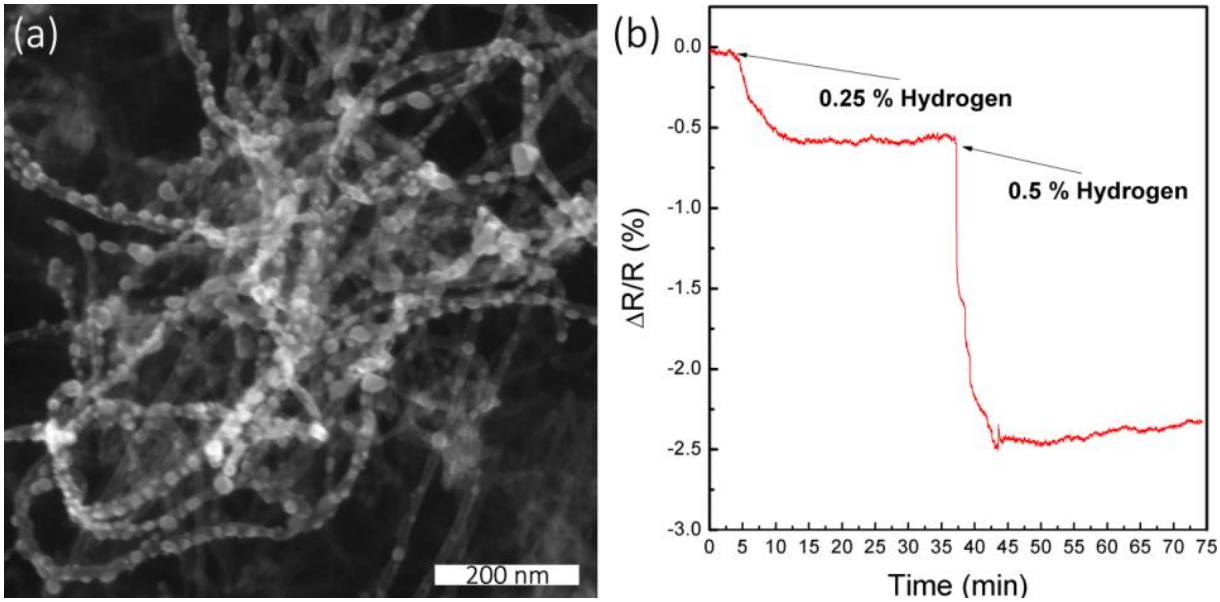

Figure 3.6 *SEM micrographs of the CNT-Pd nanocomposite annealed at 500°C (a). Resistance variations of the CNT-Pd nanocomposite when exposed to different concentrations of H_2 gas (b).*

The difference in device performance reflects the different sensing mechanisms of the materials. For a discontinuous Pd structure, H_2 sensing occurs via hydrogen-induced lattice expansion during the phase transformation of palladium hydride.[44,45] Initially, the absorption of H_2 forms a solid solution with the bulk material, leading to the α-phase palladium hydride. As more hydrogen atoms are incorporated into the material, β-PdH is formed. This phase shift occurs when the hydrogen atoms distort the crystal lattice of Pd by occupying the interstitial site. This leads to a localised swelling in

proportion to the H_2 concentration.[20,46] As the PdH lattice expands, the resistance decreases due to the fact that the enlarged Pd nanoparticles are in closer proximity to each other which increases conduction. Though the phase transformation process is often reported as reversible, it is likely that the swelling of the nanoparticle caused local changes to the supporting CNTs which prevented a reversible response. Therefore the hydrogen response displayed in Figure 3.3 also served as indirect evidences for the continuous nature of the Pd nano-shell.

3.4 Chapter Conclusion

In this chapter, the two issues namely, chiral dependent mechanism and irreversible sensing which prevents CNTs from being used in gas-sensors were presented. CNT-Pd core-shell nanowire arrays were shown to overcome these issues. The core-shell nanowire arrays configuration utilises the change in surface scattering of the Pd nano-shell to detect the quantity of H_2 present. This negated the problems with chirality dependency required by charge-transfer mechanism. This approach gives rise to an array of carbon-metal core-shell nanowires which could be used without further assembly. As the formation of both the vertically aligned array architecture and the Pd encapsulation were self-assembled, this method is both cost and labour efficient. This is significant for the continued development of next-generation sensors as it provides a method to fabricate ready-to-use arrays of carbon-metal core-shell nanowires which could be readily incorporated into the existing and emerging sensing platforms.

3.5 Reference

[1] Yick S., Yajadda M. M. A., Bendavid A. *et al.* **Physisorption-induced electron scattering on the surface of carbon-metal core-shell nanowire arrays for hydrogen sensing**. *Appl. Phys. Lett.* 2013; 102 (23): 233111.

[2] Collins P. G., Avouris P. The electronic properties of carbon nanotubes. In: Saito S, Zettl A, eds. Contemporary Concepts of Condensed Matter Science: Elsevier 2008, p. 49-81.

[3] Yu M. F., Lourie O., Dyer M. J. *et al.* **Strength and Breaking Mechanism of Multiwalled Carbon Nanotubes Under Tensile Load**. *Science*. 2000; 287 (5453): 637-40.

[4] Keidar M., Raitses Y., Knapp A., Waas A. M. **Current-driven ignition of single-wall carbon nanotubes**. *Carbon*. 2006; 44 (5): 1022-4.

[5] Collins P. G., Bradley K., Ishigami M., Zettl A. **Extreme Oxygen Sensitivity of Electronic Properties of Carbon Nanotubes**. *Science*. 2000; 287 (5459): 1801-4.

[6] Kong J., Franklin N. R., Zhou C. *et al.* **Nanotube Molecular Wires as Chemical Sensors**. *Science*. 2000; 287 (5453): 622-5.

[7] Ting Z., et al. **Recent progress in carbon nanotube-based gas sensors**. *Nanotechnology*. 2008; 19 (33): 332001.

[8] Stephan O., Ajayan P. M., Colliex C. *et al.* **Doping Graphitic and Carbon Nanotube Structures with Boron and Nitrogen**. *Science*. 1994; 266 (5191): 1683-5.

[9] Xu X., Jiang S., Hu Z., Liu S. **Nitrogen-Doped Carbon Nanotubes: High Electrocatalytic Activity toward the Oxidation of Hydrogen Peroxide and Its Application for Biosensing**. *ACS Nano*. 2010; 4 (7): 4292-8.

[10] Mondal K. C., Coville N. J., Witcomb M. J. *et al.* **Boron mediated synthesis of multiwalled carbon nanotubes by chemical vapor deposition**. *Chem. Phys. Lett.* 2007; 437 (1–3): 87-91.

[11] Gong K., Du F., Xia Z. *et al.* **Nitrogen-Doped Carbon Nanotube Arrays with High Electrocatalytic Activity for Oxygen Reduction**. *Science*. 2009; 323 (5915): 760-4.

[12] Cruz-Silva E., López-Urías F., Muñoz-Sandoval E. *et al.* **Electronic Transport and Mechanical Properties of Phosphorus- and Phosphorus–Nitrogen-Doped Carbon Nanotubes**. *ACS Nano*. 2009; 3 (7): 1913-21.

[13] Kong J., Chapline M. G., Dai H. **Functionalized Carbon Nanotubes for Molecular Hydrogen Sensors**. *Adv. Mater.* 2001; 13 (18): 1384-6.

[14] Fam D. W. H., Palaniappan A., Tok A. I. Y. *et al.* **A review on technological aspects influencing commercialization of carbon nanotube sensors**. *Sensors and Actuators B: Chemical*. 2011; 157 (1): 1-7.

[15] Jeon K. J., et al. **Air-stable magnesium nanocomposites provide rapid and high-capacity hydrogen storage without using heavy-metal catalysts**. *Nat. Mater.* 2011; 10 (4): 286-90.

[16] Boon-Brett L., Bousek J., Castello P. *et al.* **Reliability of commercially available hydrogen sensors for detection of hydrogen at critical concentrations: Part I - Testing facility and methodologies**. *Int J. Hydr. Energy*. 2008; 33 (24): 7648-57.

[17] Buttner W. J., Post M. B., Burgess R., Rivkin C. **An overview of hydrogen safety sensors and requirements**. *Int J. Hydr. Energy*. 2011; 36 (3): 2462-70.

[18] Hughes R. C., Schubert W. K. **Thin films of Pd/Ni alloys for detection of high hydrogen concentrations**. *J. Appl. Phys.* 1992; 71 (1): 542-4.

[19] Hübert T., Boon-Brett L., Black G., Banach U. **Hydrogen sensors - A review**. *Sensors and Actuators B: Chemical*. 2011; 157 (2): 329-52.

[20] Favier F., Walter E. C., Zach M. P. *et al.* **Hydrogen Sensors and Switches from Electrodeposited Palladium Mesowire Arrays**. *Science*. 2001; 293 (5538): 2227-31.

[21] Yang F., Kung S. C., Cheng M. *et al.* **Smaller is Faster and More Sensitive: The Effect of Wire Size on the Detection of Hydrogen by Single Palladium Nanowires**. *ACS Nano*. 2010; 4 (9): 5233-44.

[22] Jeon K. J., Jeun M., Lee E. *et al.* **Finite size effect on hydrogen gas sensing performance in single Pd nanowires**. *Nanotechnology*. 2008; 19 (49): 495501.

[23] Zeng X. Q., Latimer M. L., Xiao Z. L. *et al.* **Hydrogen Gas Sensing with Networks of Ultrasmall Palladium Nanowires Formed on Filtration Membranes**. *Nano Lett.* 2010; 11 (1): 262-8.

[24] Jeon K. J., Lee J. M., Lee E., Lee W. **Individual Pd nanowire hydrogen sensors fabricated by electron-beam lithography**. *Nanotechnology*. 2009; 20 (13): 135502.

[25] Offermans P., Tong H. D., van Rijn C. J. M. *et al.* **Ultralow-power hydrogen sensing with single palladium nanowires**. *Appl. Phys. Lett.* 2009; 94 (22): 223110-3.

[26] Xu S., *et al*. **Self-organized vertically aligned single-crystal silicon nanostructures with controlled shape and aspect ratio by reactive plasma etching**. *Appl. Phys. Lett.* 2009; 95 (11): 111505.

[27] Yang P., Yan R., Fardy M. **Semiconductor Nanowire: What's Next?** *Nano Lett.* 2010; 10 (5): 1529-36.

[28] Walter E. C., Favier F., Penner R. M. **Palladium Mesowire Arrays for Fast Hydrogen Sensors and Hydrogen-Actuated Switches**. *Anal. Chem.* 2002; 74 (7): 1546-53.

[29] Monzón-Hernández D., Luna-Moreno D., Martínez-Escobar D. **Fast response fiber optic hydrogen sensor based on palladium and gold nano-layers**. *Sensors and Actuators B: Chemical*. 2009; 136 (2): 562-6.

[30] Cvelbar U., Chen Z., Sunkara M. K., Mozetič M. **Spontaneous Growth of Superstructure α-Fe2O3 Nanowire and Nanobelt Arrays in Reactive Oxygen Plasma**. *Small*. 2008; 4 (10): 1610-4.

[31] Lee S., Kahng S. J., Kuk Y. **Nano-level wettings of platinum and palladium on single-walled carbon nanotubes**. *Chem. Phys. Lett.* 2010; 500 (1–3): 82-5.

[32] Yang H. Y., Yu S. F., Liang H. K. *et al.* **High-temperature lasing characteristics of randomly assembled SnO[sub 2] backbone nanowires coated with ZnO nanofins**. *J. Appl. Phys.* 2009; 106 (12): 123105-5.

[33] Yu J., Sow C. H., Wee A. T. S., Chua D. H. C. **Enhanced field emission of vertically aligned core-shelled carbon nanotubes with molybdenum oxide encapsulation**. *J. Appl. Phys.* 2009; 105 (11): 114320.

[34] Yang Y., Qu L., Dai L. *et al.* **Electrophoresis Coating of Titanium Dioxide on Aligned Carbon Nanotubes for Controlled Syntheses of Photoelectronic Nanomaterials**. *Adv. Mater.* 2007; 19 (9): 1239-43.

[35] Li X., Liu Y., Fu L. *et al.* **Synthesis and Device Integration of Carbon Nanotube/Silica Core−Shell Nanowires**. *J. Phys. Chem. C*. 2007; 111 (21): 7661-5.

[36] Modi A., Koratkar N., Lass E. *et al.* **Miniaturized gas ionization sensors using carbon nanotubes**. *Nature*. 2003; 424 (6945): 171-4.

[37] Penza M., Rossi R., Alvisi M., Serra E. **Metal-modified and vertically aligned carbon nanotube sensors array for landfill gas monitoring applications**. *Nanotechnology*. 2010; 21 (10): 105501.

[38] Randeniya L. K., Martin P. J., Bendavid A. **Detection of hydrogen using multi-walled carbon-nanotube yarns coated with nanocrystalline Pd and Pd/Pt layered structures**. *Carbon*. 2012; 50 (5): 1786-92.

[39] Sippel-Oakley J., et al. **Carbon nanotube films for room temperature hydrogen sensing**. *Nanotechnology*. 2005; 16 (10): 2218.

[40] Zilli D., Bonelli P. R., Cukierman A. L. **Room temperature hydrogen gas sensor nanocomposite based on Pd-decorated multi-walled carbon nanotubes thin films**. *Sensors and Actuators B: Chemical*. 2011; 157 (1): 169-76.

[41] Muller K. H., Yajadda M. M. A. **Electron transport in discontinuous gold films and the effect of Coulomb blockade and percolation**. *J. Appl. Phys.* 2012; 111 (12): 123705-11.

[42] Volotskova O., Fagan J. A., Huh J. Y. *et al.* **Tailored distribution of single-wall carbon nanotubes from arc plasma synthesis using magnetic fields**. *ACS Nano*. 2010; 4 (9): 5187-92.

[43] Khavrus V. O., Vinzelberg H., Schumann J. *et al.* **On the potential of long carbon nanotube forest for sensing gases and vapors**. *Physica E: Low-dimensional Systems and Nanostructures*. 2011; 43 (6): 1199-207.

[44] Xu T., Zach M. P., Xiao Z. L. *et al.* **Self-assembled monolayer-enhanced hydrogen sensing with ultrathin palladium films**. *Appl. Phys. Lett.* 2005; 86 (20): 203104.

[45] Flanagan T. B., Park C.-N. **Hydrogen-induced rearrangements in Pd-rich alloys**. *Journal of Alloys and Compounds*. 1999; 293-295: 161-8.

[46] Gurlo A., Clarke D. R. **High-sensitivity hydrogen detection: hydrogen-induced swelling of multiple cracked palladium films on compliant substrates**. *Angewandte Chemie*. 2011; 50 (43): 10130-2.

4

Plasma Scribing, a Mask-less Patterning of Carbon Nanotube Array for Plasmonic Sensing

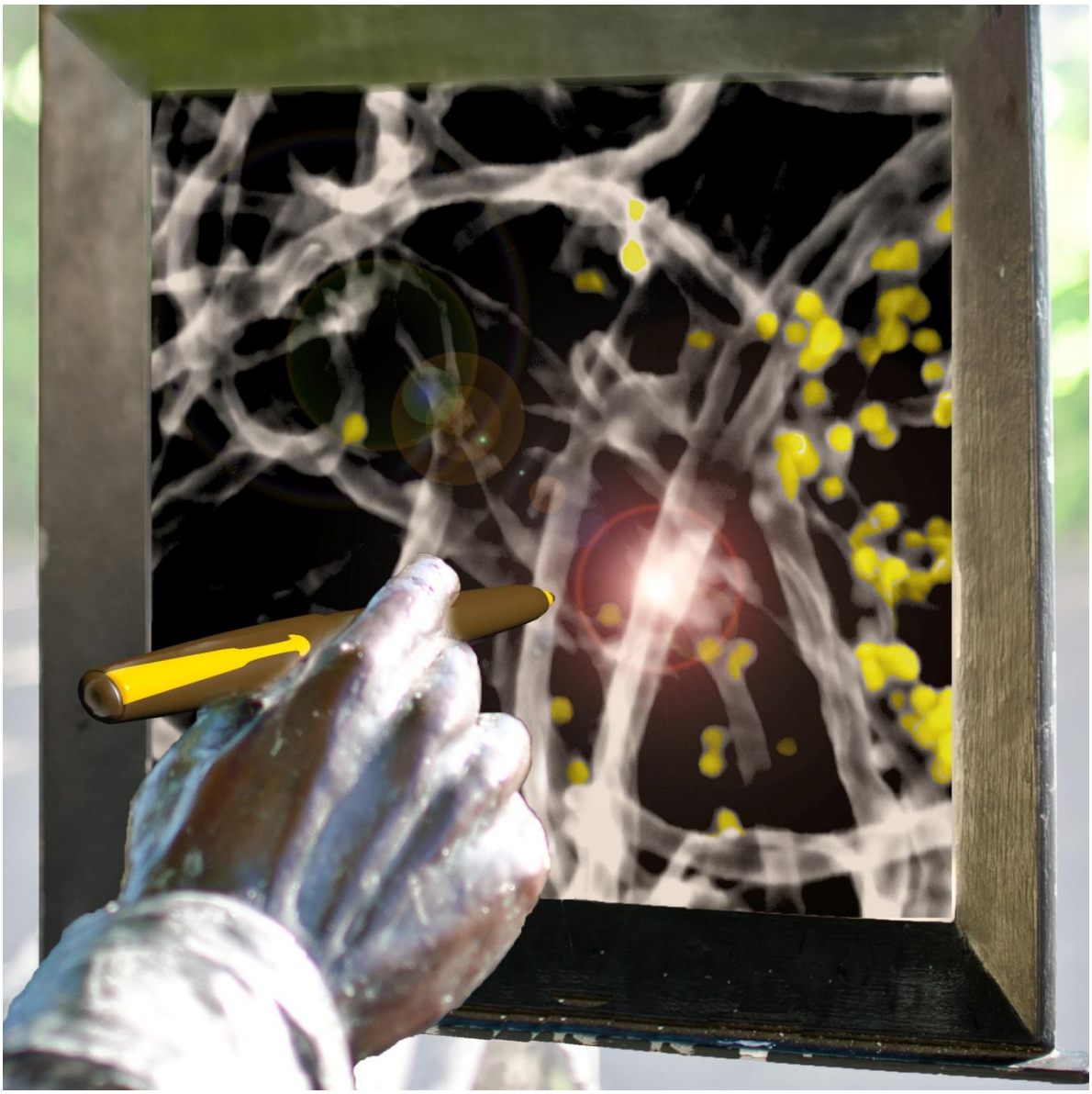

Cover image for Chemical Communication which accompanied the article "Atmospheric microplasma-functionalized 3D microfluidic strips within dense carbon nanotube arrays confine Au nanodots for SERS sensing" by Yick *et. al.*[1]

Chapter Summary

In the previous chapter, it was shown that vertically aligned CNT arrays possess many desirable properties desirable in a sensing platform. Yet, for a material to be useful in sensing application, it is often necessary to engineer specific interaction through induce chemical functionality. Currently, covalent modifications of CNT are dominated by chemical techniques that require the dispersion of CNT into a solvent which destroys the vertical alignment. In this chapter, atmospheric microplasma jet was used to demonstrate effective chemical functionalisation of CNT arrays while preserving their microstructure. Furthermore, the functionalisation was shown to be spatially confined; this allows the array to be chemically patterned without using a mask. The abrupt switch in hydrophobicitiy enables the confinement of colloidal Au nanoparticles into specific regions of the CNT arrays. The distribution of the Au nanoparticles was analysed using 4-aminothiophenol (4-ATP) as a Raman probe. This spatially defined hybrid nanostructure enabled surface-enhanced Raman scattering and thus represent a feasible platform for optical sensing of molecules. This chapter is based on the publication, "Atmospheric microplasma-functionalized 3D microfluidic strips within dense carbon nanotube arrays confine Au nanodots for SERS sensing" by Yick *et. al.*[1]

4.1 The Advantages of Vertical Alignment

In the previous chapter, the discussion centred on both controlling the physical coupling between CNTs and metal nanostructure and their utilisation as a resistive gas sensor. However, the coupling process was constrained by the line-of-sight requirement of magnetron sputtering. This prevented the metal from penetrate into the array. Thus, large portions of the CNT arrays remained unchanged. Here, a novel technique which enables spatially-defined chemical functionalisation of CNT arrays while preserving their microscopic structure (i.e. vertical alignment) will be discussed.

Prior to discussing how one might achieve chemical functionalisation of CNT arrays without affecting their microstructure, it is prudent to consider why it is advantageous to maintain the vertical alignment of the CNT arrays.

There are two general approaches in integrating CNTs into devices; they can be either constructed around individual tubes or with a network comprising a multitude of tubes. Though devices based around single-tubes can better utilise the intrinsic properties of CNT, they require labour intensive fabrication processes and their device performance (such as their sampling volume, signal strength or threshold) remains within the nanoscopic regime. These factors curtail the suitability of single-tube devices for many commercial applications.

On the other hand, CNTs can be employed as a collective such as an array or a network. In these structures, the global arrangement of the CNTs plays an additional role in determining the material's attributes. The microstructure in the CNT collective can usually be determined via two ways, post-synthesis or self-assembly during growth. In the former, the microstructure is created from as grown CNTs. Example of these includes, CNT yarns spun from CNT arrays or the formation of bucky paper from solution dispersed CNT.[2,3] Despite the ease of their production, post-synthesis assembled CNT structures exhibit physical properties below that of individual tubes.[4,5] This is because the microstructure often exhibits low degree of alignment which denies cooperative intertubular interactions. Alternatively, the microstructure of CNTs can be self-imposed during growth as discussed in Section 1.1.1 in Chapter 1. These are often arrays which can possess either horizontal or vertical alignment as determined by the experimental condition.[6,7] The fact that the microstructure is self-imposed simplifies the device fabrication as direct manipulation of individual tubes are unnecessary.[8]

Of the two structures, CNT arrays with vertical alignment are of specific interest to sensing applications due to their larger available surface area and packing density. This can be illustrated by

the comparing the surface area of a vertical array of CNTs with a planar surface of an equivalent area. The surface area of an individual CNT can be determined by the following:

$$Surface\ Area = (2\pi \times r\ \times h) + (2\pi \times r^2) \quad \text{- (4.1)}$$

Using the CNT arrays grown in Chapter 3 as examples, the height (h) of the CNT arrays was estimated to be 31.5 µm. From Figure 4.1, the radius (r) and density of the tubes can be seen as 7.2 nm and 17 tubes/µm respectively. Since, each CNT can yields an approximate surface area of 1.43×10^{-12} m^2. This results in a total surface area of 4.1×10^{-2} m^2 (assuming a 1 cm^2 wafer would possess 2.89×10^{10} tubes). In comparison, a planar silicon wafer of an equivalent dimension would only possess a surface area of 1×10^{-4} m^2. The larger available surface area allows for superior sensing performance in both sensitivity and response time.[9,10] This allows CNT arrays with vertical alignment to possess numerous advantages as-compared to randomly orientated or single CNT. Thus, they have been an attractive platform for developing new sensing devices.

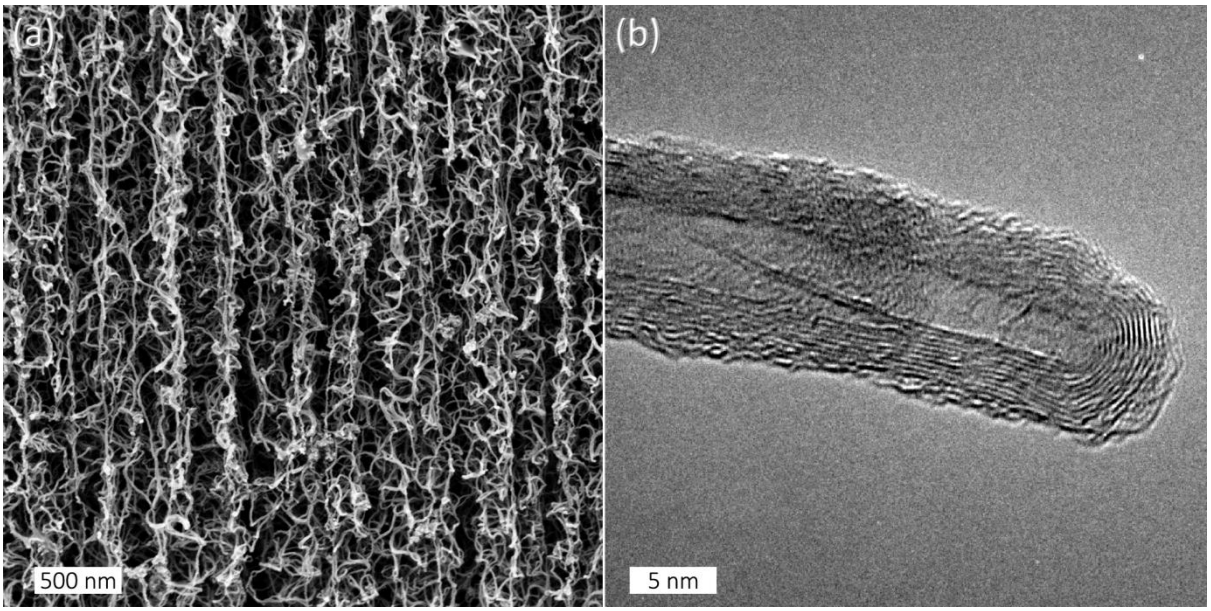

Figure 4.1 *A cross sectional scanning electron micrographs of the CNT arrays as discussed in Chapter 3 (a) and a transmission electron micrograph of an individual tube of the array.*

Aforementioned, the usefulness of pristine CNTs in sensing applications are limited. Apart from the resistive mechanism reported in the previous chapter, certain metal nanostructure such as Au and Ag nanoparticles can induce surface plasmons. These features allow surface-enhanced Raman scattering (SERS) which can aid chemical detection by enhancement the signal of up to 10^{11} times the original intensity.[11] The enhanced sensitivity makes SERS sensors useful for trace analysis and single molecule detection.[12] Therefore, SERS-based sensor can be fabricated by decorating CNTs with metal nanoparticles.[13,14] With the recent progress in the synthesis of CNT arrays at a macroscopic length.[15,16] The coupling of plasmonic capable metal nanoparticles onto CNT array are highly desirable in the hope that the intrinsic advantages of CNT arrays can be used to augment the performance of the plasmonic devices.

However, fabricating these hybrid structures is non-trivial due to the chemical inertness of the graphitic side walls.[17,18] The main challenge lies in the difficulty in enabling both effective functionalisation of CNTs while preserving the array's microstructure.[19] The commonly employed wet chemical techniques, which involve strong acids and sonication in aqueous solutions, often destroys the vertical alignment and can adversely affect the intrinsic properties of the tube.[20,21] An alternative method is to use plasma-based dry techniques, which functionalize the CNTs without the need of dispersion.[22-25] However, conventional plasma-based processes usually require low pressures for the plasma generation, which makes them expensive and time-consuming.[26,27] Moreover, prolonged exposure to energetic ions within the plasma may lead to the degradation of the CNTs and even the collapse of the arrays.[28,29] Therefore, there is a need to develop technique which can effectively functionalise the CNTs within the arrays while preserving their microstructure.

In this chapter, the above issue was resolved through the utilisation of a cold atmospheric-pressure microplasma jet (APMPJ) which enabled the effective functionalisation of CNTs while preserving the microstructure of the arrays. Contrary to the conventional low-pressure plasma systems, the APMPJ operates at room temperature and atmospheric pressure using very low power (mW–W range). The

surface treatment by APMPJ can be confined to areas as narrow as 100 µm (the size of the microplasma plume), which is of particular importance for the area-specific applications. In addition, a high density of reactive species (*e.g.*, radicals such as –OH, –O and –NH, atomic and excited molecules such as N_2, He and Ar, etc.) could be produced in the APMPJ, enabling more effective surface treatment.[30] Such features allowed spatially controllable decoration of CNT arrays with Au nanoparticles. The resulting Au/CNT hybrid nanostructure maintained the large surface area offered by the CNT arrays and a high loading of Au nanoparticles. This allowed the hybrid nanostructure to be exploited as an effective sensing platform based on the surface-enhanced Raman scattering (SERS) mechanism. This method resolves the limitation in utilising CNT arrays for chemical sensing devices and exhibits the ability to create chemically distinct patterns without using a mask.

4.2 Methodology

Growth of CNT arrays. The growth process used is identical to that which was described in chapter 3.2

Plasma modification of CNT arrays. To modify the CNT arrays, a home-made microplasma jet (APMPJ) was employed, which generated plasma using a 355 kHz radio-frequency (RF) power supply at 29 W (see the setup in Figure 4.2). The discharge occurred within a syringe where the anode and cathode were separated by 1 cm. Helium at atmospheric pressure was used as the working gas. The gap between the nozzle of the microplasma jet and the CNT array was 0.2 cm. The samples were scanned at a rate of 2 cm/min for 30 seconds to delineate the microfluidic strip. The nozzle of the syringe has a diameter of 1 mm.[31]

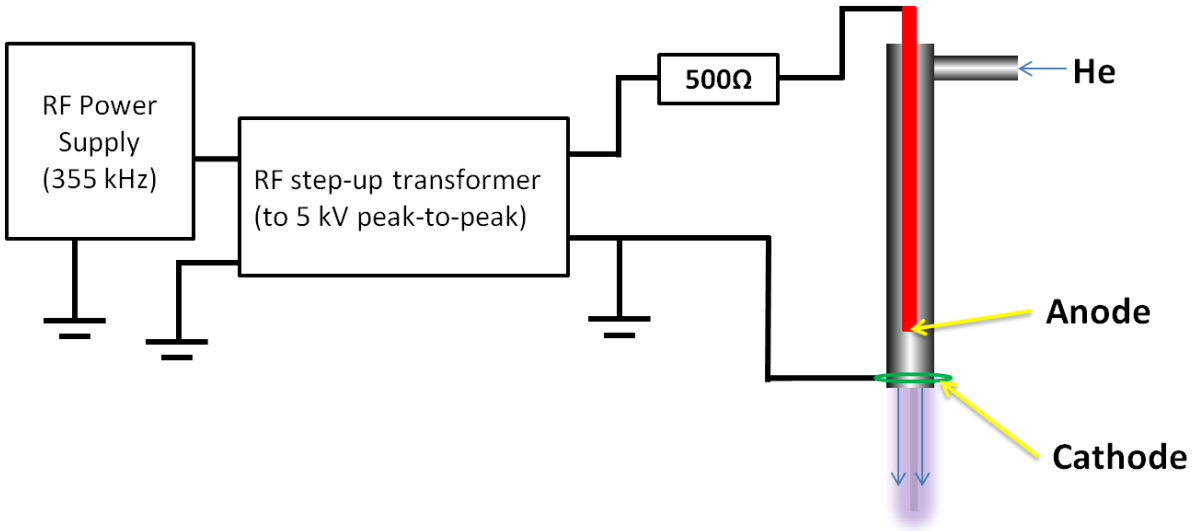

Figure 4.2 *Schematic of the cold APMPJ, the system consists of a low voltage 350 kHz radio-frequency (RF) power supply with an integrated matching circuit, a step-up transformer, and a current limiting resistor. The maximum output of the power supply system was 5 kV peak-to-peaks. The discharge occurred within a syringe where the anode and cathode was separated by 1 cm. Helium was used as the working gas for the discharge.*[1]

Coupling of CNT arrays with Au nanoparticles and attachment of 4-ATP. A 120-µL droplet of the aqueous solution containing colloidal Au nanoparticles stabilised by tannic acid (0.05 mg/mL with a size distribution of 13-15 nm; purchased from PlasmaChem GmbH) was placed onto the plasma-modified CNT arrays and left to dry overnight. 4-aminothiophenol solution (4-ATP; Sigma-Aldrich) was prepared by dissolving the substance into ethanol at a concentration of 10 mM. The Au nanoparticle decorated CNT arrays were then totally immersed in the 4-ATP solution for four days. Finally, the samples were washed in deionized water and dried overnight before Raman characterisation.

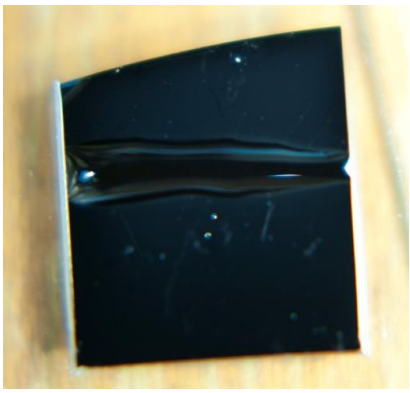

Figure 4.3 *Shown above is an example of the aqueous solution containing Au nanoparticles dropped onto the microfluidic strip. As can be seen, the solution remained confine within the plasma-generated microfluidic strip.*[1]

Characterisation methods. The microstructure of CNT arrays were investigated by a field-emission scanning electron microscopy (FE-SEM; Zeiss Auriga) operated at an acceleration voltage of 20 kV and a working distance of 4.5 mm. The optical micrograph was obtained by the Olympus BH2 microscope with a 100x objective lens. X-ray photoelectron spectroscopy (XPS) measurements were taken using the PHI Specs Sage 150 system, where the Mg Kα (at 1253.6 eV) line was used as the excitation source. The Raman spectra were collected by Renishaw *InVia* confocal Raman microscope system with a 50× objective lens. Samples were excited with 633 nm laser at power of ~ 1.5 mW and a spot diameter of ~ 1 μm^2.

4.3 Results and Discussion

Figure 4.4a shows the schematic diagram of experimental procedure. The APMPJ (Figure 4.4b) was then used to delineate a line pattern on the surface of the CNT array. After the short exposure (10–30 sec; in contrast to >10 min typical for low-pressure plasma treatments), a drastic change in surface wettability between the pristine and the plasma-modified areas was observed (Figure 4.4 c). The pristine areas (unexposed to the plasma) remained hydrophobic with a measured contact angle of 154.1°; whereas the plasma-modified area became hydrophilic (contact angle < 5°). This drastic and localized change created a microfluidic strip on the CNT array, allowing the confinement of the Au nanoparticle containing aqueous solution.

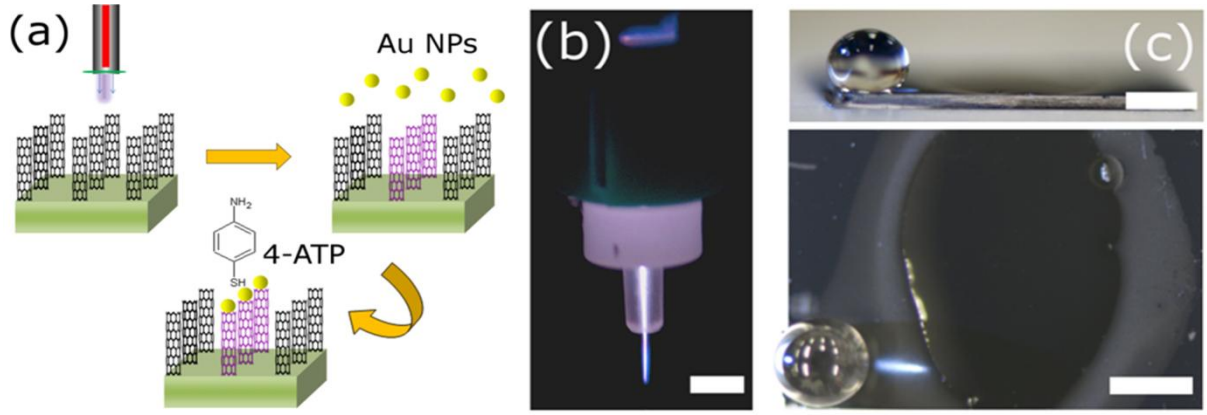

Figure 4.4 *(a) Schematic of the experimental procedure, the treated region is highlighted in pink. (b) A photograph showing the plasma plume's size (c) Change in surface wettability of the CNT arrays in the plasma-modified (hydrophilic) and the pristine area (hydrophobic). Scale bars are 2 mm in (b)-(c).*[1]

The observed change in surface wettability is caused by an alternation to the surface chemistry of the CNT array. Such changes were analysed through XPS and Raman. The XPS spectra suggested that the plasma treatment incorporated oxygen species into the structure (Figure 4.5a). The C *1s* and O *1s* core level spectra were shown in Figure 4.5 b and c respectively. In Figure 4.5b, four peaks at binding energies of 284.5, 285.8, 286.9 and 288.4 eV were observed in the C *1s* spectrum. These correspond to the carbon atoms in sp^2, sp^3, C-O and O-C=O bonding configurations, respectively.[32] This indicated that the plasma treatment, allowed the conjugated carbon structure to be opened up (changing from sp^2 to sp^3 hybridization) and the attachment of oxygen-containing moieties to the graphitic surface of CNTs. The presences of these of chemical functionalities were further corroborated by the O *1s* spectrum (Figure 4.5c), where two peaks at 532.4 and 533.6 eV corresponding to oxygen atoms in carboxylic and hydroxyl moieties were observed.[33,34] These results are in a good agreement with published reports on chemically functionalised CNTs and thus indicated that the APMPJ generated reactive sites within the graphitic network which enabled functional groups to be attached.[35]

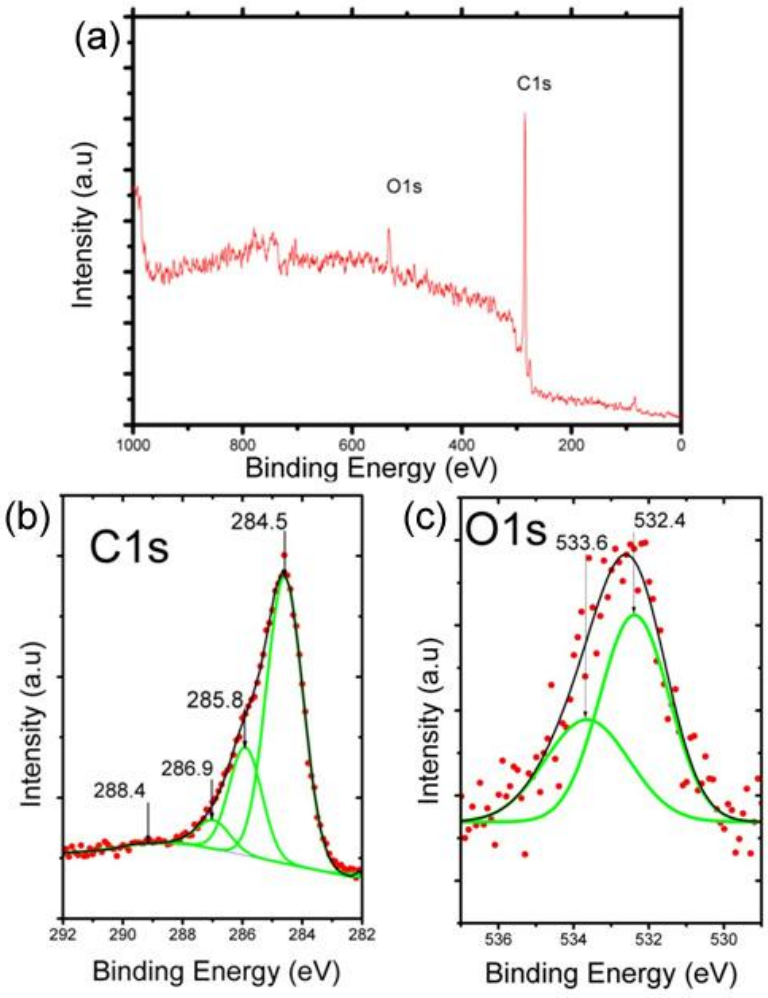

Figure 4.5 *XPS spectra of (a) survey, (b) C 1s and (c) O 1s of the APMPJ-treated CNT arrays.*[1]

Despite the drastic change in wettability and the emergence of new surface features, the APMPJ treatment did not significantly degrade the internal structure of the CNTs. This was demonstrated *via* Raman spectroscopic measurements of the CNTs (Figure 4.6). The spectra exhibited two prominent peaks in the Raman spectra, the D-peak at ~1325 cm^{-1} and the G-peak at ~1600 cm^{-1}, which stemmed from the defects and ordered graphitic structures, respectively.[36] The peak intensity and full-width-at-half-maximum (FWHM) of the G-peak feature remained almost unchanged. This led us to speculate that while the APMPJ treatment opened the outer wall(s) to chemical modification (as observed the increased peak intensity of the D-peak), it did not affect the inner walls, thereby preserving the structural integrity and transport properties of the nanotubes.[37] The result is consistent with the fact that the APMPJ treatment is essentially a mild and gentle process at a low operating temperature, which limits the modification to the outermost wall(s).[31]

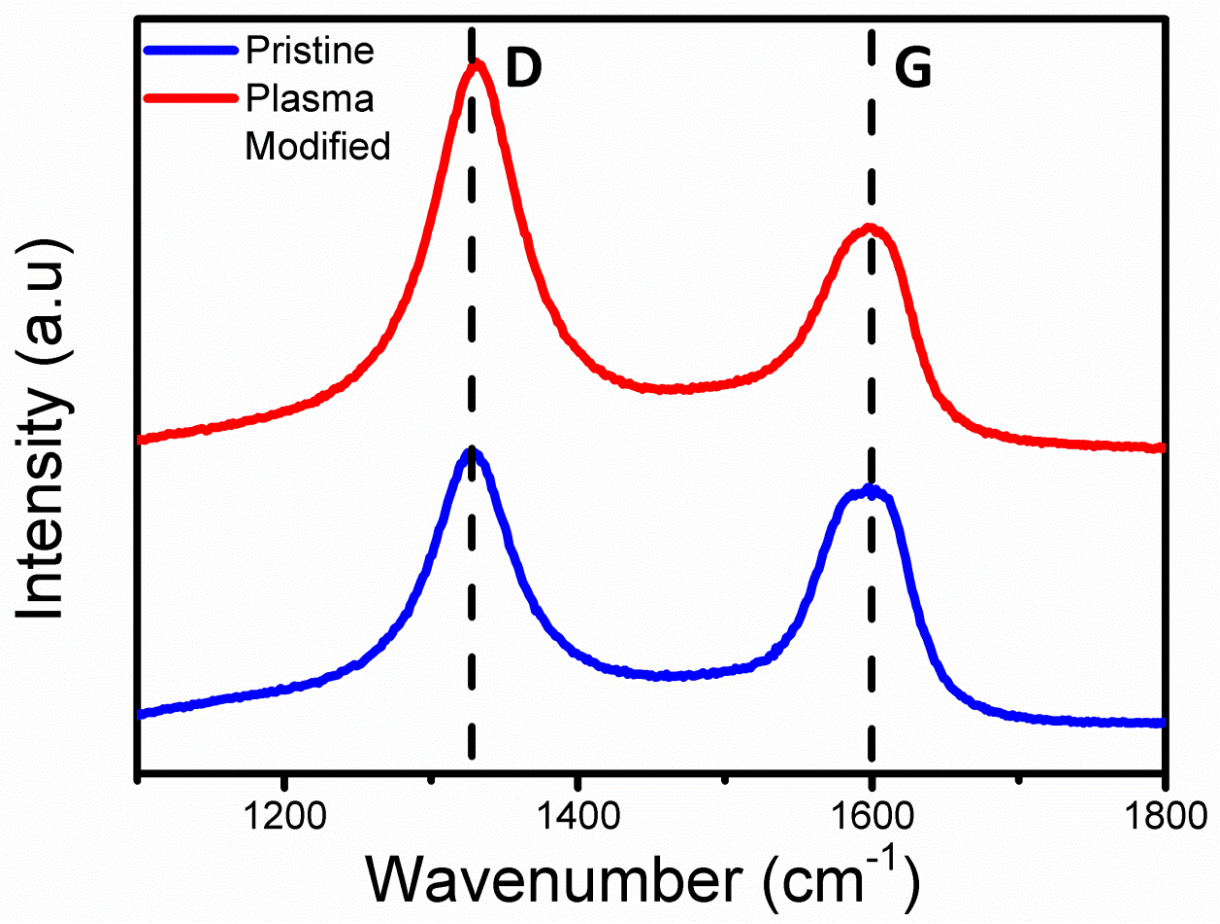

Figure 4.6 *Raman spectra of the pristine and plasma treated CNT arrays.*[1]

After the microplasma treatment, the Au nanoparticle containing solution was dropped onto the surface of the CNT arrays. The as-dropped solution was confined along the length of the plasma-generated microfluidic strip (Figure 4.3). Upon drying, two distinctive regions at the interface of the pristine and plasma-modified areas were observed under the optical microscope (Figure 4.8a). The SEM images revealed further details of Au/CNT hybrid structure: across the interface between the pristine (hydrophobic) and the plasma-modified (hydrophilic) areas, a drastic change in the density of Au nanoparticles was detected (Figure 4.7b). Indeed, Au nanoparticles were absent in the pristine region (Figure 4.7c); while as a high density of Au nanoparticles was confined within the modified region, as shown in Figure 4.7d. It is worth mentioning that no changes in the vertical alignment could be discerned even at the topmost layer of the arrays. This is in stark contrast to low-pressure plasma etching/treatments, where the structural integrity of CNT arrays was often inevitably damaged due to the strong ion bombardment.[38-40] The solvent- and mask-free patterning is also superior to many other patterning techniques such as laser pruning or lithography, where the former may damage the nanotube structure and the latter requires photo-sensitive masks which may introduce unwanted contamination.

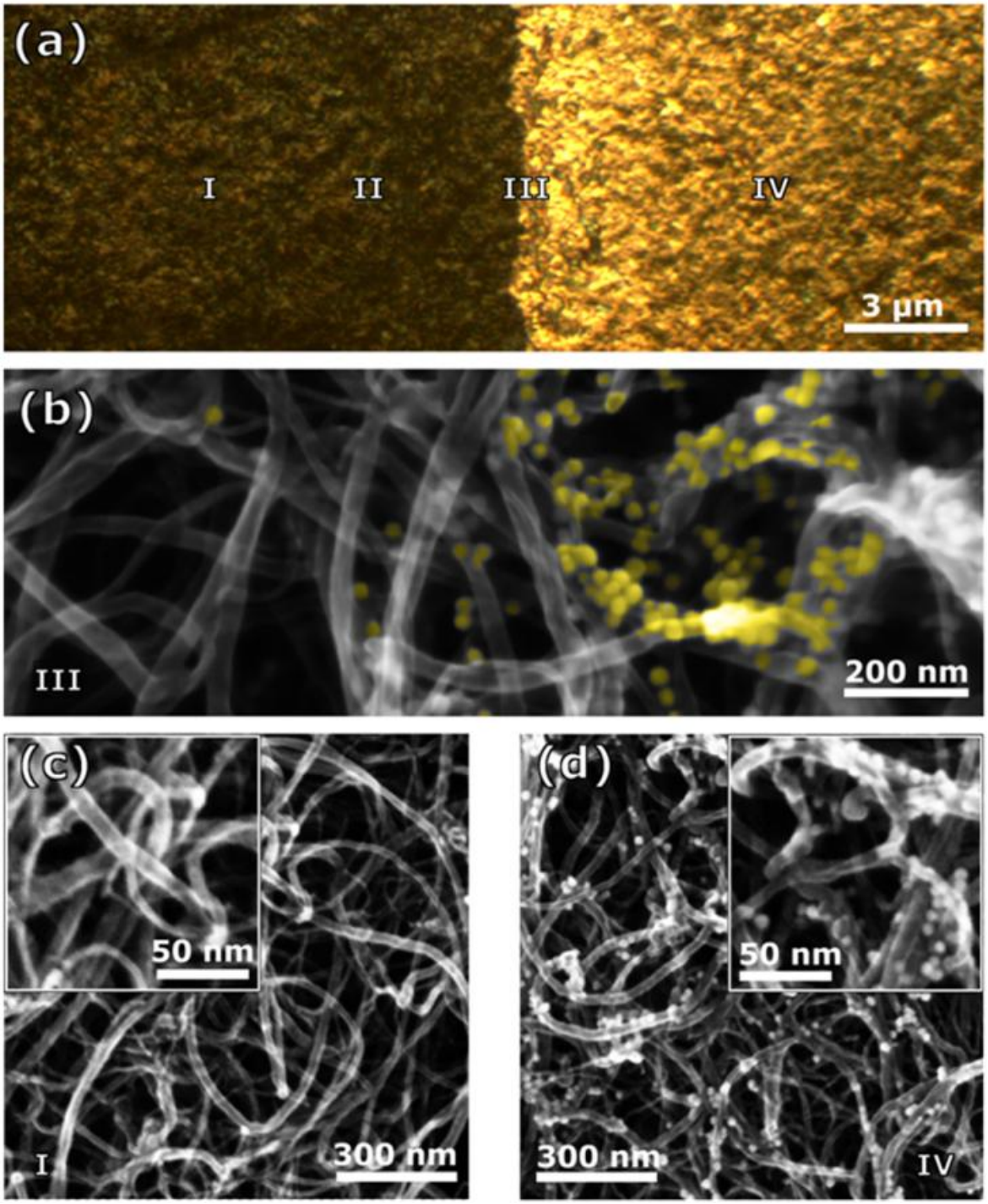

Figure 4.7 *(a) Optical micrograph of the Au/CNT hybrid at the interfacial region between the pristine and plasma modified. (b) SEM image depicting the interfacial region (III). False colour was applied to highlight the Au NDs. SEM micrographs of the pristine (c) and the Au ND-decorated (d) sides of the VA-CNTs, corresponding to areas (I) and (IV) in (a), respectively. Insets in (c) and (d) are the corresponding high-resolution SEM images.*[1]

It was further noted that the APMPJ could very effectively penetrate the thick and dense CNT arrays and modify the entire tube length. From the cross-sectional SEM images (Figure 4.8), after drying the

solution, the Au nanoparticles were confined to the topmost surface of the pristine CNT arrays. After the APMPJ treatment, however, evenly-distributed Au nanoparticles were found throughout the entire depth (2.5 µm) of the microfluidic strip (*i.e.*, forming a 3D Au/CNT hybrid over the entire nanotube length). The delivery of pre-fabricated nanoparticles *via* an aqueous solution further enabled a better control over the size distribution of the particles (diameter of 13–15 nm) as compared to other techniques. Additionally, all the micrographs indicated that these Au nanoparticles did not agglomerate and remained clearly separated from each other. This is particularly important for the effective operation of SERS-based sensors.[41]

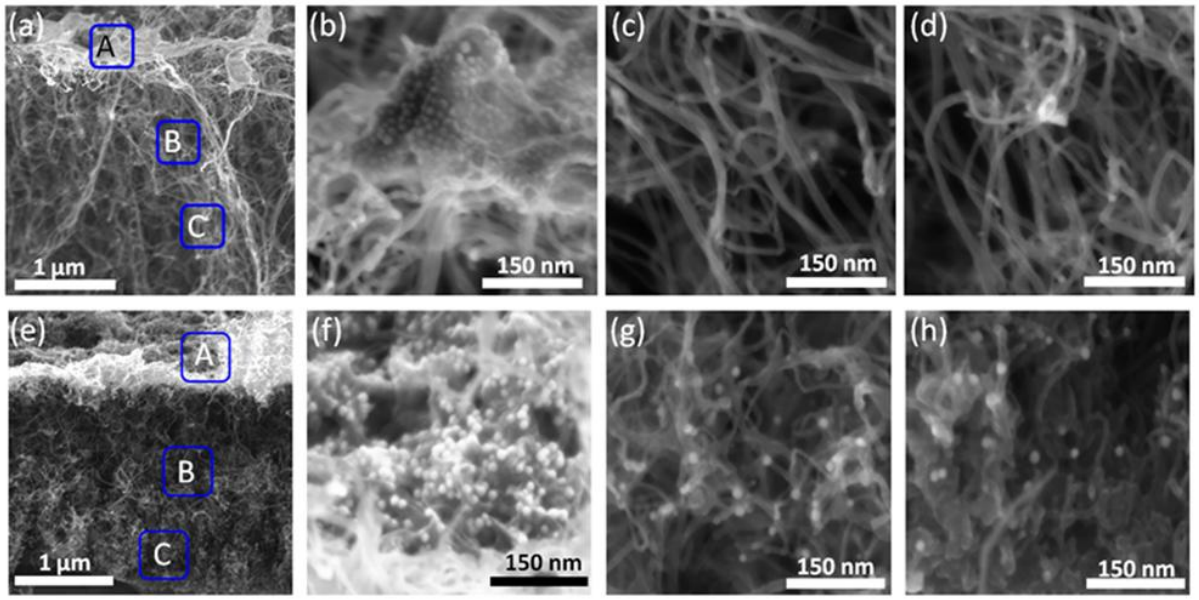

Figure 4.8 *(a) Cross-sectional SEM images of Au NDs deposited on the pristine CNT arrays. (b-d) High-resolution SEM images taken from squaress A-C in (a), respectively. (e) Cross-sectional SEM images of Au NDs deposited on the APMPJ-treated CNT arrays. (f-h) High-resolution SEM images taken from squares A-C in (e), respectively.*[1]

Next, the applicability of the Au/CNT hybrid for area-selective sensing was demonstrated through their response to the attachment of 4-aminothiophenol (4-ATP) probe molecules. This attachment was evidenced by the variation of the stretching (ν) and bending (δ) modes of 4-ATP measured by Raman spectroscopy. Figure 4.9 presents the micro-Raman spectra of the hybrid structure when the sampling area was moved over a length of 8 µm, from the pristine to the decorated areas. In the absence of APMPJ treatment, the main features of the Raman spectrum were at 1329.3 cm^{-1} and

1602.8 cm^{-1} (see Spectrum I in Figure 4.9), corresponding to the D- and G- peaks of the CNTs, respectively. As the sampling area was shifted towards the modified region, new peaks emerged in the Raman spectrum (see dotted circles in Spectrum II). At the interface and inside the plasma-modified area, these peaks became much stronger than the original CNT peaks (see Spectra III and IV). These new features encircled in Figure 4.9 were attributed to 4-ATP molecules including: v_{CS}, $7a(a_1)$ ~ 1076 cm^{-1}; δ_{CH}, $9b(b_2)$ ~1141 cm^{-1}; δ_{CH}, $9a(a_1)$ ~1182 cm^{-1}; $\delta_{CH} + v_{CC}$, $3(b_2)$ ~1389 cm^{-1}; $v_{CC} + \delta_{CH}$, $19b(b_2)$ ~1434 cm^{-1}; and v_{CC}, $8b(b_2)$ ~1574 cm^{-1} modes.[42] From the spectra II and III in Figure 4.9, a 10-15 times greater response to 4-ATPs was observed within the Au ND-decorated region compared to the undecorated region. This demonstrates the ability of the APMPJ to produce hybrid 3D nano-structures with localized and well-resolvable SERS responses. Optimization of the array morphology and nanoparticle density can be used to further enhance the SERS sensing response.

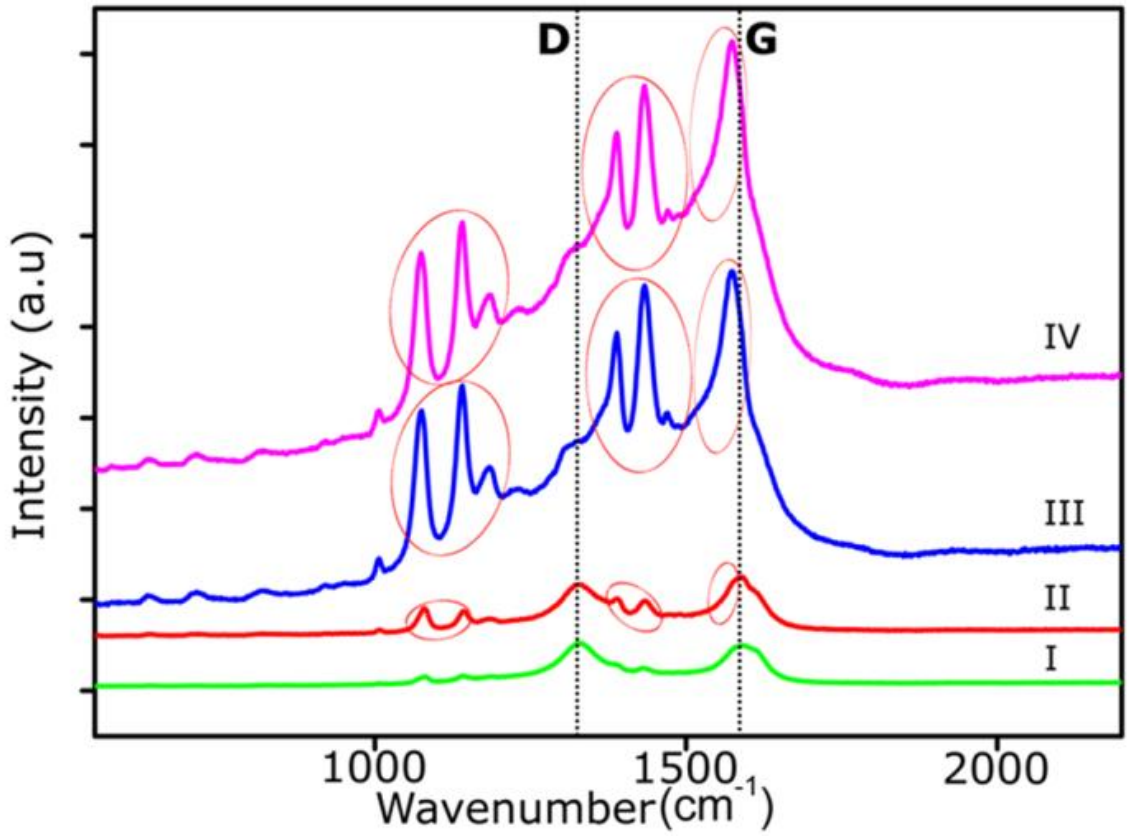

Figure 4.9 *Raman spectra from the different regions of the Au/CNT hybrid structure after the attachment of 4-ATP molecules to the Au nanoparticles. Spectra I-IV correspond to the areas labelled in figure 4.7a. The dotted lines denote the positions of the D- and G-band from the pristine CNTs, whereas the dotted circles denote the main Raman fingerprints of 4-ATP molecules.*[1]

The APMPJ treatment also improved the charge transfer between the Au nanoparticles and the 4-ATP probe molecules. By comparing the features at 1076 cm^{-1} ($7a(a_1)$) and 1141 cm^{-1} ($9b(b_2)$) between spectra II and III of Figure 4.9, the latter peak showed a stronger enhancement after the plasma modification. The preferential increase in the intensity of the b_2 mode correlated to the plasma-related improvement of the charge transfer between the decorated hybrid nanostructures and the attached 4-ATPs.[12,43] Apart from displaying clear Raman fingerprints, 4-ATP also serves as a mean for the formation of covalent links with other nanomaterials through their amine- and thiol-groups. In particular, the strong thiol-gold interaction allows the 4-ATP molecules to be anchored selectively onto the Au nanoparticles. These nanoparticles could then serve as preferential sites for the subsequent attachment and sensing of nanoparticles or biomolecules (*e.g.*, antibodies, antigens, etc.) onto the hybrid structures, merely within the plasma-modified strips.[44,45]

4.4 Chapter Conclusion

In summary, APMPJ was shown to an effective technique for chemical functionalization of CNT arrays. The treatment allowed the fabrication of a 3D sensing platform based on CNT arrays homogeneously decorated with Au nanoparticles over their entire depth. This technique did not require expensive vacuum equipment and operates in open air and room temperature. It also overcame the major shortcomings of wet chemical and conventional low-pressure plasma techniques which normally destroy the microstructure of CNT arrays. The area-specific chemical modification formed a microfluidic strip with the width defined by the thin plasma plume (~ 100 µm). Such a strip allowed the selective wetting upon application of the Au nanoparticle-containing aqueous solution, where the Au nanoparticles can attach exclusively to the plasma-modified region. The high loading ratio of metal nanoparticles offered by the large surface area of the arrays, the tuneable coupling between the tubes and the decorated nanoparticles, and the excellent electron transport properties of the nanotubes are apparently responsible for the reliable SERS sensing ability of such hybrid structures. Thus, having resolve the problem which currently inhibits the employment

of CNT arrays, this method present an avenue to utilise CNT arrays for next-generation sensing, energy storage and catalytic devices based on 3D hybrid nanostructures and microscopic area-selectively patterned chemical functionalities.

4.5 References

[1] Yick S., Han Z. J., Ostrikov K. **Atmospheric microplasma-functionalized 3D microfluidic strips within dense carbon nanotube arrays confine Au nanodots for SERS sensing**. *Chem. Commun.* 2013; 49 (28): 2861-3.

[2] Liu J., Rinzler A. G., Dai H. *et al.* **Fullerene Pipes**. *Science*. 1998; 280 (5367): 1253-6.

[3] Li Q. W., Zhang X. F., DePaula R. F. *et al.* **Sustained growth of ultralong carbon nanotube arrays for fiber spinning**. *Adv. Mater.* 2006; 18 (23): 3160-3.

[4] Ghemes A., Minami Y., Muramatsu J. *et al.* **Fabrication and mechanical properties of carbon nanotube yarns spun from ultra-long multi-walled carbon nanotube arrays**. *Carbon*. 2012; 50 (12): 4579-87.

[5] Park S., Kim H. R., Kim J. *et al.* **Assembly of Strands of Multiwall Carbon Nanotubes and Gold Nanoparticles Using Alkanedithiols**. *Carbon*. 2011; 49 (2): 487-94.

[6] Yu Q., Qin G., Li H. *et al.* **Mechanism of Horizontally Aligned Growth of Single-Wall Carbon Nanotubes on R-Plane Sapphire**. *J. Phys. Chem. B*. 2006; 110 (45): 22676-80.

[7] Xie S. S., Chang B. H., Li W. Z. *et al.* **Synthesis and Characterization of Aligned Carbon Nanotube Arrays**. *Adv. Mater.* 1999; 11 (13): 1135.

[8] Wei C., Dai L., Roy A., Tolle T. B. **Multifunctional Chemical Vapor Sensors of Aligned Carbon Nanotube and Polymer Composites**. *J. Am. Chem. Soc.* 2006; 128 (5): 1412-3.

[9] Modi A., Koratkar N., Lass E. *et al.* **Miniaturized gas ionization sensors using carbon nanotubes**. *Nature*. 2003; 424 (6945): 171-4.

[10] Penza M., Rossi R., Alvisi M., Serra E. **Metal-modified and vertically aligned carbon nanotube sensors array for landfill gas monitoring applications**. *Nanotechnology*. 2010; 21 (10): 105501.

[11] Xu H., Aizpurua J., Käll M., Apell P. **Electromagnetic contributions to single-molecule sensitivity in surface-enhanced Raman scattering**. *Physical Review E*. 2000; 62 (3): 4318-24.

[12] Wang Y., Chen H., Dong S., Wang E. **Surface enhanced Raman scattering of *p*-aminothiophenol self-assembled monolayers in sandwich structure fabricated on glass**. *J. Chem. Phys.* 2006; 124: 074709.

[13] Sahoo S., Husale S., Karna S. *et al.* **Controlled Assembly of Ag Nanoparticles and Carbon Nanotube Hybrid Structures for Biosensing**. *J. Am. Chem. Soc.* 2011; 133 (11): 4005-9.

[14] Zhao L., Shingaya Y., Tomimoto H. *et al.* **Functionalized carbon nanotubes for pH sensors based on SERS**. *J. Mater. Chem.* 2008; 18 (40): 4759-61.

[15] Hata K., Futaba D. N., Mizuno K. *et al.* **Water-Assisted Highly Efficient Synthesis of Impurity-Free Single-Walled Carbon Nanotubes**. *Science*. 2004; 306: 1362.

[16] Han Z. J., Ostrikov K. **Uniform, Dense Arrays of Vertically Aligned, Large-Diameter Single-Walled Carbon Nanotubes**. *J. Am. Chem. Soc.* 2012; 134: 6018.

[17] V. Palermo, P. Samorì. **Molecular Self-Assembly across Multiple Length Scales**. *Angew. Chem. Int. Ed.* 2007; 46 (24): 4428-32.

[18] Han Z. J., Tay B. K., Tan C. M. *et al.* **Electrowetting Control of Cassie-to-Wenzel Transitions in Superhydrophobic Carbon Nanotube-Based Nanocomposites**. *ACS Nano*. 2009; 3: 3031.

[19] Palermo V., Samori P. **Molecular Self-Assembly across Multiple Length Scales**. *Angew. Chem. Int. Ed.* 2007; 46: 4428.

[20] K. Balasubramanian, M. Burghard. **Chemically Functionalized Carbon Nanotubes**. *Small*. 2005; 1 (2): 180-92.

[21] M. S. Marshall, S. Popa-Nita, J. G. Shapter. **Measurement of functionalised carbon nanotube carboxylic acid groups using a simple chemical process**. *Carbon*. 2006; 44 (7): 1137-41.

[22] H. Kinoshita, A. Ogasahara, Y. Fukuda, N. Ohmae. **Superhydrophobic/superhydrophilic micropatterning on a carbon nanotube film using a laser plasma-type hyperthermal atom beam facility**. *Carbon*. 2010; 48 (15): 4403-8.

[23] D. Kolacyak, J. Ihde, C. Merten *et al.* **Fast functionalization of multi-walled carbon nanotubes by an atmospheric pressure plasma jet**. *J. Colloid. Interface. Sci.* 2011; 359 (1): 311-7.

[24] L. K. Randeniya, P. J. Martin, A. Bendavid, J. McDonnell. **Ammonia sensing characteristics of carbon-nanotube yarns decorated with nanocrystalline gold**. *Carbon*. 2011; 49 (15): 5265-70.

[25] M. V. Naseh, A. A Khodadadi, Y. Mortazavi *et al.* **Fast and clean functionalization of carbon nanotubes by dielectric barrier discharge plasma in air compared to acid treatment**. *Carbon*. 2010; 48 (5): 1369-79.

[26] W. H. Chiang, M. Cochey, R. C. Virnelson, R. M. Sankaran. **Nonlithographic fabrication of surface-enhanced Raman scattering substrates using a rastered atmospheric-pressure microplasma source**. *Appl. Phys. Lett.* 2007; 91 (2): 021501-3.

[27] A. Schutze, J. Y. Jeong, S. E. Babayan *et al.* **The atmospheric-pressure plasma jet: A review and comparison to other plasma sources**. *IEEE Transactions on Plasma Science*. 1998; 26 (6): 1685-94.

[28] K. S. Hazra, N. A. Koratkar, D. S. Misra. **Improved field emission from multiwall carbon nanotubes with nano-size defects produced by ultra-low energy ion bombardment**. *Carbon*. 2011; 49 (14): 4760-6.

[29] C. Bittencourt, C. Navio, A. Nicolay *et al.* **Atomic Oxygen Functionalization of Vertically Aligned Carbon Nanotubes**. *Journal of Physical Chemistry C*. 2011; 115 (42): 20412-8.

[30] Lu X. P., Laroussi M. **Electron density and temperature measurement of an atmospheric pressure plasma by millimeter wave interferometer**. *Appl. Phys. Lett.* 2008; 92: 051501.

[31] Yan W., Han Z. J., Phung B. T., Ostrikov K. **Silica Nanoparticles Treated by Cold Atmospheric-Pressure Plasmas Improve the Dielectric Performance of Organic–Inorganic Nanocomposites**. *ACS Appl. Mater. Interfaces*. 2012; 4: 2637.

[32] Ago H., Kugler T., Cacialli F. *et al.* **Work functions and surface functional groups of multiwall carbon nanotubes**. *Journal of Physical Chemistry B*. 1999; 103 (38): 8116-21.

[33] V. Datsyuk, M. Kalyva, K. Papagelis *et al.* **Chemical oxidation of multiwalled carbon nanotubes**. *Carbon*. 2008; 46 (6): 833-40.

[34] Datsyuk V., Kalyva M., Papagelis K. *et al.* **Chemical oxidation of multiwalled carbon nanotubes**. *Carbon*. 2008; 46: 833.

[35] Kolacyak D., Ihde J., Merten C. *et al.* **Fast functionalization of multi-walled carbon nanotubes by an atmospheric pressure plasma jet**. *J. Colloid Interface Sci.* 2011; 359: 311.

[36] Dresselhaus M. S., Dresselhaus G., Saito R., Jorio A. **Raman spectroscopy of carbon nanotubes**. *Phys. Rep.* 2005; 409: 47.

[37] Gupta S., Patel R. J. **Changes in the vibrational modes of carbon nanotubes induced by electron-beam irradiation: resonance Raman spectroscopy**. *J. Raman Spectrosc.* 2007; 38: 188.

[38] Li P., Lim X., Zhu Y. *et al.* **Tailoring Wettability Change on Aligned and Patterned Carbon Nanotube Films for Selective Assembly**. *J. Phys. Chem. B*. 2007; 111: 1672.

[39] Zhao B., Zhang L., Wang X., Yang J. **Surface functionalization of vertically-aligned carbon nanotube forests by radio-frequency Ar/O_2 plasma**. *Carbon*. 2012; 50: 2710.

[40] Hazra K. S., Koratkar N. A., Misra D. S. **Improved field emission from multiwall carbon nanotubes with nano-size defects produced by ultra-low energy ion bombardment**. *Carbon*. 2011; 49: 4760.

[41] Yeshchenko O. A., Dmitruk I. M., Alexeenko A. A. *et al.* **Size-dependent surface-plasmon-enhanced photoluminescence from silver nanoparticles embedded in silica**. *Phys. Rev. B*. 2009; 79: 235438.

[42] Rider A. E., Kumar S., Furman S. A., Ostrikov K. **Self-organized Au nanoarrays on vertical graphenes: an advanced three-dimensional sensing platform**. *Chem. Commun.* 2012; 48: 2659.

[43] Osawa M., Matsud N., Yoshii K., Uchida I. **Charge Transfer Resonance Raman Process in Surface-Enhanced Raman Scattering from *p*-Aminothiophenol Adsorbed on Silver: Herzberg-Teller Contribution**. *J. Phys. Chem.* 1994; 98: 12702.

[44] Li G.-j., Liu L.-h., Qi X.-w. *et al.* **Development of a sensitive electrochemical DNA sensor by 4-aminothiophenol self-assembled on electrodeposited nanogold electrode coupled with Au nanoparticles labeled reporter ssDNA**. *Electrochim. Acta*. 2012; 63: 312.

[45] Vakarelski I. U., Brown S. C., Higashitani K., Moudgil B. M. **Penetration of Living Cell Membranes with Fortified Carbon Nanotube Tips**. *Langmuir*. 2007; 23: 10893.

Enhanced Supercapacitor Performance via the Fusion of Vertical Graphene Nanosheets and Carbon Nanotubes

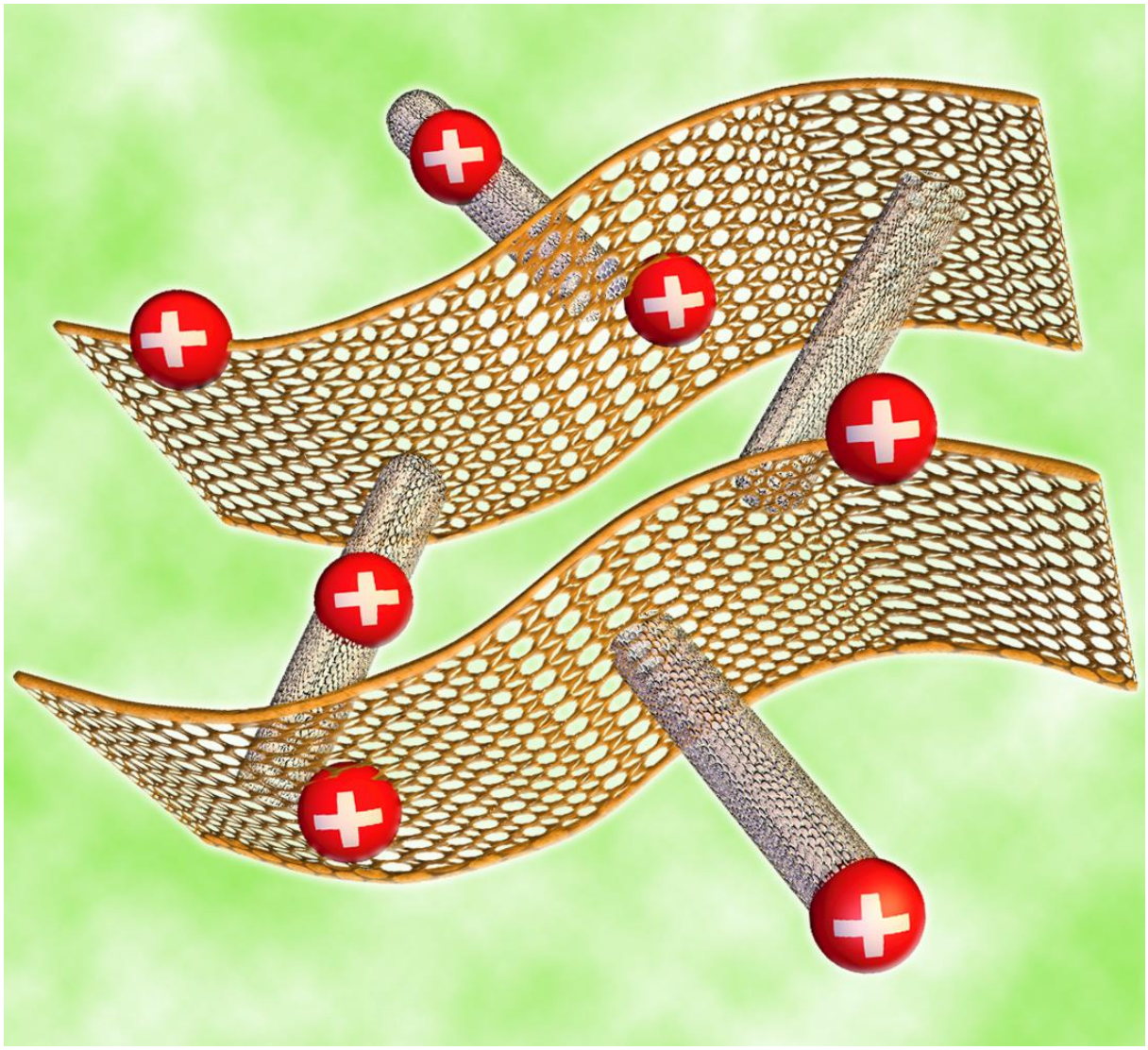

Schematic of the supercapacitor electrode made from VGNS/CNT hybrid nanostructure. This illustration was adapted from the publication "*Synergistic Fusion of Vertical Graphene Nanosheets and Carbon Nanotubes for High Performance Supercapacitor Electrodes"* which I was credited as an equal lead-author.[1]

Chapter Summary

This chapter outlines the growth and utilization of a graphene/CNT hybrid nanostructure for energy storage purposes. CNTs and graphene are seen as two of the most attractive electrode materials for supercapacitors due to their large surface area, high electrical conductivity and electrochemical stability. Despite these advantages, both materials possess inherent flaws which are detrimental for energy storage performance. For instance, CNTs are hindered by their substrate-limited growth and the problem of tube bundling in liquid electrolyte whereas graphene suffer from under-utilized basal planes and intersheet stacking. Thus, their implementations in devices are hindered, as their performances fall short of what is theoretically expected. In this chapter I will explore the possibility of fusing CNTs and Vertical Graphene Nanosheets (VGNS) via a direct growth approach. The combination of two sp^2 carbon structures with different morphology overcomes the challenges intrinsic to both materials. The resulting VGNS/CNTs hybrid nanostructures utilise non-Faradaic charge storage mechanism and show a specific capacitance of 278 F g^{-1} at 10 mV s^{-1} which is superior to the values normally obtained from either CNTs or graphene alone. Furthermore, the high stability of the hybrid nanostructures was demonstrated by a capacitance retention of >99% after 8,000 charge/discharge cycles at 100 mV s^{-1}. This work resulted in a joint publication between the author and Mr Dong Han Seo in ChemSusChem, titled "*Synergistic Fusion of Vertical Graphene Nanosheets and Carbon Nanotubes for High Performance Supercapacitor Electrodes*".[1]

5.1 Why Carbon-Based Supercapacitors?

The progress of our society is intertwined with technological developments. Though the advancement in technology has led to devices which are smarter, more capable and more effective, it has also significantly increased their energy demands. Currently, the lack of high-performance energy storage medium has hampered the deployment of next generation portable devices.[2-4] In this aspect, supercapacitor which possesses high power density, rapid charge/discharge rate, and long lifespan is a particularly attractive option.[5,6] The basic operating principle of supercapacitors

involves two electrodes with large surface areas to store charges in the electrical double-layer (EDL) and/or through the electrochemical redox reactions (*i.e.*, pseudocapacitance).[6,7] For a material to be an effective supercapacitor electrode, a high specific capacitance, low internal resistance and good stability are desirable. Among a variety of electrode materials, carbon-based nanostructures such as graphene and CNTs have attracted considerable interest because of their excellent electrochemical performance, easy processability, and tailorable structural properties.[8-10]

Recently, VGNS which is a derivative of graphene has emerged as a promising electrode material for binder-free, high-performing supercapacitors.[11] VGNS show excellent charge storage features such as a large surface area, high specific capacitance, stable charge retention capability, and low relaxation time constant τ_0.[11,12] In addition to many intrinsic attributes of horizontal graphenes, VGNS also possesses an inherently open, interconnected, three-dimensional (3D) morphology due to the vertical configuration of graphene sheets. Such morphology allows rapid ion transport within the material and enables the formation of a large number of thin reactive edge planes which are more electrochemically active than the basal graphitic planes.[11] Furthermore, the rigidity of VGNS could prevent the uncontrollable stacking of graphene nanosheets, a commonly observed problem in horizontal graphenes when immersed in liquid electrolytes.[13-15] These structural features enable VGNS to preserve the utilisable surface area for charge storage and retain their capacitance even after long charge/discharge cycles. Thus, in many cases VGNS can be a better practical choice over their conventional horizontal counterpart.

Despite these advantages, there are several roadblocks which impede the practical usage of VGNS as an active material in supercapacitors. Firstly, the open structure of VGNS results in gaps between the nanosheets which create barriers for electrical conduction and increase the resistance of the electrode. Secondly, though the edge planes exhibit a high electrochemical activity, the bulk of VGNS is comprised of basal planes which show only a fraction of the capacitance as compared to the edge planes.[11] Thirdly, although the nanocavities are desirable for ion accessibility and fast ion transport,

they also result in a low tapping density of the active material, which inevitably leads to a low areal and volumetric specific capacitance of the devices.

CNTs possess many attributes desirable in supercapacitor electrodes, such as large surface area, chemical stability and good mechanical properties.[16,17] The low internal resistance of CNTs allows a high-power density to be achieved and, if all the external surface area of a SWCNT is to be utilised, a theoretical specific capacitance of 280 F g^{-1} can be achieved.[18] However, CNT-based supercapacitor has yet reached their predicted performance. There are two major factors which impede the performance of CNT-based electrodes. Firstly, the available specific surface area of CNTs is often lower than that predicted. This is caused by the aggregation of CNTs into bundles, which limits ion accessibility, hence decreasing the usable area for the EDL formation.[19] Secondly, the integration of CNTs onto current collectors is difficult as the growth process is substrate-specific.[20,21] So far the specific capacitances of CNT electrodes reported in the literature range between 50-100 F g^{-1}.[22] As such, CNT electrodes have not made the expected impact into the field of supercapacitors.

Thus, the enhancement of carbon-based nanostructure through combination with other electrochemically active materials is necessary. The conventional approaches are to attach pseudocapacitive materials such as metal oxides and conductive polymers to improve the capacitance of carbon-based electrodes.[23-26] However, though the addition of these materials can deliver a high specific capacitance of the electrodes, they usually suffer from low electrical conductivity and poor stability.[27] Alternatively, the combination of CNTs with VGNS can in principle increase the surface area for charge storage, generate extra conductive pathways which can lower the internal resistance, and enhance the tapping density of the electrode. Unfortunately, the common methods of fabricating the graphene/CNTs hybrids through solution-based mixing often results in the bundling of nanotubes due to the strong *van der Waals* interactions which can significantly reduce the amount of surface sites accessible to ions.[13,28-30] Recently, integration based on the direct growth of CNTs on horizontal graphenes has been demonstrated.[31-33] However,

graphenes in such a planar, two-dimensional (2D) configuration acted merely as the current collector and their excellent electrochemical properties were not utilized. These methods of integration also led to a reduction of surface area which inevitably compromised the performance of hybrid graphene/CNT nanostructures. Given these challenges, the development of an effective method which can complementarily integrate VGNS and CNTs on different current collectors with a low contact resistance is highly desirable.

In this chapter, the fusion of VGNS/CNTs into a hybrid nanostructure is achieved via a direct growth method and their subsequent supercapacitor performance is explored. The VGNS/CNTs hybrid electrode possesses a high specific capacitance of 278 F g^{-1} at 10 mV s^{-1} in a low-concentration aqueous electrolyte using the three-electrode cell measurement. Moreover, the stability of VGNS/CNT hybrid electrode is evidenced by the capacitance retention of >99% after 8,000 charge/discharge cycles. The integration of VGNS and CNTs thus leads to significant improvements in various aspects vital to high performance supercapacitors and other energy storage devices.

5.2 Methodology

Growth of VGNS. A thin layer of commercially available butter was spread over the flexible graphite paper substrate. It was then loaded into radio-frequency inductively-coupled plasma (ICP) chemical vapor deposition (CVD) chamber and placed directly under the plasma generation site. During the growth, a gas mixture of Ar and H_2 was fed into the chamber at a constant pressure of 2.5 Pa and the plasma was ignited at 1 kW. Despite the lack of external heating, the substrate temperature reached 400 – 450 °C due to the direct plasma-heating effect.[34] The VGNS structures were subsequently obtained by exposing commercial butter to the plasma for 9 min. No metal catalyst was used in the process, thereby simplifying the production and reducing the possible contamination of the electrodes. The mass loading of VGNS was about 100 μg/cm^2.

Growth of CNT arrays. Catalyst consisting of 1 nm Co and 1 nm Mo was sputtered onto graphite paper. It was then inserted into a TCVD (same as the CVD system used in the previous chapters) and a gas mixture of Ar and H_2 at 262 and 100 sccm, respectively was fed into the system, while the furnace was heated at 30 °C per min to reach 750 °C. The growth of CNTs was initiated by the introduction of 100 sccm of C_2H_4. After 20 min, the growth was terminated and the furnace was cooled down to room temperature in a continuous flow of argon. The pressure was kept at one atmosphere throughout the heating and growth processes. The mass loading of CNTs after growth was ~200 μg/cm^2.

Growth of CNTs on VGNS. The direct growth of CNTs and VGNS was carried out in a thermal CVD system. Catalysts for growing CNTs were prepared by sequentially sputtering 1 nm thick Mo and 1 nm thick Co onto the pristine VGNS. The catalyst-loaded VGNS were then inserted into a quartz tube furnace and grown in the aforementioned procedure. This fabrication process of VGNS/CNTs hybrid structures can be easily scaled up with a high controllability and reproducibility. The optimum mass loading of VGNS/CNTs was about 130 μg/cm^2.

VGNS/CNT hybrid structure grown with thinner Co/Mo catalyst. Catalyst consisting of 0.5 nm Co and 0.5 nm Mo was sputtered onto the VGNS. The catalyst-loaded VGNS was then inserted into the tube furnace and the same conditions for growing CNTs were adopted. The mass loading after CNT growth was ~125 μg/cm^2.

VGNS/CNT hybrid structure grown with Fe catalyst. Catalyst consisting of 1 nm Fe was sputtered onto the VGNS. The catalyst-loaded VGNS was then inserted into the tube furnace and the same conditions for growing CNTs were adopted. The mass loading after CNT growth was ~175 μg/cm^2.

VGNS/CNT hybrid structure grown with water assistance. The same catalyst and growth conditions as in the optimum VGNS/CNTs hybrid structure were adopted, except that water vapor carried by 20

sccm Ar were simultaneously introduced and terminated with the C_2H_4 precursor. The mass loading after CNT growth was ~150 μg/cm^2.

Microscopy and microanalysis. Field-emission scanning electron microscopic (FE-SEM) images were obtained by Zeiss Auriga microscope operated at 5 keV electron beam energy with an InLens secondary electron detector. Transmission electron microscopy (TEM) was conducted by the JEOL 2100 operating at 200 kV. Raman spectroscopy was performed using a Renishaw *inVia* spectrometer with a laser excitation at 514 nm (Ar laser) and a probing spot size of ~1 μm^2. X-ray photoelectron spectroscopy (XPS) spectra were recorded by Specs SAGE 150 spectroscope with the Mg *Kα* excitation at 1253.6 eV. Both survey and narrow scans of C 1s and O 1s were conducted. The mass of the electrode were determined by weighting a 10 cm long sample on an ultrasensitive balance (Δ±0.1 μg; Mettler Toledo UMT2) and calculating the fractional mass which was submerged into the electrolyte.

Electrochemical measurements. The electrochemical measurements were performed in 0.1 M Na_2SO_4 aqueous electrolyte at room temperature. Both three-electrode and two-electrode cell configurations were employed. The three-electrode cell used the as-grown carbon-based sample as the working electrode, a Pt foil as the counter electrode, and an Ag/AgCl reference electrode; while the two-electrode cell used two identical testing samples as the electrodes separated by a thin layer of prolypropylene. Cyclic voltammetry (CV), galvanostatic charge/discharge, and electrochemical impedance spectroscopy (EIS) measurements were conducted using a BioLogic VSP 300 potentiostat/galvanostat device. CV tests were performed in the potential range of 0 – 0.8 V at scan rates of 10 – 500 mV s^{-1}. Galvanostatic charge/discharge curves were obtained at a constant current density of 2 – 8 A g^{-1}. EIS measurements were performed in the frequency range from 0.01 Hz to 100 kHz. The specific capacitance *C* was calculated from the CV curves by integrating the discharge current against the potential *V* according to $\mathrm{C_S} = (\int \mathrm{I\,dV/vm\Delta V})$ where v is the scan rate (V s^{-1}), *m* is the mass of the active material, and *ΔV* is the operating potential window (0.8 V).[35] It was worth

mentioning that in the calculations the capacitance contribution from pure graphite paper (i.e., 15 mF/cm^2 as measured at 10 mV/s in the three-electrode cell configuration) was subtracted from the overall capacitance of the electrodes (the VGNS/CNTs hybrid structure showed an overall capacitance of 51.3 mF/cm^2 at 10 mV/s in the three-electrode cell configuration).

5.3 Results and Discussion

5.3.1 Fabrication and Structure of the VGNS/CNTs Hybrid

Flexible and light-weight energy storage devices play a central role in the future development of multifunctional electronics such as portable and wearable devices, roll-up displays, and photovoltaic cells.[36] To this end, flexible graphite paper was chosen as the growth substrate for VGNS. Due to its good electrical conductivity, graphite paper also acts as the current collector in the supercapacitor electrode. Figure 5.1a illustrates the procedure in preparing our hybrid electrodes.

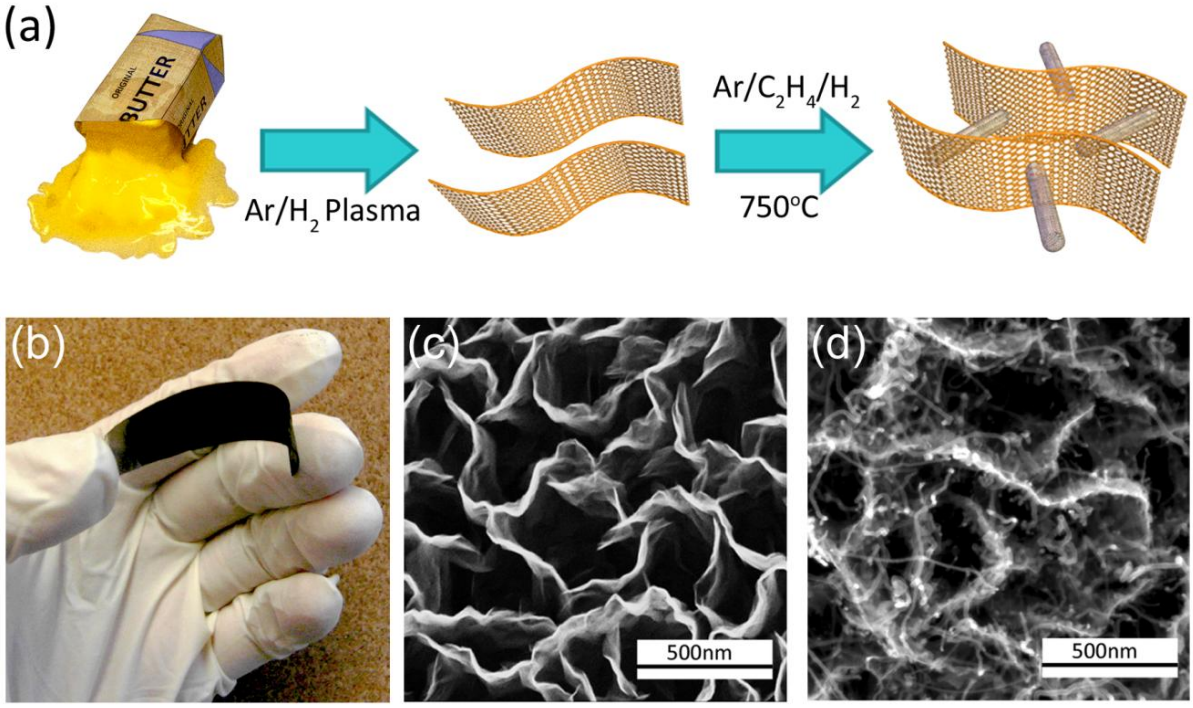

Figure 5.1 (*a) The schematic for the direct growth processes to fuse carbon nanotubes (CNTs) onto vertical graphene nanosheets (VGNS). (b) Photograph of the as-grown VGNS/CNTs hybrid on a flexible graphite substrate. (c) SEM micrograph of pristine VGNS prior to CNT growth. (d) SEM micrograph of the final VGNS/CNTs hybrid structure.*[1]

In particular, VGNS was formed through the plasma transformation of commercially available natural precursor butter.[37,38] The plasma was essential in the formation of VGNS as it not only breaking down the carbon-containing molecules in butter but also re-constructing them into an ordered and vertically standing structure. Conversely, a conventional annealing process of butter will only result in the formation of amorphous carbon.[37] The necessity of the plasma is presumably attributed to the strong plasma-matter interactions presented in the plasma sheath.[34] The butter-derived VGNS also showed strong adhesion to the graphite substrate, and proved to exhibit superior electrochemical properties as opposed to VGNS formed by purified hydrocarbons.[37] This open structure may help to facilitate the electrolyte's access to the active surfaces, which is crucial for efficient charge accumulation in the electrochemical capacitors.[13] The growth of CNTs was then performed in a TCVD process after the deposition of Co/Mo catalyst on VGNS. Figure 5.1b shows the as-grown VGNS/CNTs hybrid structure on a flexible graphite substrate. Figures 5.1c and d show the SEM images of pure VGNS structure and the VGNS/CNTs hybrid obtained after the direct growth process, respectively.

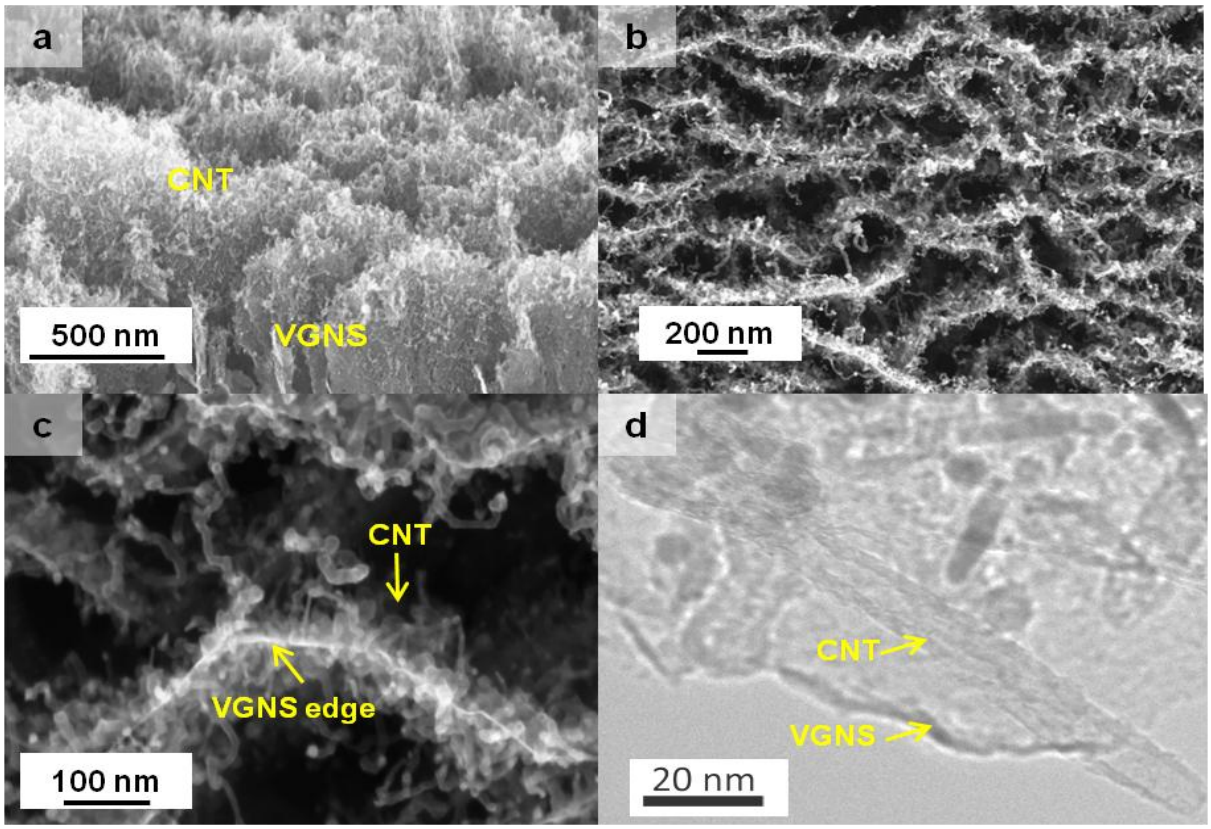

Figure 5.2 *(a) The cross-sectional, (b) low-resolution top-view, and (c) high-resolution SEM images of VGNS/CNTs hybrid structure. (d) TEM image of the VGNS/CNTs hybrid nanostructure, where CNTs and VGNS were identified.*[1]

Figure 5.2 reveals more details of the VGNS/CNTs hybrid structure. The cross-sectional and top-view SEM images of a typical VGNS/CNTs hybrid are given in Figures 5.2a and b respectively. The high-resolution SEM image shown in Figure 5.2c also indicated that CNTs with a typical length of 100 – 500 nm and diameters of 10 – 25 nm radiated from the VGNS structure and linked the neighboring graphene nanosheets. Catalyst nanoparticles were observed on the tips of these nanotubes, indicating a "tip-growth" mechanism of CNTs during the thermal CVD process.[39] Such observation may imply that CNTs were directly "fused" to the VGNS, with possible covalent bondings formed at the interface of VGNS and CNTs.[31] The majority of reactive edge planes of VGNS were preserved, as they were too thin to accommodate the growth of CNTs. Moreover, Figure 5.2d shows the typical transmission electron microscopy (TEM) image of VGNS/CNTs flakes, where multi-walled CNTs with were embedded in the graphene nanosheets.

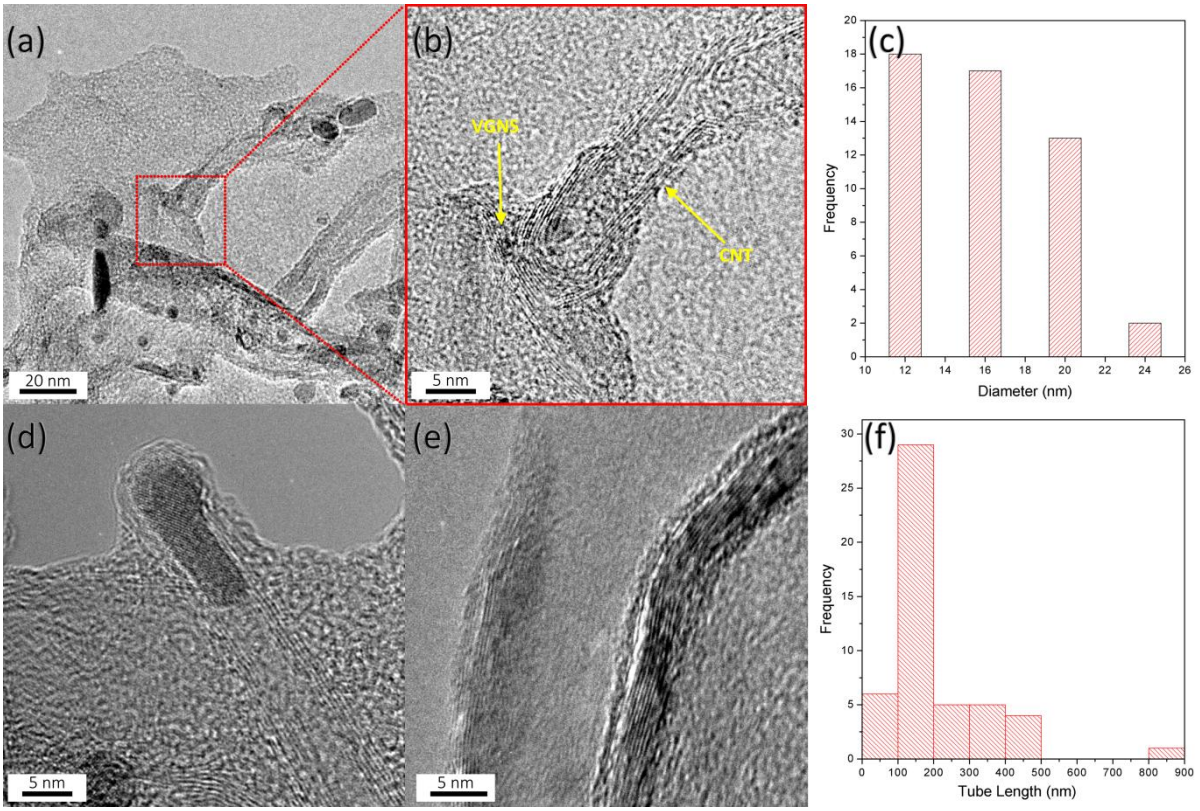

Figure 5.3 (a) TEM image of a carbon nanotube grew on a graphene nanosheet. (b) High-resolution at the junction of CNT and graphene nanosheet as squared in (a). (d) An isolated nanotube with encapsulated catalyst nanoparticles in the tip. (e) High-resolution TEM showing the lattice fringe of the VGNS. The histograms of the CNT's (c) diameter and (f) tube length in the VGNS/CNTs hybrid structure.[1]

High-resolution TEM images shown in Figures 5.3a and b also indicated the plausible "fusion" of CNTs with the supporting graphene nanosheets. In addition, most of the catalyst particles for CNT growth were found to be encapsulated by a graphitic shell (Figure 5.3d), which prevents the generation of pseudocapacitance from faradaic reactions during the operation of supercapacitors. The VGNS used showed typically 3–15 graphitic layers with an average sheet length of 200 nm and a height of ~4 µm. (Figure 5.2a and 5.3e) Using the micrographs from Figure 5.2 and 5.3, the diameter and length of the as-grown CNTs on the VGNS are determined to range from 10-20 nm and on average 150 nm respectively (Figure 5.3c and f).

The surface chemistry of VGNS/CNTs was determined by Raman and X-ray photoelectron spectroscopy (XPS). Figure 5.4a compares the Raman spectra of pristine VGNS and VGNS/CNTs hybrid structure. Pristine VGNS exhibited the characteristic disorder peak (D-band) at 1350 cm^{-1}, the

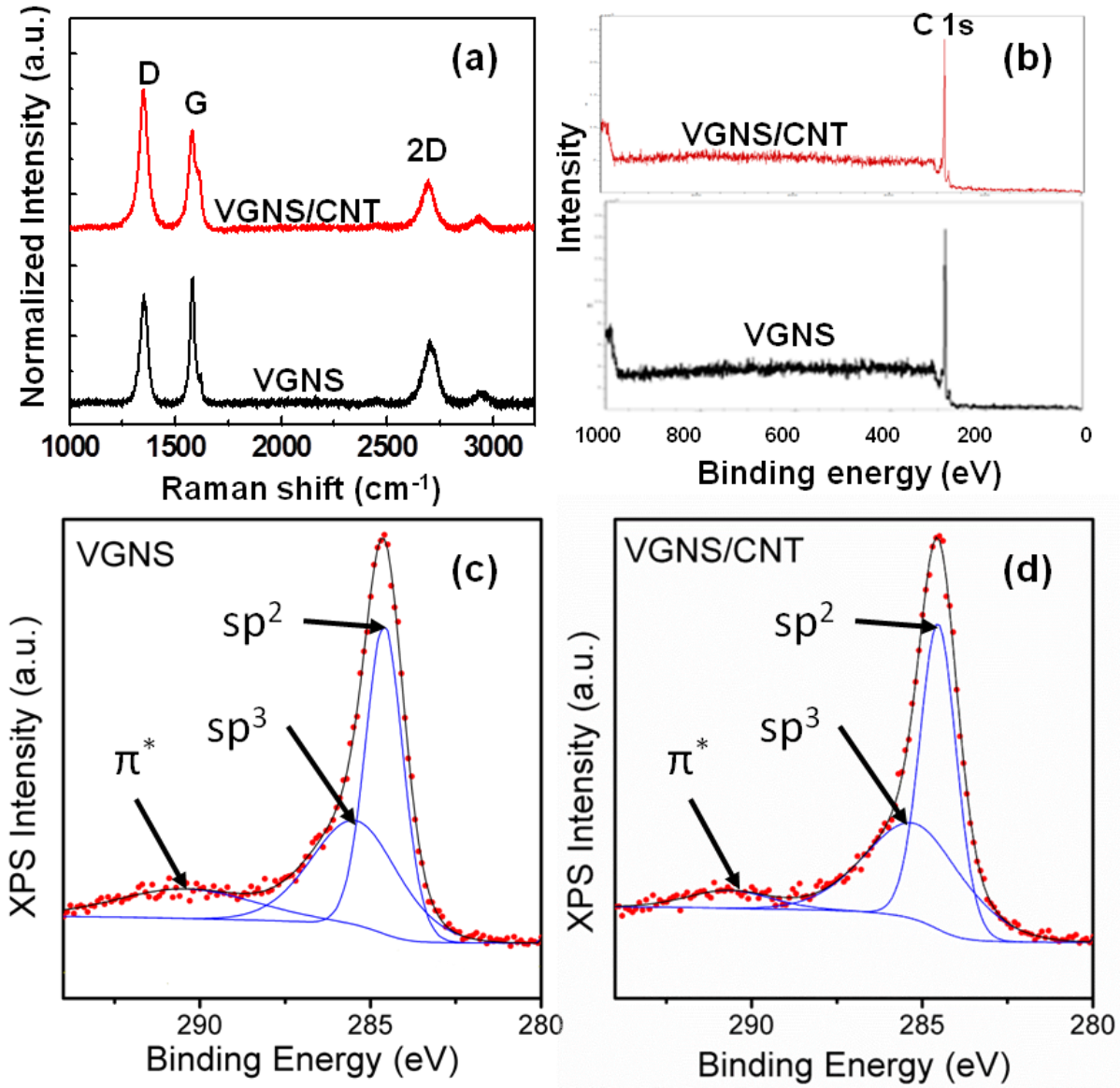

Figure 5.4 *(a) Raman spectra of pristine VGNS (black) and the VGNS/CNTs hybrid structure (red). (b) XPS spectra of both VGNS (black) and VGNS/CNT hybrid structure (red). C 1s narrow scans of (c) VGNS and (d) VGNS/CNTs hybrid. The spectra in c) and d) were fitted with the sp^2, sp^3 and π-π* shake-up features.*[1]

graphitic peak (G-band) at 1583 cm^{-1}, and the second-order 2D-band at 2690 cm^{-1}. The VGNS/CNT hybrid structure, on the other hand, exhibited the same D-band at 1350 cm^{-1}, but a slightly blue-shifted G-band at 1585 cm^{-1} and 2D-band at 2698 cm^{-1}. It is well known that the G-band arises from the in-plane vibrational E_{2g} mode of the sp^2-bonded carbon, the D-band is due to the finite crystallite size effect and/or various defects induced in the sp^2 carbon materials, and the 2D-band is a second-order Raman spectral feature that is sensitive to the three-dimensional interplanar stacking of the hexagonal carbon networks.[40-42] The blue-shifts observed in the G and 2D bands were probably due

to the reduced crystallite size in the hybrid structure or the stress imposed on VGNS after CNTs integration.[33,43,44] Moreover, it was observed that a small increase in the I_D/I_G peak ratio and a small reduction in the I_{2D}/I_G peak ratio by comparing the pristine VGNS with the VGNS/CNTs hybrid. This could be attributed to the reduced graphitic domain size in the hexagonal carbon networks or the extra carbon deposited at the basal planes of VGNS after the CNT growth process.[41,42,45] Indeed, it has been recently demonstrated that the covalent attachment of CNTs on graphene could induce heptagonal carbon rings at the junction, thereby contributing to more disordered structure and a higher D-band peak intensity.[31] These structural changes were also evidenced by the broadening in the full-width-at-half-maximum (FWHM) of the G peaks, which increased from 25 cm^{-1} in the pristine VGNS sample to 42 cm^{-1} in the hybrid structure.[43]

Figure 5.4 also shows the XPS measurements of both VGNS and VGNS/CNTs nanostructures. Only a single strong C 1s peak positioned at binding energy (BE) of ~284.5 eV was found in both spectra, implying that the samples were comprised of mostly carbon atoms. Figures 5.4c and d plotted the C 1s narrow scans of VGNS and VGNS/CNTs hybrid respectively. Both C 1s spectra could be fitted by three peaks corresponding to the carbon sp^2 (BE ~ 284.5 eV), sp^3 (BE ~ 285.4 eV), and the shake-up feature (BE ~ 290.2 eV).[46,47] The lack of features from other elements supported the conclusion that our hybrid structure had a minimal amount of impurities, *e.g.*, oxygen, nitrogen, or metal atoms. In addition, the ratio between the sp^2 and sp^3 contents in the respective C 1s spectra gave further information about the structural changes caused by the combination. The sp^2/sp^3 ratio slightly reduced from 1.25 for the pristine VGNS to 1.17 for the hybrid structure. Since no oxygen or other element was detected in the XPS spectra (Figure 5.4b), the reduced sp^2/sp^3 ratio suggested that the induced change experienced was likely to be the presences amorphous carbon or the covalent attachment between CNTs and VGNS, in a good agreement with the above Raman analyses.

5.3.2 Electrochemical Performance of the VGNS/CNTs Electrodes

The electrochemical performance of pristine VGNS and VGNS/CNT hybrid as binder-free supercapacitor electrodes was then investigated by potentiostat/galvanostat using the three-electrode testing configuration. Figures 5.5a and b show the CV curves of pristine VGNS and VGNS/CNTs hybrid structure in 0.1 M Na_2SO_4 aqueous electrolyte, respectively. It is clearly noticeable that both electrodes showed a near rectangular shape in CVs at low scan rates, suggesting the efficient formation of EDL and fast ion transport in both VGNS and hybrid structures.[13] Nevertheless, the curves became skewed for both electrodes at high scan rates (*e.g.*, 500 mV s^{-1}). A question may arise here as to whether the catalyst nanoparticles used for CNT growth made contribution to the charge storage mechanism. After all, both Co and Mo are well known to undergo electrochemical redox reactions to provide pseudocapacitance.[48,49] While the potentials required for Mo redox reactions are beyond the potential windows operated in this work,[50] the absence of redox peaks at 0.06 and 0.09 V or 0.25 and 0.3 V indicated the lack of electrochemical activity from Co.[51,52] Furthermore, neither Co nor Mo were detected in the XPS analysis of the hybrid structure (detection limit was <0.1 wt%; see Figure 5.4b). It was suspected that the undetectable quantity of Co and Mo was probably due to the encapsulation of catalyst nanoparticles by CNTs during the growth process (Figure 5.3d).[53] It has been demonstrated that the internal space of CNTs remains inaccessible to electrolyte unless the tubes are first opened.[54] Thus, the electrochemical contributions of the Co and Mo nanoparticles would be negligible.

Figures 5.5c and d show the galvanostatic charge/discharge curves of pristine VGNS and VGNS/CNTs hybrid structures at different current densities of 2, 4, and 8 A g^{-1} respectively. A linear dependence between the discharge potential and time was identified in the discharge curves, further indicating the absence of major Faradaic processes.[55] These results are consistent with the structural analyses that the electrodes were composed of mostly carbon-based materials and the charge storage occurred mainly through the EDL mechanism.[7]

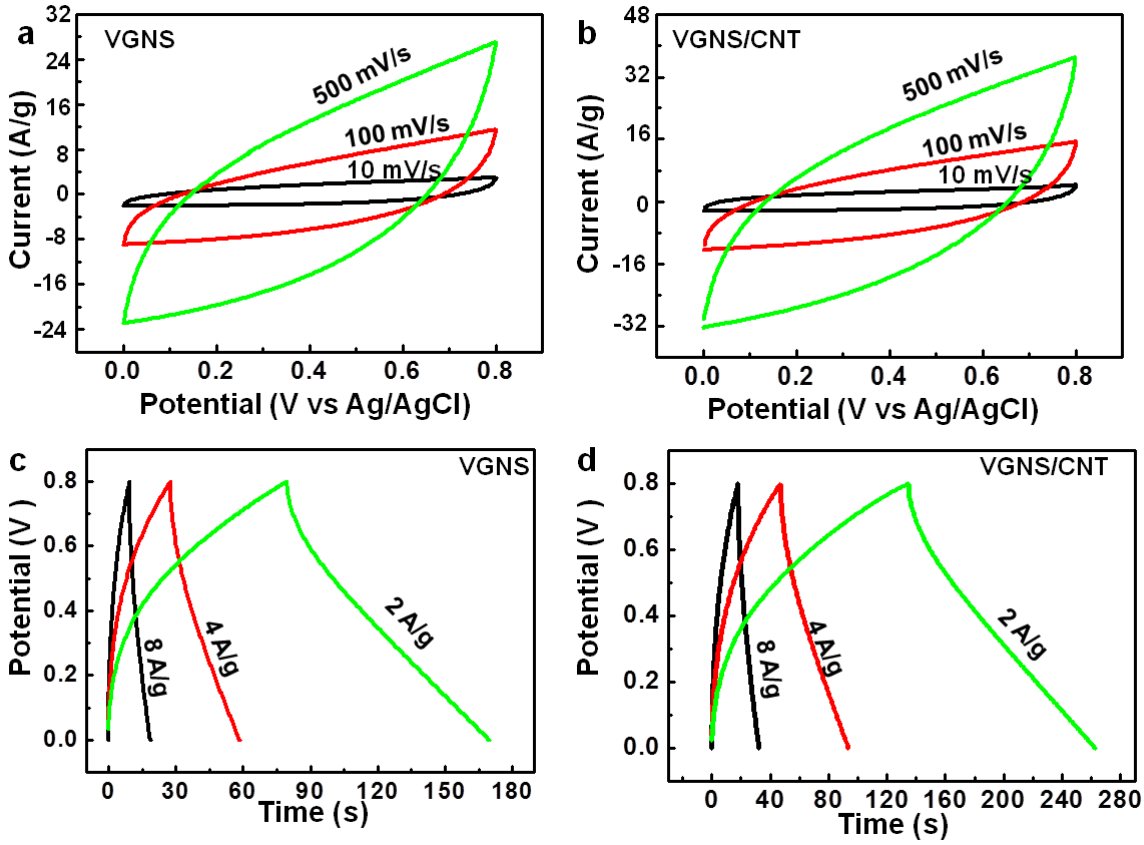

Figure 5.5 *CV curves of (a) pristine VGNS and (b) VGNS/CNTs hybrid structure at different scan rates of 10, 100 and 500 mV s^{-1}. Galvanostatic charge/discharge plots of (c) pristine VGNS and d) VGNS/CNTs hybrid structure at a current density of 2, 4, and 8 A/g.*[1]

The cycle stability tests are shown in Figure 5.6a, where both VGNS and VGNS/CNT hybrid structures exhibited retention of >99% of their initial capacitance after 1,000 cycles performed at 5 A g^{-1}. In addition, Figures 5.6b and c showed almost equivalent discharge curves between the 1st and the 1000th cycles, clearly evidencing the excellent stability of the electrode materials.

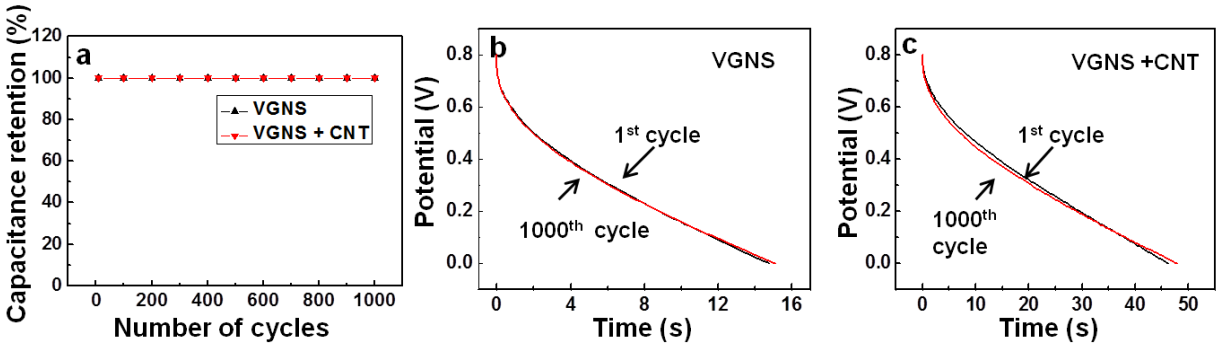

Figure 5.6 *(a) Cycle stability of the VGNS and VGNS/CNTs hybrid structures at 5 A g^{-1} for 1000 cycles. (b) Discharge curves of VGNS for the 1st (black) and 1000th cycles (orange hollow triangle). (c) Discharge curves of VGNS/CNTs hybrid structure for the 1st (red) and 1000th (blue hollow triangle) cycles.*[1]

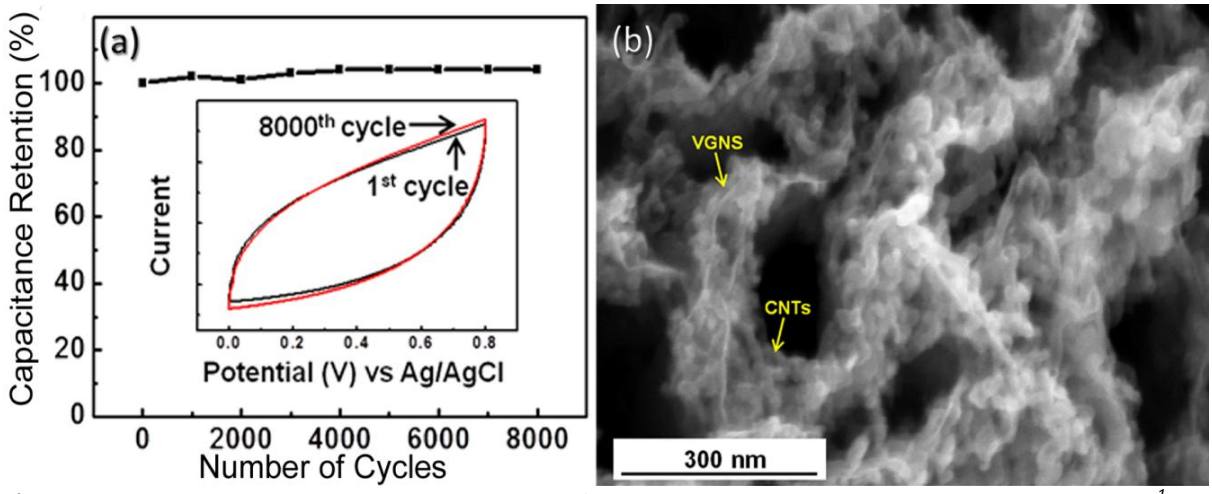

Figure 5.7 *(a) Capacitance retention test for VGNS/CNTs hybrid performed at a scan rate of 100 mV s^{-1} for 8,000 cycles. Inset shows the CV curves at the 1st and 8,000th cycles. (b) SEM image of the VGNS/CNTs hybrid structure after 8,000 cycles at 100 mV s^{-1}.*[1]

The stability of the electrodes was further tested using cyclic voltametry, where >99% retention for the hybrid structure was again observed even after 8000 cycles at 100 mV s^{-1} (Figure 5.7a). Slight increase in capacitance was observed at the end of 8000 cycles which could arise from the greater wetting of the electrodes through capillary action as the cycling measurement proceeded.

This stability of VGNS/CNTs hybrid was remarkable as compared to other typical 3D nano-carbon structures reported in the literature; for example, *Chen et al.* obtained 90% retention after 3000 cycles for the graphene oxide hydrogels; *Mhamane et al.* obtained 93% retention after 1000 cycles for the hierarchically perforated graphene nanosheets.[56,57] The observed stability was attributed to the structural durability and the EDL charge storage mechanism of carbon-based materials, as opposed to metal oxide nanostructures which often show low capacitance retention due to a significant degradation to the nanostructures from redox reactions.[25] Microscopic analysis indicated that CNTs remained bound to VGNS in the hybrid structure even after the 8000th cycle, with the change in microstructure most likely due to capillary forces upon the evaporation of the electrolyte (see Figure 5.7b). The excellent stability thus provides an additional proof that the Faradaic contribution from the active material or metal catalysts was clearly not a dominating contributor in the present hybrid electrodes.

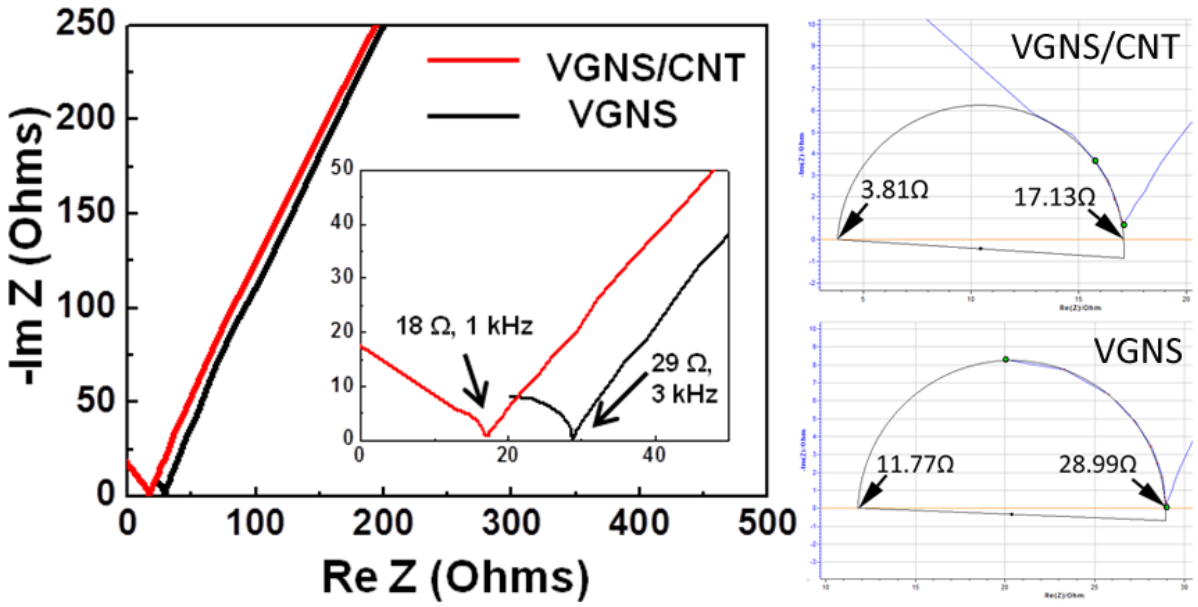

Figure 5.8 *Nyquist plot of (black) pristine VGNS and (red) VGNS/CNTs hybrid structure. Inset shows the enlarged view at the frequencies where the curves intersect with the real-Z axis and the semicircle fit.*

The electrochemical impedance spectra (EIS) for pristine VGNS and hybrid structure were shown in the Nyquist plot (Figure 5.8), where the frequency-dependent impedance was given as the real (Z') and imaginary (Z'') components. Both samples displayed a vertical curve feature at low frequencies, indicating a near ideal capacitive behavior.[55] In the high-frequency range, a semicircle was observed to intersect with the real (Z') axis in both spectra, which could be attributed to charge transfer at the electrode-electrolyte interface.[58] The charge transfer resistance (R_{ct}) calculated from the diameter of the semicircles show that the hybrid structure has a lower R_{ct} (13.3 Ω) than the pure VGNS (17.2 Ω), suggesting that the hybrid structure had a lower charge transfer resistance. It is possible that the attachment of highly-conductive CNTs had enhanced the charge transfer processes.

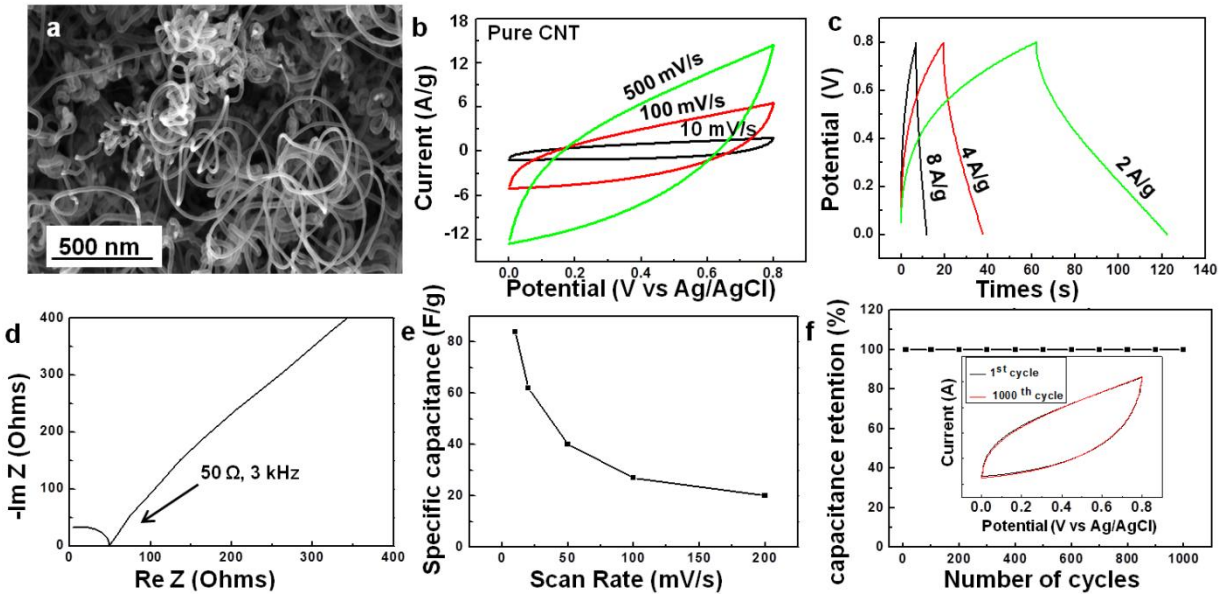

Figure 5.9 *(a) The SEM image and (b) the corresponding CV curve of CNT arrays. (c) The galvanostatic charge-discharge curves of the CNT arrays at current densities of 2, 4 and 8 A/g. (d) The Nyquist plot, (e) the rate capability, and (f) the stability test performed for 1,000 cycles at 100 mV/s of the CNT arrays.*[1]

Thus far, the performance of hybrid electrode has only been compared to VGNS. In order to demonstrate the complementary nature of the combination, the performance of CNT electrodes was also evaluated. CNTs were grown directly on graphite paper using the same process. Figure 5.9 displays the electrochemical performance of the CNT electrode. Though the as-grown CNT arrays also exhibited >99% capacitance retention over 1,000 cycles at 100 mV s^{-1}, a specific capacitance of merely 84 F g^{-1} was observed at 10 mV s^{-1} in the three-electrode cell configuration. In contrast, the capacitance was noticeably enhanced when the CNTs were grown on the VGNS (Figure 5.5). Taking the mass loading of CNTs (~30 µg) into account, the CNTs contributed a specific capacitance of 240 F g^{-1} in the hybrid structure. This value is much higher than what is normally achieved for CNTs.[22] The reasons for this enhancement can be understood through considering common factors which hinder the specific capacitance of CNT-based devices. As aforementioned, the effective utilisation of surface areas were often hindered in CNT arrays due to tube bundling when immersed in the aqueous electrolytes.[59] The morphology of hybrid structure as seen in the SEM micrographs of Figures 5.1 and 5.2 overcame this problem by anchoring CNTs onto a rigid structure provided by the VGNS support. This facilitated effective ion transport and near-total accessibility to the CNTs' surface.

Secondly, the high contact resistance between electrode and the current collector limits their performance.[60,61] By comparing the EIS of both the hybrid structure (Figure 5.8) and the CNT arrays (Figure 5.9d), it can be seen that the hybrid electrode exhibited a much lower charge transfer resistance. These factors together led to the synergistic effects in boosting the electrochemical performance of CNTs in the hybrid electrodes.

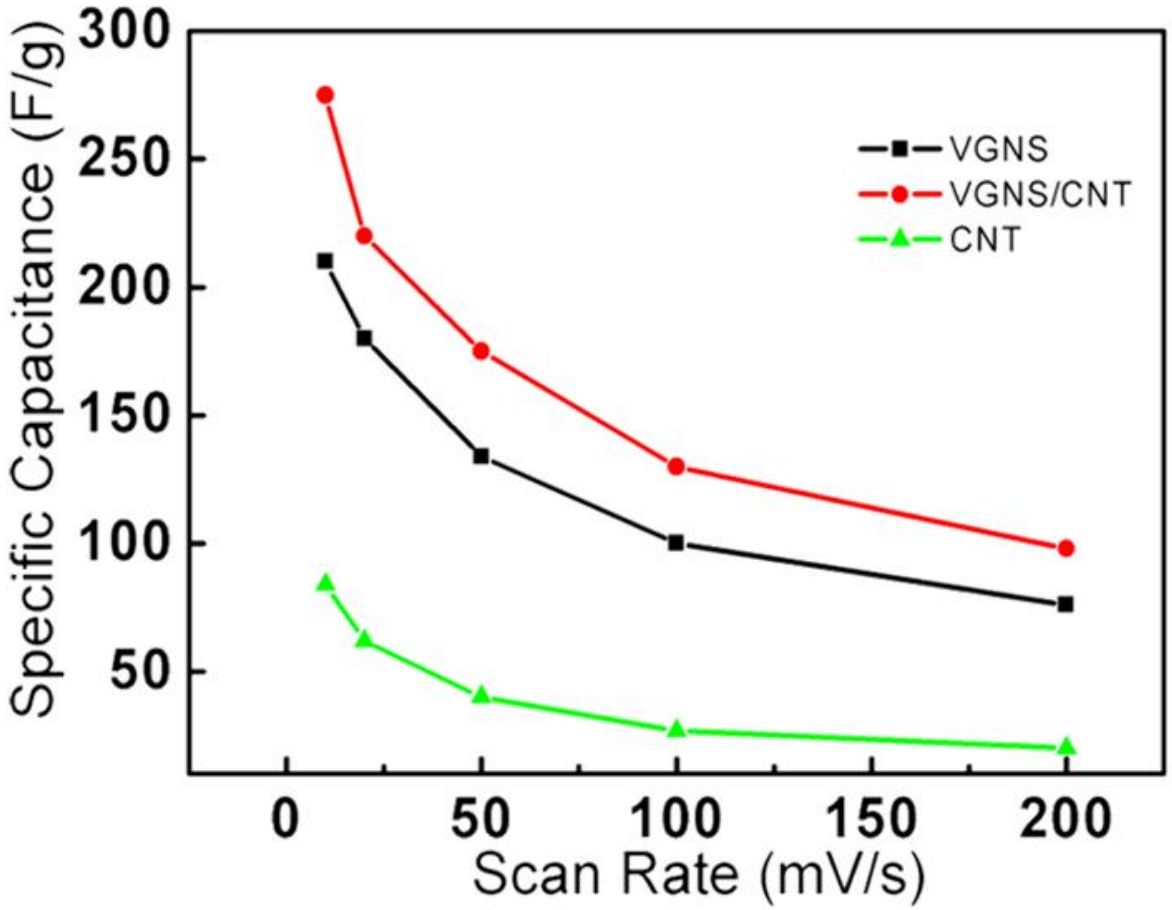

Figure 5.10 *Rate capabilities of pristine VGNS (black), VGNS/CNTs hybrid structures (red) and pure CNT (Green).*[1]

The specific capacitance (C_S) of each material obtained at different scan rates (of the CV measurements) are shown in Figure 5.10 (excluding the capacitance contribution from the pristine graphite paper). A decrease in C_S was observed for all electrode materials as the scan rates increased, similar to that of other corrugated three dimensional graphene based structure.[62] It is also seen that the hybrid structure has a consistently higher specific capacitance as compared to either VGNS or CNTs. For example, the specific capacitance of VGNS and CNTs are 206 and 84 F g^{-1} at

10 mV s^{-1}, whereas the hybrid structures show a significantly enhanced value of 278 F g^{-1} at the same scan rate. The observed improvement is attributed to factors such as the enlarged surface area, improved electrical conductivity, and higher electrochemical activity of the synergistically fused hybrid nanostructure, where the ions can easily access the edge planes, basal planes, and CNT sidewalls.[6,27,63] The C_S exhibited by the hybrid structure is among the highest values reported for carbon-based supercapacitor electrodes and is also superior as compared to other carbon structures with similar 3D morphology, such as reduced graphene oxide sheets and mechanically combined graphene/CNT composite structures.[64,65] This marked trend in the capacitance also indicated that even by incorporating a small quantity of CNTs on the VGNS, a significant increase in performance could be obtained.

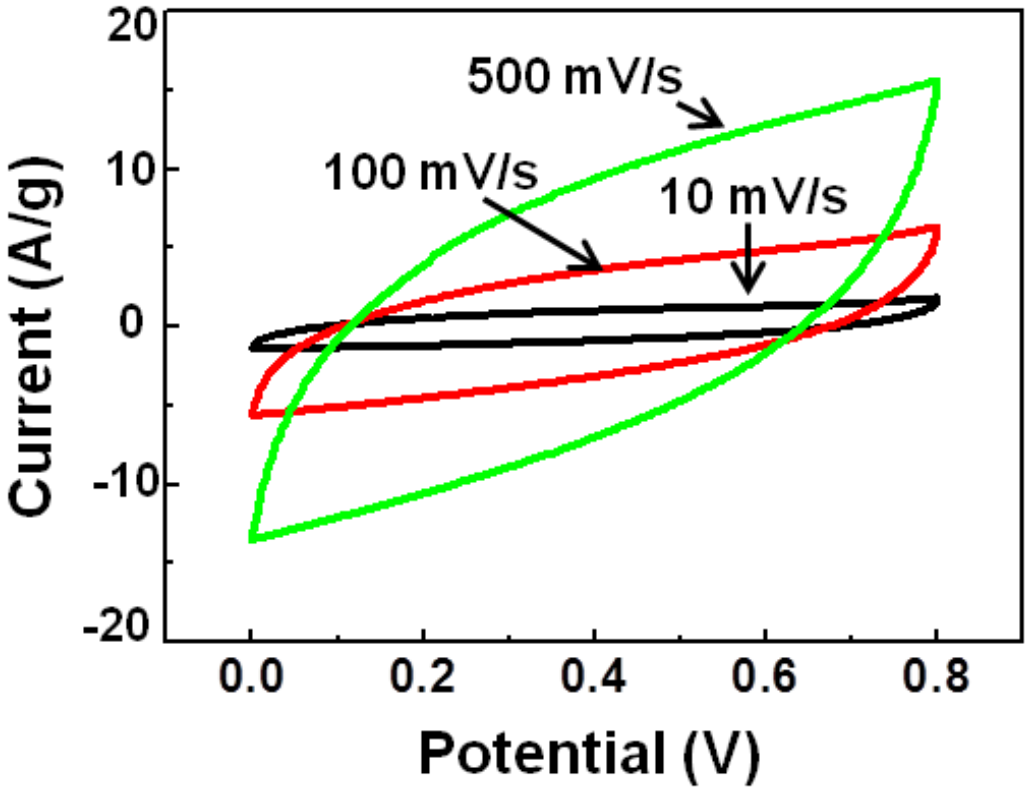

Figure 5.11 *CV curves of the two-electrode cell configuration of the VGNS/CNTs hybrid structure at different scan rates*

To better evaluate the performance of the hybrid electrode as compared to real world devices, two-electrode cell measurements were also carried out (Figure 5.11).[66] Just as the three-electrode setup, the specific capacitance C_s was calculated by $C_S = (\int \mathrm{I}\,\mathrm{dV}/\mathrm{vm}\Delta\mathrm{V})$. However, since both

electrodes consisted of the hybrid material, the mass of the active material in consideration is doubled. The results showed that the hybrid structure had a cell capacitance of 131 F g^{-1} at 10 mV s^{-1}, in a good agreement with the three-electrode cell measurements.

These values have been evaluated against other graphene/CNTs hybrid systems fabricated by the direct growth or solution-based mixing methods (Table 5.1). It was found that the present hybrid structure have superior performance compared to the hybrids reported recently.[29,32,48,67] With further optimization on the CNT density and electrolyte ion penetration depth, the performance of this hybrid nanostructure may further be enhanced.

Electrode material	Cell configuration	Electrolyte	C_s (F/g)	Methods	References
VGNS/CNTs	3-electrode	0.1M Na_2SO_4	278	Direct Growth	This work
	2-electrode	0.1M Na_2SO_4	131		
Metal/Graphene/CNTs	2-electrode	6M KOH	100 at 1 A/g	Direct Growth	[68]
Graphene/CNTs Sandwich	3-electrode	6M KOH	385 at 10 mV/s	Solution-based mixing	[69]
Graphene/CNTs Layer-by-layer	3-electrode	1M H_2SO_4	125 at 10 mV/s	Solution-based mixing	[70]
Graphene Oxide/CNTs Composite	3-electrode	1M H_2SO_4	251 at 5 mV/s	Solution based mixing	[71]

Table 5.1 *Comparison of the specific capacitance (F/g) reported in the present work with those values from recently published graphene/CNTs hybrids.*

5.3.3 Critical Factors in the VGNS/CNTs Electrodes

In order to unveil the critical factor which enabled the synergistic integration between VGNS and CNTs, factors such as catalyst thickness, catalyst composition and the presences of an oxidative etchant during growth were systematically explored.

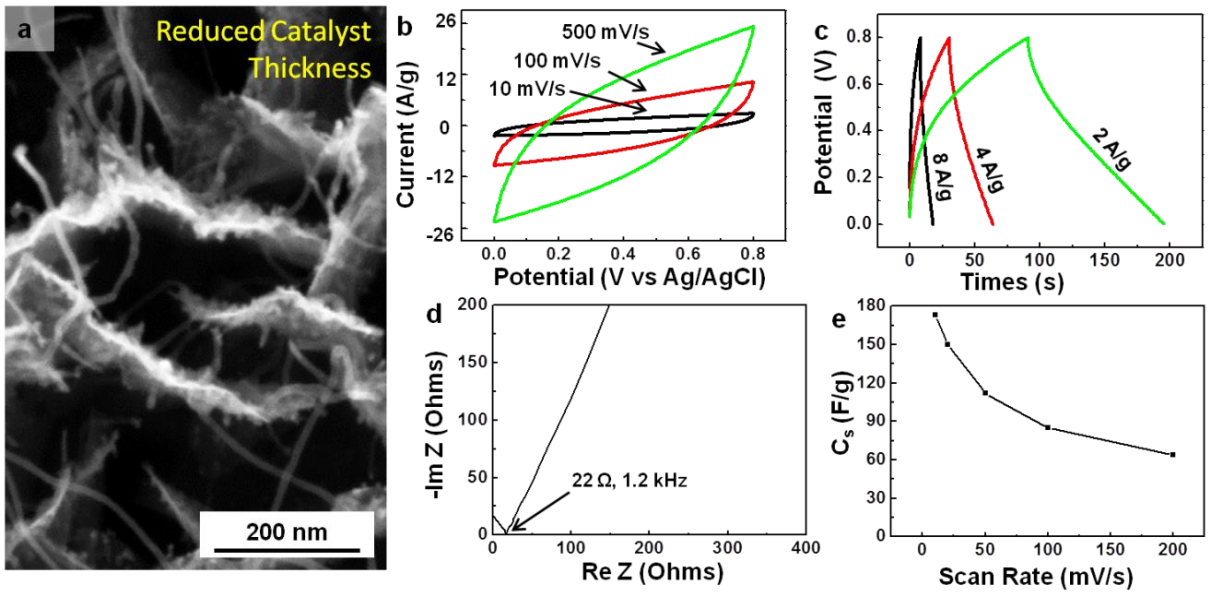

Figure 5.12 *(a) The SEM image and (b) the corresponding CV curve of VGNS/CNTs hybrid grown with thinner Co/Mo catalyst. (c) The galvanostatic charge-discharge curves performed at current densities of 2, 4 and 8 A/g. (d) The Nyquist plot and (e) rate capability of the VGNS/CNTs hybrid grown with thinner Co/Mo catalyst*.[1]

Firstly, the thickness of the Co/Mo catalyst was reduced from 1 nm to 0.5 nm in order to obtain thinner CNTs which have a higher theoretical surface area and therefore the possibility of a greater specific capacitance.[72] After the growth of CNTs, the mass loading was ~125 μg/cm^2. While the diameter of the as-grown CNTs indeed decreased, it also resulted in a lower density of CNTs on the VGNS (Figure 5.12a). The electrochemical performance of this structure exhibited a significant drop in specific capacitance from 278 F g^{-1} to 178 F g^{-1}. This poor charge storage capability may arise from the side effects during CNT growth, *i.e.*, the deposition of amorphous carbons when too few catalyst nanoparticles were present.[73] The increase in charge transfer resistance from the EIS spectra seemed to support this possibility (Figure 5.12d). The observations thus demonstrated that a certain threshold in the population of the catalyst nanoparticles were necessary to enable a high tapping density of CNTs and minimize the detrimental effects caused to the original VGNS structure.

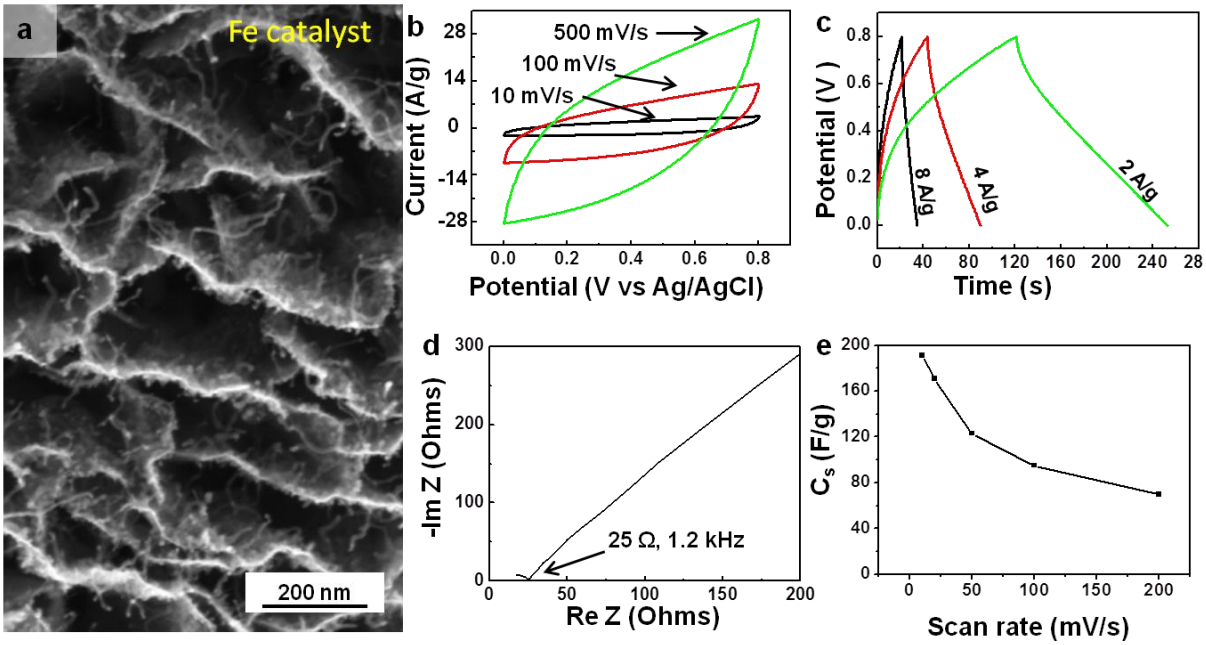

Figure 5.13 *(a) The SEM image and (b) the corresponding CV curve of VGNS/CNTs hybrid grown with Fe catalyst. (c) The galvanostatic charge-discharge curves performed at current densities of 2, 4 and 8 A/g. (d) The Nyquist plot and (e) rate capability of the VGNS/CNTs hybrid grown with Fe catalyst.*[1]

Secondly, the Co/Mo catalyst was substituted with a Fe catalyst. Although Fe is known for possessing a higher catalyst activity, the density and length of CNTs were not greater than those obtained from the Co/Mo catalyst (Figure 5.13a). Nevertheless, the mass of the electrode increased to ~175 μg/cm^2 which was a 35% increase as compared to the mass obtained from the standard procedure. This could be again due to the deposition of amorphous carbons because of the de-activation of Fe at high temperatures. Furthermore, the thickened basal planes of the VGNS were observed to have thickened from the SEM image (Figure 5.13a).[74,75] Again an increase in the transfer resistance was observed in the EIS (Figure 5.13d). As a result, the difference in the microstructure resulted in a decrease of the C_S from 278 F g^{-1} to 191 F g^{-1}.

Lastly, the effects of an etchant were investigated through the addition of a trace amount of water in the CNT growth process. This was done in an attempt to increase the tapping density of CNTs and reduce the presence of amorphous carbon in the hybrid structure as the addition of water had been known to enhance CNT growth.[76] After the growth of CNTs, the mass loading increased to ~150 μg/cm^2.

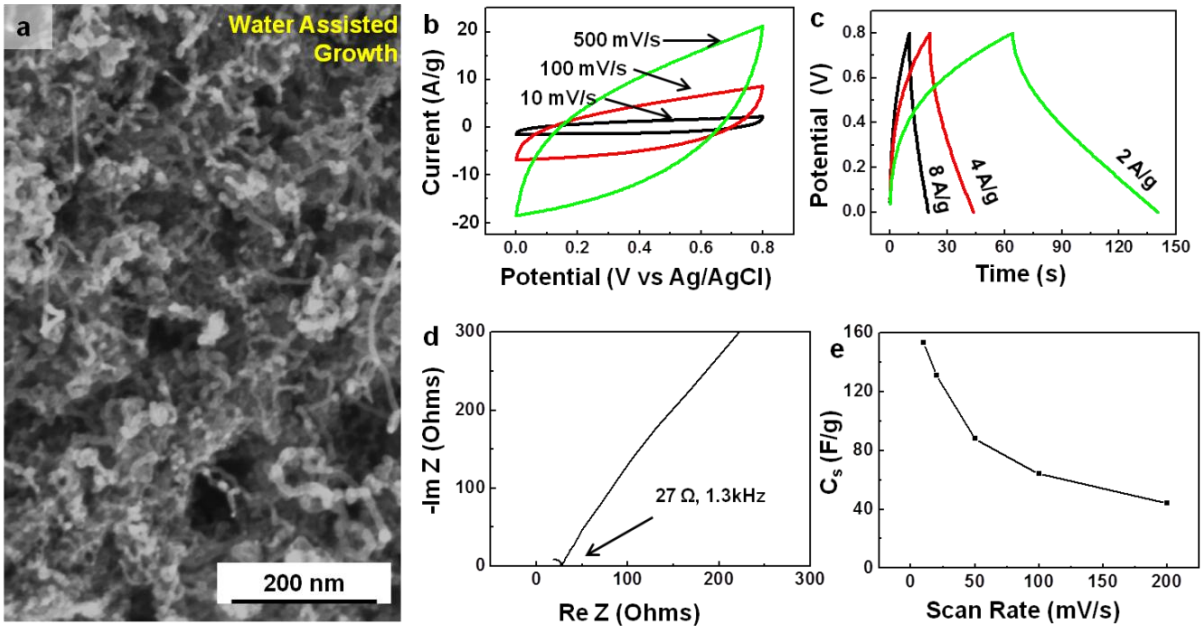

Figure 5.14 *(a) The SEM image and (b) the corresponding CV curve of VGNS/CNTs hybrid grown with water assistance. (c) The galvanostatic charge-discharge curves performed at current densities of 2, 4 and 8 A/g. (d) The Nyquist plot and (e) rate capability of the VGNS/CNTs hybrid grown with water assistance.*[1]

Though the CNT density increased significantly, the density of the exposed reactive edge planes of VGNS was reduced (Figure 5.14a). This reduction could be due to the coverage of VGNS by CNTs and/or the etching effect of water molecules.[76,77] Consequently, ion transport to the reactive edge planes was impeded and a significant drop in the specific capacitance from 278 F g^{-1} to 153 F g^{-1} was observed (Figure 5.14). This clearly demonstrates that the reactive edge planes must be preserved and accessible in the VGNS/CNTs hybrid structure to provide effective charge storage for optimal performance.

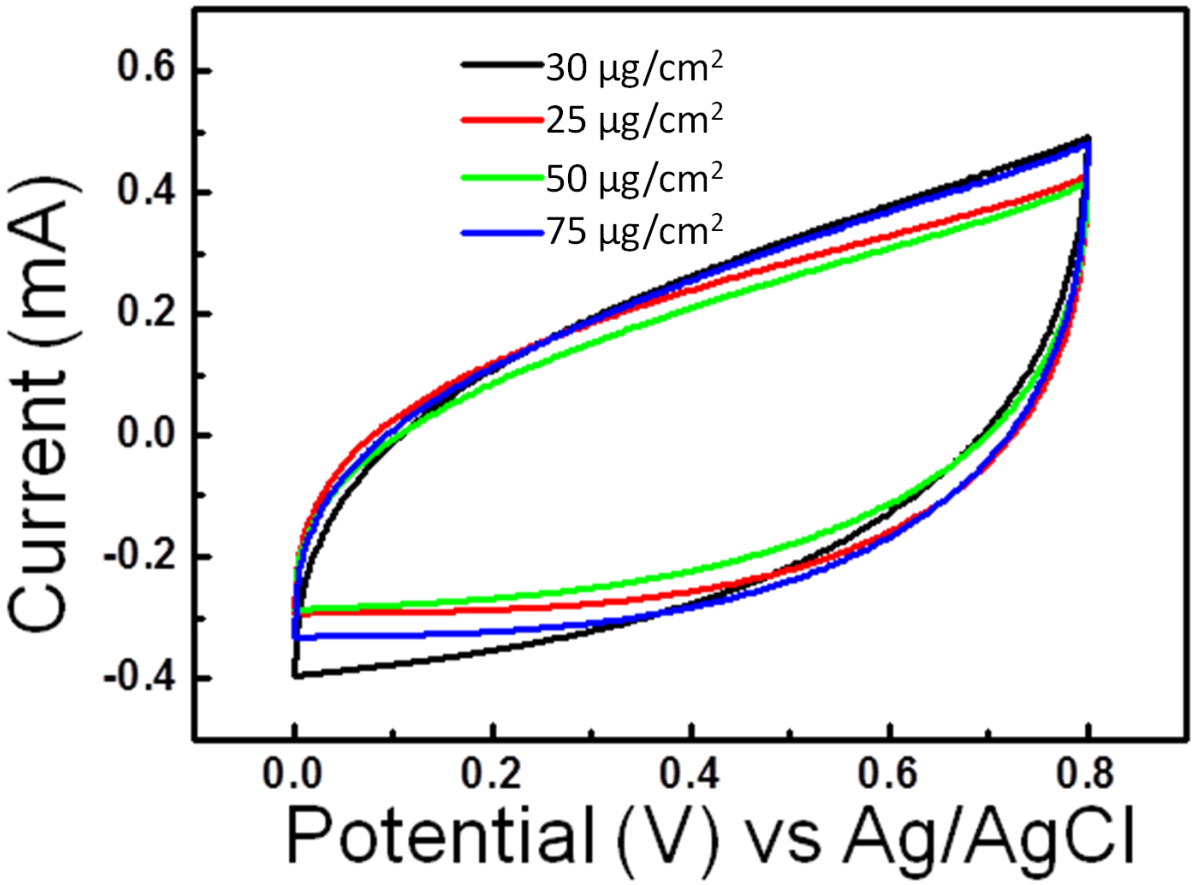

Figure 5.15 *CV curves of the VGNS/CNTs with different CNT mass loading. The black indicates the CV curve of the optimal condition, the red being that of a reduced catalyst thickness, green being that from the water-assisted growth, and blue being that of Fe catalyst. Data are combined from the above three studies and the optimum condition reported in the text.*[1]

In order to compare the effects of the above modification on their electrochemical performances, Figure 5.15 superimposed the various CV curves with that obtained by the hybrid grown under the optimum condition. The different curves are denoted by the difference mass loading of the process (*i.e.,* the total mass loading – the specific mass of VGNS). To reiterate, the standard procedure yielded a net mass loading of 30 μg/cm^2. The mass loading dropped to 25 μg/cm^2 when the catalyst was thinned. The substitution of Fe as the growth catalyst resulted in a mass loading of 75 μg/cm^2. Finally, the water-assisted process resulted in a mass loading of 50 μg/cm^2. The swipe was carried out at 10 mV/s. It can be seen that the black curve representing the electrochemical performance of the optimal condition encompassed the largest area. After taking into account the electrode mass, it would also exhibit the highest specific capacitance. The spectra clearly showed that the integration

of CNTs onto VGNS was highly susceptible to the experimental condition. Therefore, for complimentary integration to occur, optimum conditions are required. These rigorous optimization processes suggested that the synergistic integration of VGNS and CNTs required suppressing the deposition of low-capacitance material (*e.g.,* amorphous carbon), preserving the reactive edges of VGNS, and also maximizing the CNT density.

5.4 Chapter Conclusion

This chapter presented a feasible approach to fuse CNTs and VGNS into a hybrid structure via a direct growth method. The impacts on their supercapacitor performance were then evaluated. The resultant VGNS/CNTs hybrid nanostructure was shown to be mechanically robust and possessed good conductivity and a high surface area for the EDL formation. Furthermore, the integration of VGNS and CNTs solved the intrinsic problems persistent in both structures. The investigation also showed critical factors which affected their integration, which include suppressing of amorphous carbon, maximizing the density of CNTs and preserving the reactive edges of VGNS. As the integration of CNTs on VGNS was substrate-independent, this also allowed the supercapacitor electrodes to be assembled on many substrates including the flexible and conductive graphite paper. These results are promising for the utilization of carbon-based electrodes and may lead to better understanding of the elementary charge storage processes, which are critical for the development of next-generation energy storage devices.

5.5 References

[1] Seo D. H., Yick S., Han Z. J. *et al.* **Synergistic Fusion of Vertical Graphene Nanosheets and Carbon Nanotubes for High-Performance Supercapacitor Electrodes**. *ChemSusChem*. 2014;10.1002/cssc.201402045.

[2] Tollefson J. **How green is my future?** *Nature*. 2011; 473 (7346): 134-5.

[3] Service R. F. **New 'supercapacitor' promises to pack more electrical punch**. *Science*. 2006; 313 (5789): 902.

[4] Manthiram A., Fu Y., Su Y.-S. **In charge of the world: electrochemical energy storage**. *J. Phys. Chem. Lett.* 2013; 4 (8): 1295-7.

[5] Miller J. R., Simon P. **Electrochemical capacitors for energy management**. *Science*. 2008; 321 (5889): 651-2.

[6] Jiang H., Lee P. S., Li C. **3D carbon based nanostructures for advanced supercapacitors**. *Energy Environ. Sci.* 2013; 6 (1): 41-53.

[7] Simon P., Gogotsi Y. **Capacitive energy storage in nanostructured carbon-electrolyte systems**. *Acc. Chem. Res.* 2013; 46 (5): 1094-103.

[8] Simon P., Gogotsi Y. **Materials for electrochemical capacitors**. *Nat. Mater.* 2008; 7 (11): 845-54.

[9] Li J., Cheng X., Shashurin A., Keidar M. **Review of electrochemical capacitors based on carbon nanotubes and graphene**. *Graphene*. 2012; 1: 1-13.

[10] Su D. S., Schlögl R. **Nanostructured Carbon and Carbon Nanocomposites for Electrochemical Energy Storage Applications**. *ChemSusChem*. 2010; 3 (2): 136-68.

[11] Miller J. R., Outlaw R. A., Holloway B. C. **Graphene double-layer capacitor with ac line-filtering performance**. *Science*. 2010; 329 (5999): 1637-9.

[12] Sheng K., Sun Y., Li C. *et al.* **Ultrahigh-rate supercapacitors based on eletrochemically reduced graphene oxide for ac line-filtering**. *Sci. Rep.* 2012; 2: 247.

[13] El-Kady M. F., Strong V., Dubin S., Kaner R. B. **Laser scribing of high-performance and flexible graphene-based electrochemical capacitors**. *Science*. 2012; 335 (6074): 1326-30.

[14] Yang X., Zhu J., Qiu L., Li D. **Bioinspired effective prevention of restacking in multilayered graphene films: towards the next generation of high-performance supercapacitors**. *Adv. Mater.* 2011; 23 (25): 2833-8.

[15] Cheng Y., Lu S., Zhang H. *et al.* **Synergistic effects from graphene and carbon nanotubes enable flexible and robust electrodes for high-performance supercapacitors**. *Nano Lett.* 2012; 12 (8): 4206-11.

[16] Lin H., Li L., Ren J. *et al.* **Conducting polymer composite film incorporated with aligned carbon nanotubes for transparent, flexible and efficient supercapacitor**. *Sci. Rep.* 2013; 3.

[17] Hahm M. G., Leela Mohana Reddy A., Cole D. P. *et al.* **Carbon Nanotube–Nanocup Hybrid Structures for High Power Supercapacitor Applications**. *Nano Letters*. 2012; 12 (11): 5616-21.

[18] Ervin M. H., Mailly B., Palacios T. **Electrochemical double layer capacitance of metallic and semiconducting SWCNTs and single layer graphene**. *ECS Trans.* 2012; 41 (22): 153-60.

[19] Pico F., Pecharroman C., Ansón A. *et al.* **Understanding Carbon–Carbon Composites as Electrodes of Supercapacitors: A Study by AC and DC Measurements**. *J. Electrochem. Soc.* 2007; 154 (6): A579-A86.

[20] Hiraoka T., Yamada T., Hata K. *et al.* **Synthesis of single- and double-walled carbon nanotube forests on conducting metal foils**. *J. Am. Chem. Soc.* 2006; 128 (41): 13338-9.

[21] Talapatra S., Kar S., Pal S. K. *et al.* **Direct growth of aligned carbon nanotubes on bulk metals**. *Nat. Nanotech.* 2006; 1 (2): 112-6.

[22] Zhang L. L., Zhao X. S. **Carbon-based materials as supercapacitor electrodes**. *Chem. Soc. Rev.* 2009; 38 (9): 2520-31.

[23] You B., Li N., Zhu H. *et al.* **Graphene Oxide-Dispersed Pristine CNTs Support for MnO_2 Nanorods as High Performance Supercapacitor Electrodes**. *ChemSusChem*. 2013; 6 (3): 474-80.

[24] Huang F., Lou F., Chen D. **Exploring Aligned-Carbon-Nanotubes@Polyaniline Arrays on Household Al as Supercapacitors**. *ChemSusChem*. 2012; 5 (5): 888-95.

[25] Conway B. E., Birss V., Wojtowicz J. **The role and utilization of pseudocapacitance for energy storage by supercapacitors**. *J. Power Sources*. 1997; 66 (1–2): 1-14.

[26] Liang Y., Schwab M. G., Zhi L. *et al.* **Direct access to metal or metal oxide nanocrystals integrated with one-dimensional nanoporous carbons for electrochemical energy storage**. *J. Am. Chem. Soc.* 2010; 132 (42): 15030-7.

[27] Zhi M., Xiang C., Li J. *et al.* **Nanostructured carbon–metal oxide composite electrodes for supercapacitors: a review**. *Nanoscale*. 2013; 5 (1): 72-88.

[28] Yu A., Park H. W., Davies A. *et al.* **Free-standing layer-by-layer hybrid thin film of graphene-MnO_2 nanotube as anode for lithium ion batteries**. *J. Phys. Chem. Lett.* 2011; 2 (15): 1855-60.

[29] Aboutalebi S. H., Chidembo A. T., Salari M. *et al.* **Comparison of GO, GO/MWCNTs composite and MWCNTs as potential electrode materials for supercapacitors**. *Energy Environ. Sci.* 2011; 4 (5): 1855-65.

[30] Chen P., Xiao T.-Y., Qian Y.-H. *et al.* **A nitrogen-doped graphene/carbon nanotube nanocomposite with synergistically enhanced electrochemical activity**. *Adv. Mater.* 2013; 25 (23): 3192-6.

[31] Zhu Y., Li L., Zhang C. *et al.* **A seamless three-dimensional carbon nanotube graphene hybrid material**. *Nat. Comm.* 2012; 3: 1225.

[32] Yan Z., Ma L., Zhu Y. *et al.* **Three-dimensional metal-graphene-nanotube multifunctional hybrid materials**. *ACS Nano*. 2013; 7 (1): 58-64.

[33] Rao R., Chen G., Arava L. M. R. *et al.* **Graphene as an atomically thin interface for growth of vertically aligned carbon nanotubes**. *Sci. Rep.* 2013; 3: 1891.

[34] Ostrikov K., Neyts E. C., Meyyappan M. **Plasma nanoscience: from nano-solids in plasmas to nano-plasmas in solids**. *Adv. Phys.* 2013; 62 (2): 113-224.

[35] El-Kady M. F., Kaner R. B. **Scalable fabrication of high-power graphene micro-supercapacitors for flexible and on-chip energy storage**. *Nat. Comm.* 2013; 4: 1475.

[36] Nishide H., Oyaizu K. **Toward flexible batteries**. *Science*. 2008; 319 (5864): 737-8.

[37] Seo D. H., Han Z. J., Kumar S., Ostrikov K. **Structure-controlled, vertical graphene-based, binder-free electrodes from plasma-reformed butter enhance supercapacitor performance**. *Adv. Energy Mater.* 2013; 3 (10): 1316-23.

[38] Seo D. H., Rider A. E., Han Z. J. *et al.* **Plasma break-down and re-build: same functional vertical graphenes from diverse natural precursors**. *Adv. Mater.* 2013; 25 (39): 5638-42.

[39] Han Z. J., Tay B. K., Tan C. M. *et al.* **Electrowetting control of cassie-to-wenzel transitions in superhydrophobic carbon nanotube-based nanocomposites**. *ACS Nano*. 2009; 3 (10): 3031-6.

[40] Lespade P., Aljishi R., Dresselhaus M. S. **Model for Raman-Scattering from Incompletely Graphitized Carbons**. *Carbon*. 1982; 20 (5): 427-31.

[41] Wang Y., Alsmeyer D. C., McCreery R. L. **Raman spectroscopy of carbon materials: structural basis of observed spectra**. *Chemistry of Materials*. 1990; 2 (5): 557-63.

[42] Cuesta A., Dhamelincourt P., Laureyns J. *et al.* **Comparative performance of X-ray diffraction and Raman microprobe techniques for the study of carbon materials**. *J. Mater. Chem.* 1998; 8 (12): 2875-9.

[43] Wilhelm H., Lelaurain M., McRae E., Humbert B. **Raman spectroscopic studies on well-defined carbonaceous materials of strong two-dimensional character**. *J. Appl. Phys.* 1998; 84 (12): 6552-8.

[44] Niyogi S., Bekyarova E., Itkis M. E. *et al.* **Spectroscopy of Covalently Functionalized Graphene**. *Nano Lett.* 2010; 10 (10): 4061-6.

[45] Eckmann A., Felten A., Mishchenko A. *et al.* **Probing the Nature of Defects in Graphene by Raman Spectroscopy**. *Nano Lett.* 2012; 12 (8): 3925-30.

[46] Yick S., Han Z. J., Ostrikov K. **Atmospheric microplasma-functionalized 3D microfluidic strips within dense carbon nanotube arrays confine Au nanodots for SERS sensing**. *Chem. Commun.* 2013; 49 (28): 2861-3.

[47] Seo D. H., Han Z. J., Kumar S., Ostrikov K. K. **Structure-Controlled, Vertical Graphene-Based, Binder-Free Electrodes from Plasma-Reformed Butter Enhance Supercapacitor Performance**. *Adv. Energy Mater.* 2013; 3 (10): 1316-23.

[48] Fan Z., Yan J., Zhi L. *et al.* **A Three-Dimensional Carbon Nanotube/Graphene Sandwich and Its Application as Electrode in Supercapacitors**. *Adv. Mater.* 2010; 22 (33): 3723-8.

[49] Rajeswari J., Kishore P. S., Viswanathan B., Varadarajan T. K. **One-dimensional MoO2 nanorods for supercapacitor applications**. *Electrochem. Comm.* 2009; 11 (3): 572-5.

[50] Saji V. S., Lee C.-W. **Reversible Redox Transition and Pseudocapacitance of Molybdenum/Surface Molybdenum Oxides**. *J. Electrochem. Soc.* 2013; 160 (1): H54-H61.

[51] Kim Y. K., Cha S. I., Hong S. H. **Nanoporous cobalt foam and a Co/Co(OH)$_2$ core-shell structure for electrochemical applications**. *J. Mater. Chem. A*. 2013; 1 (34): 9802-8.

[52] Mazloumi M., Shadmehr S., Rangom Y. *et al.* **Fabrication of three-dimensional carbon nanotube and metal oxide hybrid mesoporous architectures**. *ACS Nano*. 2013; 7 (5): 4281-8.

[53] Yick S., Han Z. J., Ostrikov K. **Control of density of self-organized carbon nanotube arrays by catalyst pretreatment through plasma immersion ion implantation**. *J. Appl. Phys.* 2011; 110 (9): 094303-6.

[54] Tsang S. C., Chen Y. K., Harris P. J. F., Green M. L. H. **A simple chemical method of opening and filling carbon nanotubes**. *Nature*. 1994; 372 (6502): 159-62.

[55] Taberna P. L., Simon P., Fauvarque J. F. **Electrochemical characteristics and impedance spectroscopy studies of carbon-carbon supercapacitors**. *J. Electrochem. Soc.* 2003; 150 (3): A292-A300.

[56] Chen J., Sheng K., Luo P. *et al.* **Graphene hydrogels deposited in nickel foams for high-rate electrochemical capacitors**. *Adv. Mater.* 2012; 24 (33): 4569-73.

[57] Mhamane D., Suryawanshi A., Unni S. M. *et al.* **Hierarchically Nanoperforated Graphene as a High Performance Electrode Material for Ultracapacitors**. *Small*. 2013; 9 (16): 2801-9.

[58] Aurbach D., Levi M. D., Levi E. *et al.* **Common electroanalytical behavior of Li intercalation processes into graphite and transition metal oxides**. *J. Electrochem. Soc.* 1998; 145 (9): 3024-34.

[59] Zhang H., Cao G., Yang Y. **Carbon nanotube arrays and their composites for electrochemical capacitors and lithium-ion batteries**. *Energy Environ. Sci.* 2009; 2 (9): 932-43.

[60] An K. H., Kim W. S., Park Y. S. *et al.* **Electrochemical Properties of High-Power Supercapacitors Using Single-Walled Carbon Nanotube Electrodes**. *Adv. Funct. Mater.* 2001; 11 (5): 387-92.

[61] Zhang L. L., Zhou R., Zhao X. S. **Graphene-based materials as supercapacitor electrodes**. *J. Mater. Chem.* 2010; 20 (29): 5983-92.

[62] Yan J., Liu J., Fan Z. *et al.* **High-performance supercapacitor electrodes based on highly corrugated graphene sheets**. *Carbon*. 2012; 50 (6): 2179-88.

[63] Qie L., Chen W., Xu H. *et al.* **Synthesis of functionalized 3D hierarchical porous carbon for high-performance supercapacitors**. *Energy Environ. Sci.* 2013; 6 (8): 2497-504.

[64] Zhang L., Zhang F., Yang X. *et al.* **Porous 3D graphene-based bulk materials with exceptional high surface area and excellent conductivity for supercapacitors**. *Sci. Rep.* 2013; 3: 1408.

[65] Lee J. H., Park N., Kim B. G. *et al.* **Restacking-inhibited 3D reduced graphene oxide for high performance supercapacitor electrodes**. *ACS Nano*. 2013; 7 (10): 9366-74.

[66] Stoller M. D., Ruoff R. S. **Best practice methods for determining an electrode material's performance for ultracapacitors**. *Energy Environ. Sci.* 2010; 3 (9): 1294-301.

[67] Yu D. S., Dai L. M. **Self-Assembled Graphene/Carbon Nanotube Hybrid Films for Supercapacitors**. *J Phys Chem Lett*. 2010; 1 (2): 467-70.

[68] Yan Z., Ma L., Zhu Y. *et al.* **Three-dimensional metal-graphene-nanotube multifunctional hybrid materials**. *ACS Nano*. 2013; 7: 58.

[69] Fan Z., Yan J., Zhi L. *et al.* **A Three-Dimensional Carbon Nanotube/Graphene Sandwich and Its Application as Electrode in Supercapacitors**. *Adv. Mater.* 2010; 22: 3723.

[70] Yu D., Dai L. **Self-Assembled Graphene/Carbon Nanotube Hybrid Films for Supercapacitors**. *J. Phys. Chem. Lett.* 2010; 1: 467.

[71] Aboutalebi S. H., Chidembo A. T., Salari M. *et al.* **Comparison of GO, GO/MWCNTs composite and MWCNTs as potential electrode materials for supercapacitors**. *Energy Environ. Sci.* 2009; 4: 1855.

[72] Hiraoka T., Izadi-Najafabadi A., Yamada T. *et al.* **Compact and Light Supercapacitor Electrodes from a Surface-Only Solid by Opened Carbon Nanotubes with 2 200 m^2 g^{-1} Surface Area**. *Adv. Funct. Mater.* 2010; 20 (3): 422-8.

[73] Han Z. J., Levchenko I., Yick S., Ostrikov K. **3-Orders-of-magnitude density control of single-walled carbon nanotube networks by maximizing catalyst activation and dosing carbon supply**. *Nanoscale*. 2011; 3 (11): 4848-53.

[74] Chung H.-Y., Weinberger M. B., Levine J. B. *et al.* **Synthesis of ultra-incompressible superhard rhenium diboride at ambient pressure**. *Science*. 2007; 316 (5823): 436-9.

[75] Ago H., Uehara N., Yoshihara N. *et al.* **Gas analysis of the CVD process for high yield growth of carbon nanotubes over metal-supported catalysts**. *Carbon*. 2006; 44 (14): 2912-8.

[76] Hata K., Futaba D. N., Mizuno K. *et al.* **Water-assisted highly efficient synthesis of impurity-free single-walled carbon nanotubes**. *Science*. 2004; 306 (5700): 1362-4.

[77] Han Z. J., Ostrikov K. **Uniform, Dense Arrays of Vertically Aligned, Large-Diameter Single-Walled Carbon Nanotubes**. *J. Am. Chem. Soc.* 2012; 134 (13): 6018-24.

Bacterial Interactions of Carbon Nanotube Arrays

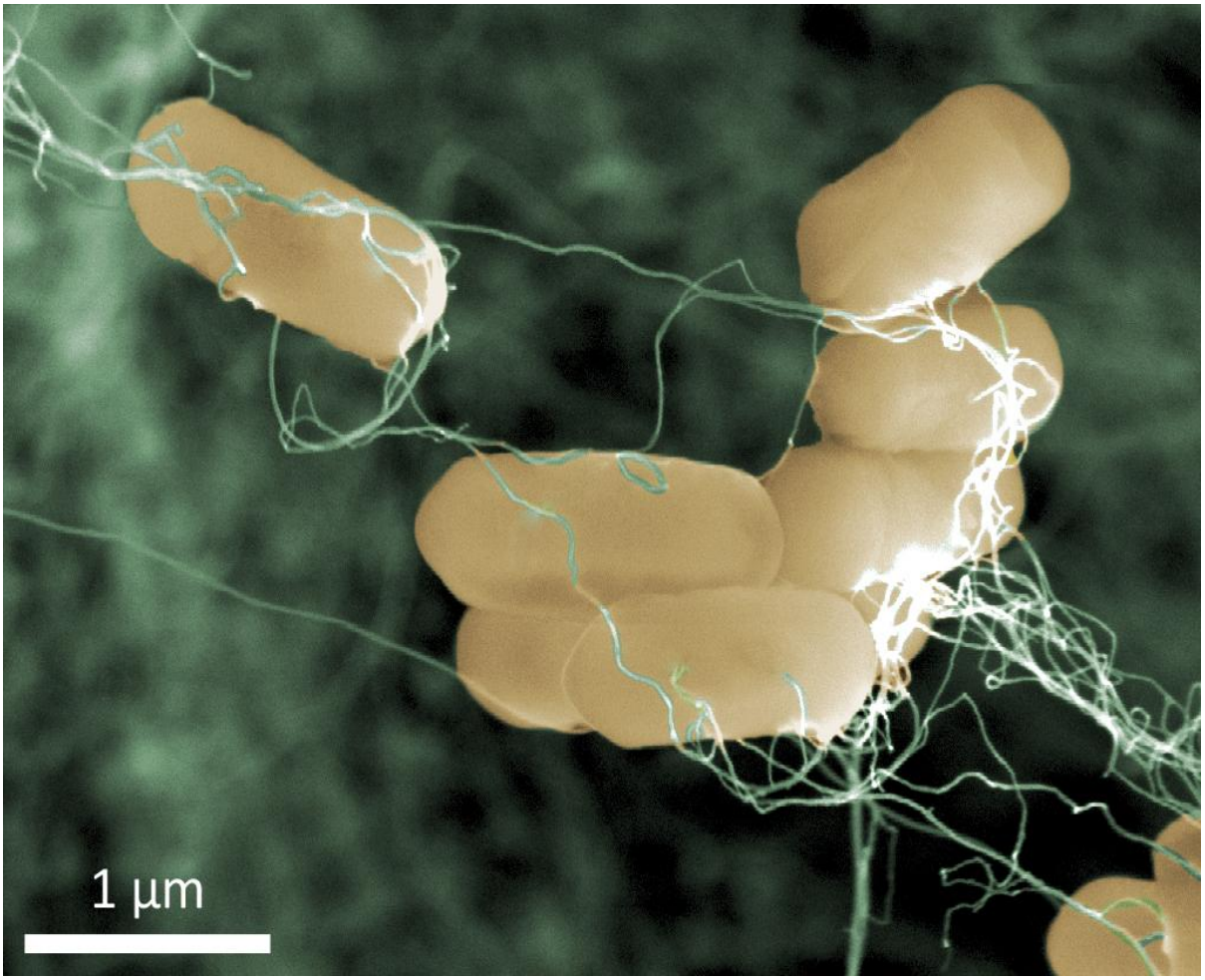

Micrograph indicating the physical interaction between *Bacillus subtilise* and strands of CNTs. The sample was prepared by CPD and observed under an SEM.

Chapter Summary

CNT possesses many attributes desirable for a range of health and biological applications. In particular, as discussed in Chapter 1, their ability to conjugate with various biomolecules can generate hybrid materials with novel and biologically relevant properties. However, the potential of CNTs in biological devices has yet to be exploited as our understanding of their biological interaction and cytotoxicity remains unclear. The reason for this ambiguity comes from the non-standardised nature of experimentally available CNTs. The variation in their morphology, graphitic quality and the presences of foreign components (metallic elements or chemical functional groups) can lead to contradictory toxicological results. Thus, the fundamental mechanisms which dictate the intrinsic interaction between CNTs and biological systems remain to be explored. In this chapter, the biological interactions of CNT arrays are studied through both a Gram-positive and Gram-negative bacteria model. From the in-depth chemical and biological analysis, the correlation between the microstructure, chemical functionalisation and their resulting biocompatibility were examined.

6.1 Biological Interactions of CNTs

Over the years, progress made in medical and biological technologies has improved both the life expectancy and standard of living for many. The emergence of nanoscience is predicted to lead to new developments of these fields, as novel nanomaterials allow direct interaction with molecules and substances relevant to biological systems. Due to their unique nature, CNTs can be beneficial to many bio- and health-related applications. There are various areas where the unique properties of CNTs can be promising. The mechanical properties of CNTs make them desirable in tissue engineering.[1] They can be used in drug delivery as their large specific surface area and chemical composition allow the formation of bioconjugate through binding with proteins, peptides and antibodies.[2] Lastly, their nanometre diameter and one dimensional morphology makes them useful and in intracellular probing and molecular delivery.[3,4]

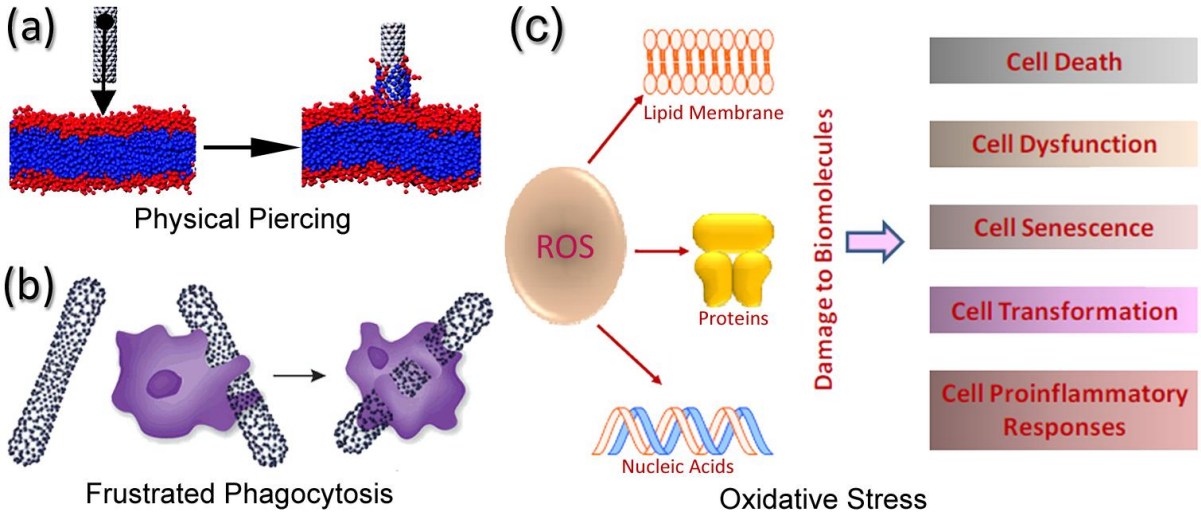

Figure 6.1 *Illustration of the various scheme involved in explaining the cytotoxicity of CNTs, (a) physical piercing,*[5] *(b) frustrated phagocytosis,*[6] *and (c) effects of oxidative stress.*[7]

Since their discovery, the toxicity of CNTs had been actively investigated with both mammalian cells and bacteria.[8] Most of these works indicate that CNTs are cytotoxic. Currently the toxicity of CNTs is attributed to the following mechanisms: physical degradation of cell membranes, disruption to the cellular activities and generation of fatal oxidative stress (Figure 6.1).[8] Physical interaction with solution dispersed CNTs had been shown to compromise the lipid bilayer of cells (Figure 6.1a). Using a bacteria model, Liu *et. al.* demonstrated that CNTs can cause the destruction of the plasma membrane via physical puncture.[9] With the help from numerical simulations, it has been speculated that as the tube penetrates the plasma membrane, elements of the lipid bilayer are extracted due to hydrophobic attraction between the non-polar chains and the graphitic surface.[5] Therefore, repeated puncturing by CNTs will degrade the membrane and kill the cell. Apart from physical interaction, the cellular uptake of CNTs has also been shown to elicit adverse cellular reactions. CNTs with large aspect ratios can lead to frustrated phagocytosis (Figure 6.1b).[10] This occurs when a cell tries to engulf a structure which is too long to be completely internalised by endosomes.[11] As such, the incomplete ingestion can lead to inflammatory responses and malignancy.[6] Upon shortening the length of CNTs, cells have demonstrated the ability to internalise them. However, their presences in the cytoplasma can elicit a genotoxic and undesirable response as they causes deactivation of proteins and organelles via physical binding.[8,12,13] Lastly, CNTs have been known to

generate reactive oxygen species (ROS). The exposure to ROS can lead to fatal oxidative stress (Figure 6.1c). ROS are produced upon uptake either by the CNTs themselves or from the metallic catalyst residuals (such as Fe, Ni and Co).[14] Once the ROS enter the cells, they are known to target cellular constituents such as lipids, proteins, nucleic acids and carbohydrate. Thus, exposure to ROS can result in chromosomal damage, premature ageing of the cell (cell senescence), inflammotary response and cell apoptosis.[15,16].

From the commonly accepted mechanisms presented above, the toxicity of CNTs can be reasoned to the following properties: high aspect ratio, wall rigidity, ability to generate free radicals and biopersistency. Due to these attributes, interaction or uptake of CNTs can lead to adverse cellular response and cell death.[9,17] However, the lethality of these interactions depends on the ability individualised CNTs to interact with the cells. For this reason, there is a further correlation between the toxicity of CNTs and the stability of the CNT dispersion. It is often noted that upon agglomeration, the toxicity of CNTs decrease significantly. [18,19]

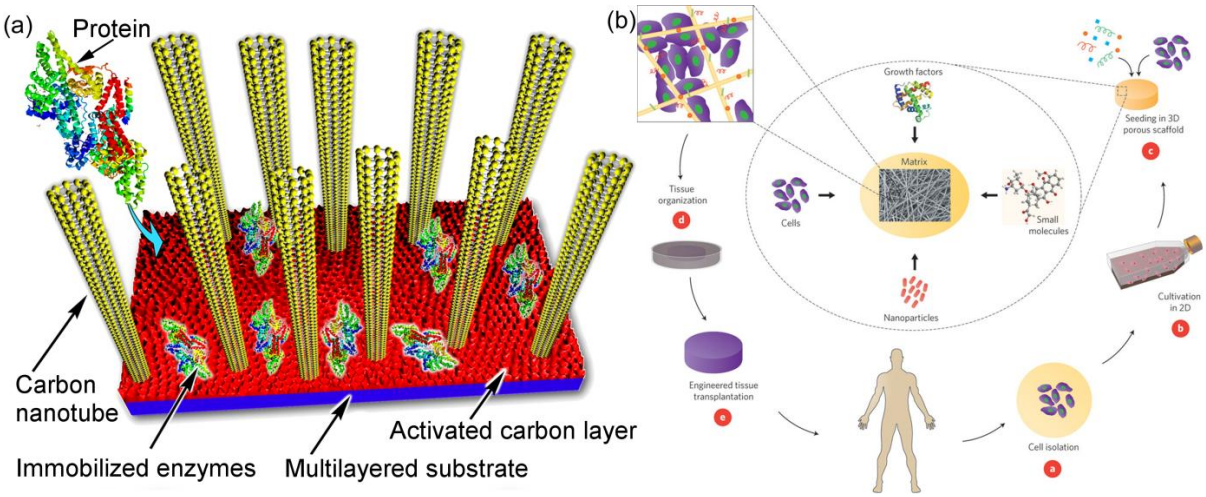

Figure 6.2 *(a) An illustration of proteins coupled with CNT arrays for bioreactor applications.*[20] *(b) Schematic about the application of CNT arrays and other 3D nanomaterials for tissue engineering.*[1]

Despite the general association between nanotoxicity and individual CNTs, CNT arrays may show different biological properties due to their ordered microstructure. CNT arrays are surface bound unlike the individualised CNTs commonly used in toxicological studies. Their adhesion to the

substrate invalidates the dispersion based mechanisms previously mentioned. Thus, CNTs arrays might possess different cellular interactions.

Furthermore, it had been recently shown that CNT arrays can exhibit effective coupling with proteins. By embedding enzymes into the array's architecture, their bioactivity can be prolonged as they are protected from the external environment. Such work alluded to the usefulness of CNT arrays for flow bioreactor applications, which currently suffers from enzyme depletion and inactivation.[20] Additionally, CNT arrays can be engineered which enable the rate of release of the embedded proteins to be tuned.[21] This is a desirable property suitable for advance drug delivery platform and scaffolds for tissue growth. Yet, despite the copious toxicological studies published about CNTs recently, information regarding to the cytotoxicity of CNT arrays remains limited. It is thus of great interest to study the biocompatibility of CNT arrays.

In this work, the biocompatibility of CNT arrays is examined via the bacteria models. Specifically, the effects of CNT arrays with varying degrees of surface functionalisation on the bacteria's proliferation, membrane integrity, and bioactivities are investigated. The work presented in this chapter may shed light on the future biological applications of CNT arrays.

6.2 Methodology

Growth of CNT arrays. The growth process of CNT arrays here is identical to that described in Chapters 3 and 4.

Plasma Modification of CNT arrays. The as-grown CNT arrays were treated with Ar plasmas generated via an Inductively-Coupled Plasma (ICP) system. Briefly, the sample was first inserted into a vacuum chamber. 20 sccm of Ar was flowed into the chamber and the pressure was set to 5 Pa. The sample was treated by argon plasmas ignited at power ranging from 200 to 1000 W for 2 minutes.

Bacteria Experiment. Bacillus subtilis (*B. subtilis)* and *Escherichia coli* (*E. coli*) were grown overnight in Luria Bertani (LB) broth at 37°C to an optical density of 1. A 5 µL aliquot of overnight culture was inoculated into 1 mL of fresh LB broth in a well of a 24-well plate; each well also contained a 1 cm^2 piece of CNT array sample. The 24-well plate was incubated for 16 hours at 37°C with slight shaking (80 rpm). To determine the viability of the bacteria, aliquots from the incubated wells were taken for live cell counts to determine the number of colony forming units (CFU).

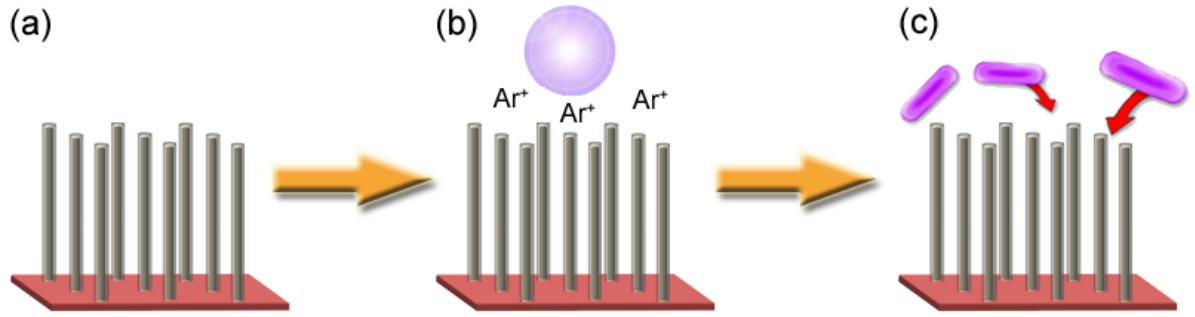

Figure 6.3 *Schematic of the experimental process, firstly the thermally grown CNT arrays (a) were treated with an argon based ICP (b), and incubated with a solution of bacteria and growth medium for 24 hours (c).*

Flow Cytometry. Bacteria from both the supernatant and the biofilms formed on the nanostructures were used in the flow cytometry measurements. Bacterial biofilms were scraped off from the CNT arrays using a sterile metal spatula and dispersed into 2 mL of phosphate buffered saline (PBS). Samples were sonicated for 1 min to break up cell clumps before staining with LIVE/DEAD® BacLight™ (Invitrogen) according to the manufacturer's instructions. A 6-hour fresh culture of each strain was diluted into PBS. One half of this culture was used as a live control and stained with each of the components (Syto 9 and PI) separately. The other half was heat killed by exposing the culture to 90°C for 10 min in a water bath before staining.

Preparing Biological Samples for SEM. In order to enable the utilisation of electron microscopic analysis, the bacteria laden samples were prepared with the critical point drying (CPD). The samples were first immersed in 100% ethanol, then transferred to the CPD chamber (BAL-TEC CPD030 Critical Point Dryer) and dried using liquid CO_2 for 3 hours at the critical point (+31.1°C, 1000 PSI). This

process allows the structural integrity of both the bacteria and CNT arrays to be preserved in a high vacuum environment.

Material Characterisation. Field-emission scanning electron microscopy (FE-SEM; Zeiss Auriga) operated at an electron acceleration voltage of 5 kV and a working distance of 2.6 mm. Transmission electron microscopy (TEM; JOEL 2200) was operated at an electron beam energy of 200 keV. X-ray photoelectron spectroscopy (XPS) measurements were taken using the PHI Specs Sage 150 system, where the Mg Kα (at 1253.6 eV) line was used as the excitation source. The Raman spectra were collected by Renishaw *InVia* confocal Raman microscope system with a 50× objective lens. Samples were excited with a 514 nm laser at power of ~ 1.5 mW and a spot diameter of ~ 1 μm^2.

6.3 Results and Discussion

6.3.1. Effects of Plasma Treatment on the CNT Arrays

As mentioned in chapter 4, plasma treatment generates reactive sites on CNTs which can be functionalised upon being exposed to air. By varying the power used to generate the plasma, the degree of modification i.e., the surface energy, quantity of chemical functional groups, and the graphitic quality of the CNTs, can be controlled. These variations can affect the ability of a biological system to interact with CNTs. In order to understand the effect of plasma functionalisation on the CNT arrays' biocompatibility, it is prudent to first investigate the change induced by the plasma treatment. This is best illustrated by analysing the CNT arrays treated by Ar plasma of 1000 W and comparing these results with the pristine sample.

The morphology of the CNT arrays used in this study is shown in the SEM micrographs of Figure 6.4**.** The top of the array was comprised of entangled tubes with submicron voids (Figure 6.4a). Such voids proved to be impermeable to the bacteria due to their physical dimensions (Figure 6.4b). By examining the cross-sectional SEM micrographs depicted in Figures 6.4c and d, the CNT arrays

possessed an average height of 20 µm and an estimated density of 3 to 5×10^{10} tubes/cm^2. As mentioned in chapter 4, the height and density of CNT arrays remain unperturbed after plasma treatment.[22] As such, the chemical environment of the CNT arrays can be altered without disrupting the overall microstructure. This is a significant advantage possessed by plasma treatment over conventional functionalisation techniques which relies on wet chemical.

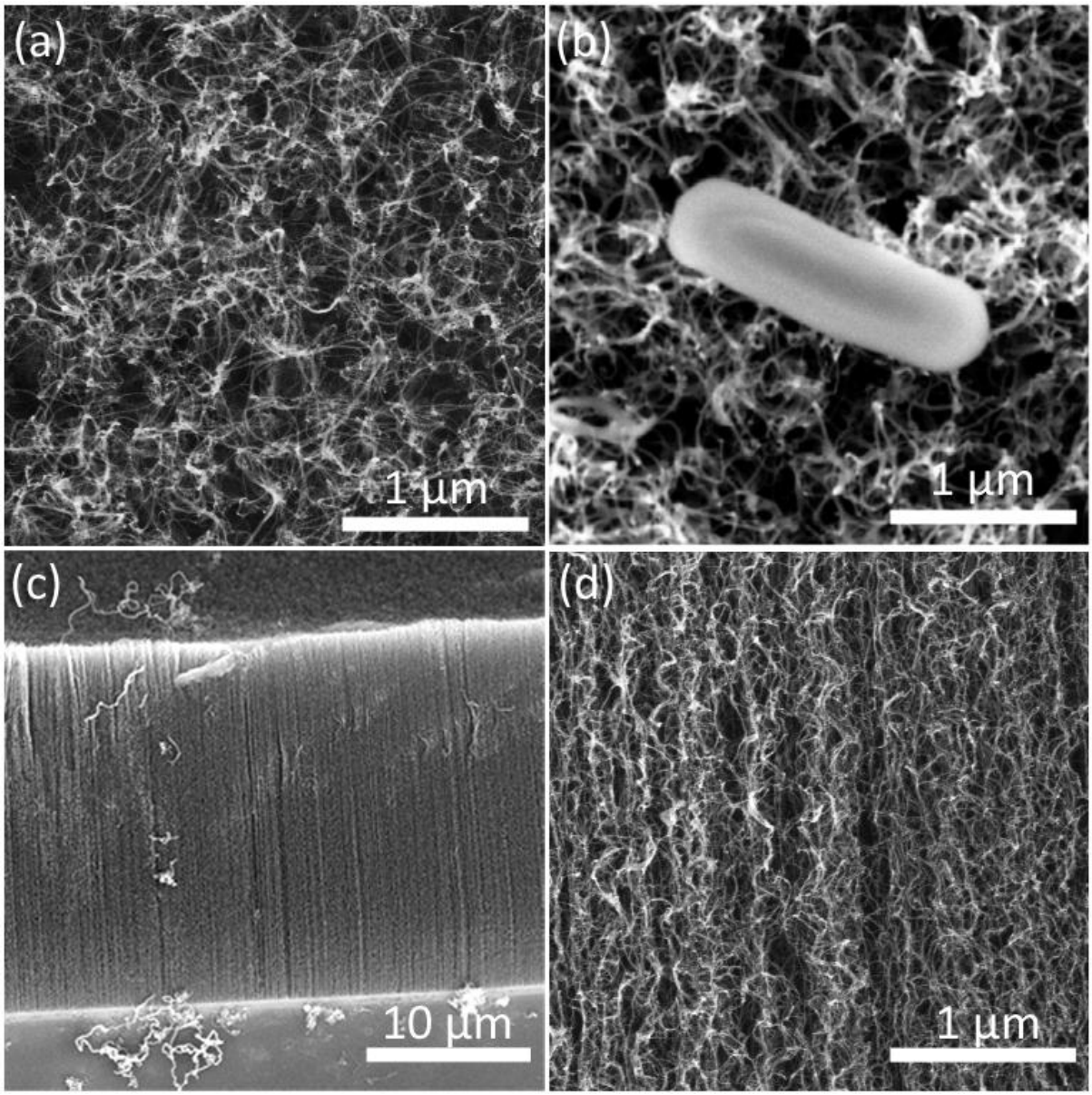

Figure 6.4 *SEM images of the as-prepared carbon nanotube arrays, the top view of the CNT arrays (a), in the presences of B. subtilis (b) resolution cross-sectional images of the arrays in low (c) and high (d) resolution.*

The plasma treatment enabled chemical modification of the CNT arrays through disrupting the graphitic structure of CNTs as observed in Figure 6.5. The pristine CNT was shown to possess a

diameter of 10 nm with 5 to 10 walls. The clearly distinguishable lattice fringes observed in the pristine sample indicate their high graphitic ordering (Figures 6.5a and b). After the plasma treatment at 1000 W, though the diameter of the tube remained unchanged, the lattice fringes and the internal void became unobservable (Figures 6.5c and d). Furthermore, some of the nanotubes appeared to be opened by the treatment. These observations confirm our assumptions that bombardment by Ar ions can alter the graphitic lattice of the CNTs.

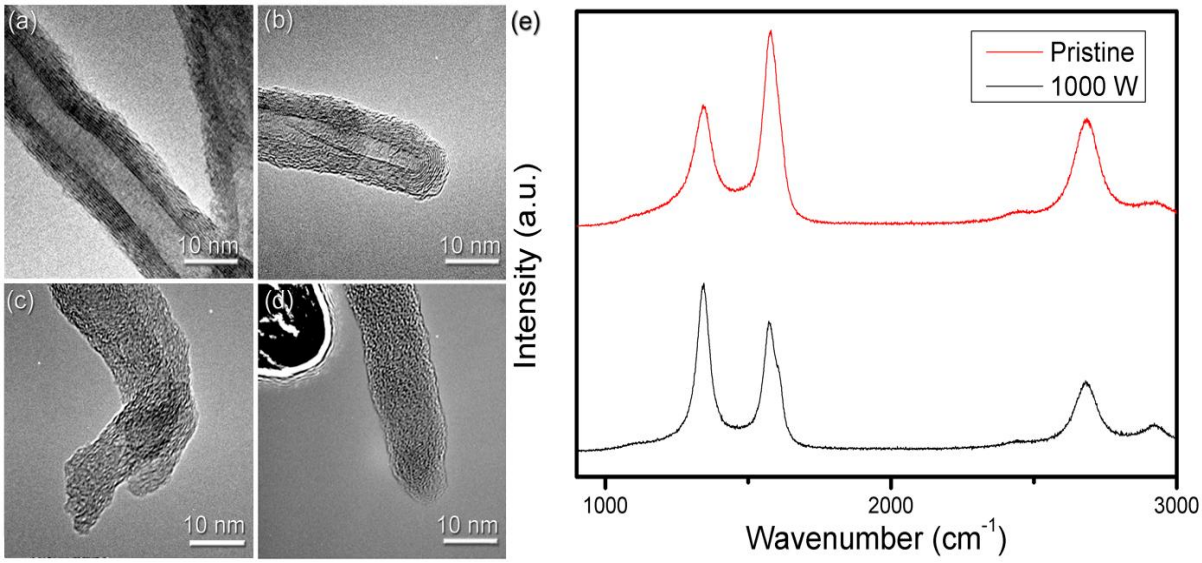

Figure 6.5 *High resolution TEMs of the (a), (b) pristine nanotubes and (c), (d) nanotubes after a 1000 W plasma treatment. Raman spectra (e) of the pristine and plasma treated CNT arrays.*

The changes induced to the graphitic structure were further examined via Raman spectroscopy. Raman spectra of both pristine and plasma functionalised samples are shown in Figure 6.5c. The spectra displayed features commonly associated with multi-walled CNTs, which include the D-peak at 1340 cm^{-1}, the G-peak at 1570 cm^{-1} and the second-order Raman resonant feature (2D-peak) at 2680 cm^{-1}. Even at a glance, the differences between the two spectra can be clearly observed. These include the change in the relative intensity of the D and G-peak, the reduction of the 2D-peak and the emergence of a shoulder feature at 1604 cm^{-1}. It is known that the ratio between the D- and G-peak (I_D/I_G) reflects the crystalline ordering of the nanostructure. In the present case, the I_D/I_G ratios of the CNT arrays increased from 0.65 to 1.26 after plasma treatment. The increase in I_D/I_G ratio implied an increase in sp^3 content, due to a higher amount of graphitic disordering. The change in

I_D/I_G ratio was also accompanied by a reduction in the intensity of the 2D peak. Such reduction can be attributed to the fact that plasma treatment caused a disruption to the graphitic structure of the CNTs. The plasma treatment also generated a shoulder featured at Raman shift of 1604 cm^{-1}. This feature, commonly referred to as the D' peak, is a defect induced single-phonon intra-valley scattering process.[23] The origin of this feature have been shown to arise from perturbations within the sp^2 lattice induced by the presences of voids and edge defects.[24] Therefore, the emergence of the D' feature indicates that the Ar plasma treatment may have created voids in the graphitic networks and edge defects through opening the tubes. These Raman and TEM results confirmed that plasma treatment created reactive sites without changing the microstructure of the CNT arrays. It was noted that the presences of defective sites allow the CNT arrays to be functionlised with oxygen-containing surface groups once exposed to the atmosphere.

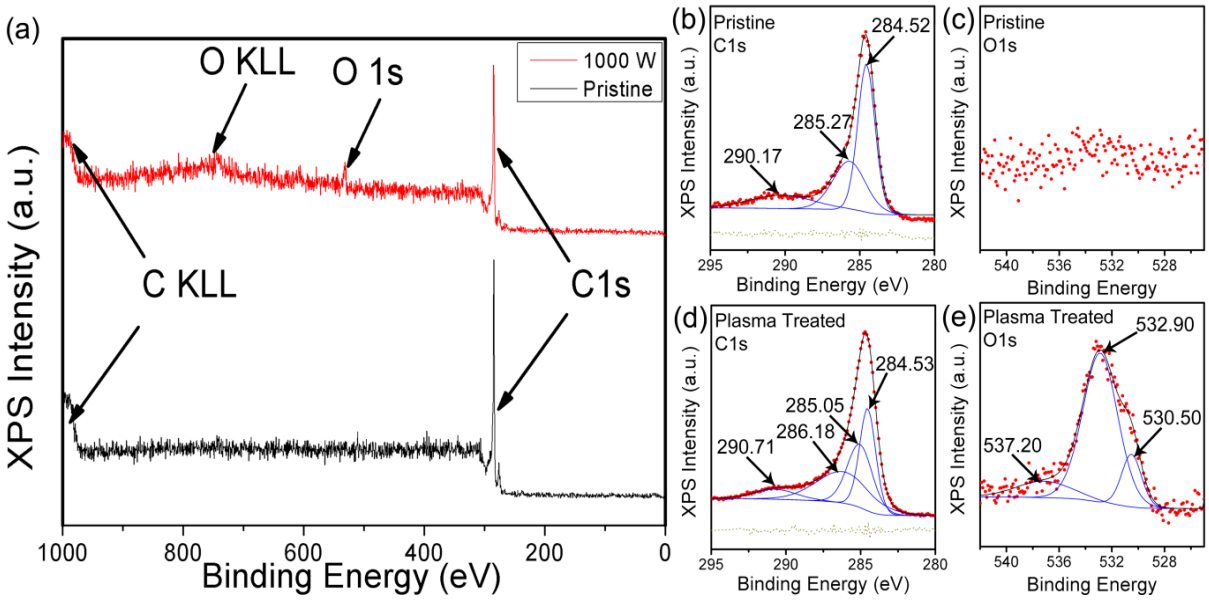

Figure 6.6 *(a) XPS spectra of the pristine and 1000 W plasma treated CNT arrays with the survey scan and narrow scans of the (b), (d) C1s and (c), (e) O1s plotted.*

The chemical bondings of the plasma-treated CNT arrays were also quantified by XPS. The survey scans of the two samples (Figure 6.6a) show that only peaks relating to carbon atoms were detected in the pristine sample; whereas in the plasma treated sample, extra peaks correlating to oxygen atoms were also present. Figures 6.6b to e present the high-resolution scans over the regions of 280 to 295 eV and 524 to 542 eV, which correspond to the binding energy (BE) of C1s and O1s features

respectively. These peaks were deconvolved to reveal the different chemical environment of the pristine and plasma treated CNT arrays. Within the pristine sample, three peaks at positions 284.52, 285.27 and 290.71 eV can be fitted under the C1s spectrum. These peaks corresponded to carbon atoms in the sp^2-bonding, sp^3-bonding and the shake-up features (Figure 6.6b).[22,25] After the plasma treatment process, peaks corresponding to carbon atoms in the sp^2- bonding (284.53 eV), the sp^3-bonding (285.05 eV) and the shake-up features (290.71 eV) still remained. However, it is cleared that the ratio of XPS peak intensity between the sp^2- and sp^3-bonded carbons (I_{sp2}/I_{sp3}) decreased. Furthermore, an additional peak at 286.18 eV could be fitted to the C1s feature of plasma treated CNT arrays (Figure 6.6d). This new peak arose from the carbon atoms binding with the oxygen containing moieties.[26]

Apart from the change to the C1s feature, the plasma treatment led to the emergence of an O1s feature (Figures 6.6c and e). After being exposed to the plasma, the oxygen atomic percentage of the CNT arrays increased from 1.2 at.% (close to the instrumental noise level) to 7 at.%. Upon deconvoluting the O1s feature, three peaks at positions 530.50, 532.90 and 537.20 eV were observed. These peaks corresponded to oxygen atoms which are physisorbed, the carboxyl or hydroxyl groups bonded to an aromatic structure, and the C-O groups, respectively.[27-29] The O1s features corresponded to the change in the C1s peak observed. This demonstrates that the plasma treatment was indeed able to modulate the surface functionality of the CNT arrays

6.3.2. Biological Interactions of the CNT Arrays

In order to elucidate the biological interactions of the CNT arrays and the effect of the plasma treatment, CNT arrays treated by different plasma powers were incubated with *B. subtilis* and *E. coli* in a growth medium. These bacteria were chosen due to the difference in their physiology and their wide usage in the routine laboratory experiments. The two groups, Gram-positive and Gram–negative bacteria, are differentiated by their outer cellular structure. Gram-positive bacteria such as *B. subtilis* have a thick cell wall composed of peptidoglycan. As a result, they are able to retain the

stain crystal violet and appear purple after the differential staining procedure. On the other hand, Gram-negative bacteria such as *E. coli* have a much thinner layer of peptidoglycan. They can be easily de-stained with ethanol and appear pink after counter staining with Safranin. Therefore, these different groups of bacteria represent the two sets of unique biological interfaces. It is also noted that although *E. coli* lacks a thick layer of peptidoglycan, it possesses an outer membrane in addition to the plasma membrane and cell wall. This feature allows *E. coli* to be intrinsically more resistant to some antibiotics and physical stress.[30]

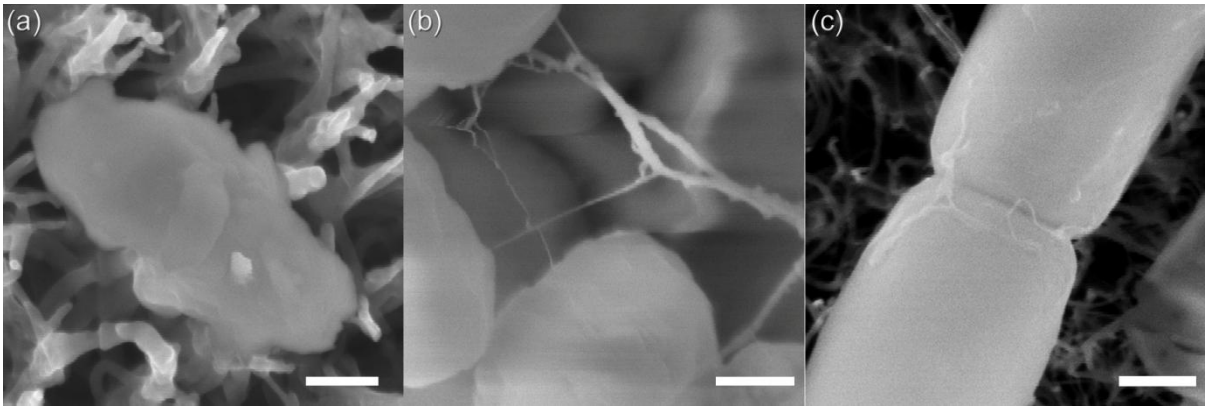

Figure 6.7 *SEM images of the bacteria on the CNT array, (a) CNT penetrating the bacteria, (b) the formation of filaments by the bacteria in the biofilm and (c) bacteria undergoing division. All scale bars represent 200 nm.*

The biocompatibility of a material can be studied by the microscopic imaging techniques. In order to prepare the surface for SEM imaging, the samples were treated via the CPD technique SEM offers a higher magnification as compared to the optical microscope and could enable the study of interactions between CNTs and the bacterial of interest. To illustrate the advantages of the SEM, Figure 6.7 showcased a host of cellular activity which are not observable by optical microscope. This includes the piecing of the plasma membrane by CNT (Figure 6.7a), the formation of extracellular filaments (Figure 6.7b) and cell division (Figure 6.7c). These observations shed light on the bacterial interaction of CNT arrays.

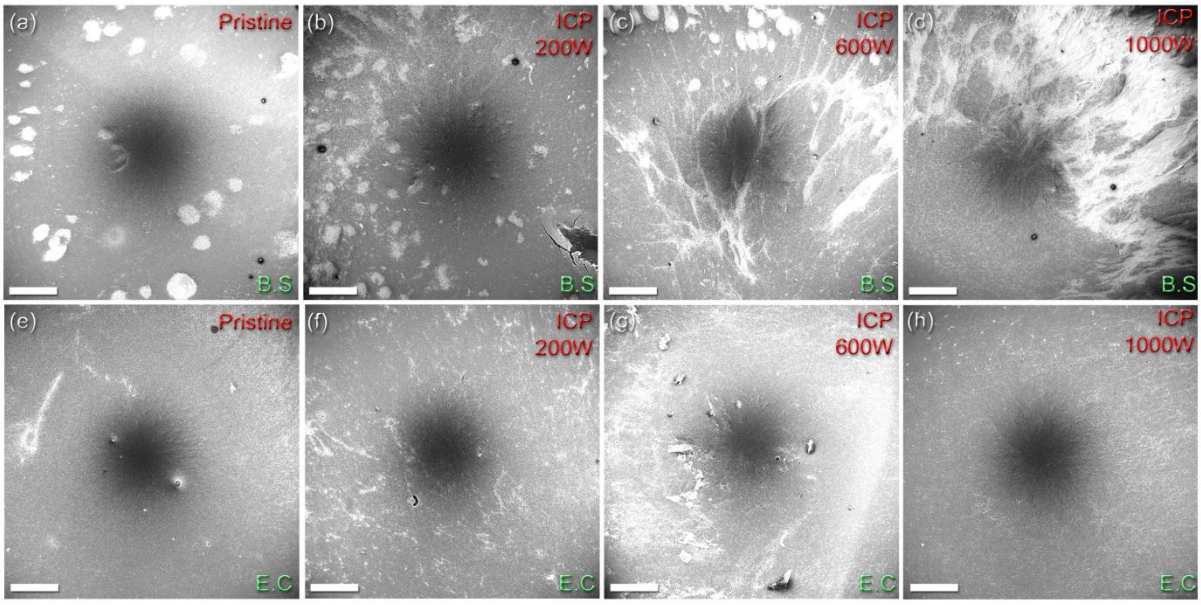

Figure 6.8 *SEM images of the bacteria colonies formed on the CNT arrays treated by plasma of different plasma. The top row depicts the colonies formed by B. subtilis whereas the bottom row represents the colonies formed by E. coli. All scale bars represent 400 µm.*

The SEM micrographs presented in Figure 6.8 depicted the colonies formed by both *B. subtilis* and *E. coli* on the surface of the CNT arrays with varying degrees of plasma modification. Upon the attachment to a suitable surface, bacteria are known to proliferate and form biofilms. Such structures can indicate the ability of the surface to capture live and active bacteria. From these micrographs, it is obvious that both bacteria were able to form colonies (white patches) on the CNT arrays. As seen in Figure 6.4b, the bacteria sit at the top of the CNT arrays and were not able to penetrate into the microstructure. In the case of *B. subtilis*, a correlation between the proliferations of the bacterium with the extent of the functionalisation process was observed. Prior to plasma treatment, *B. subtilis* was only able to form sparse micro-colonies on the surface of the CNT array after being incubated overnight. However, as the plasma power increased, the size, number and thickness of the bacterial microcolonies also increased in correspondence. At 1000 W (the highest ICP power generated in this experiment), thick biofilm streamers were observed (Figure 6.8d). *E. coli* also formed biofilms on the CNT arrays (Figure 6.8e-h). However, the plasma treatment did not drastically alter the size and number of the colonies. These observations may suggest that Gram positive and Gram negative bacteria perceive and respond to CNT arrays differently.

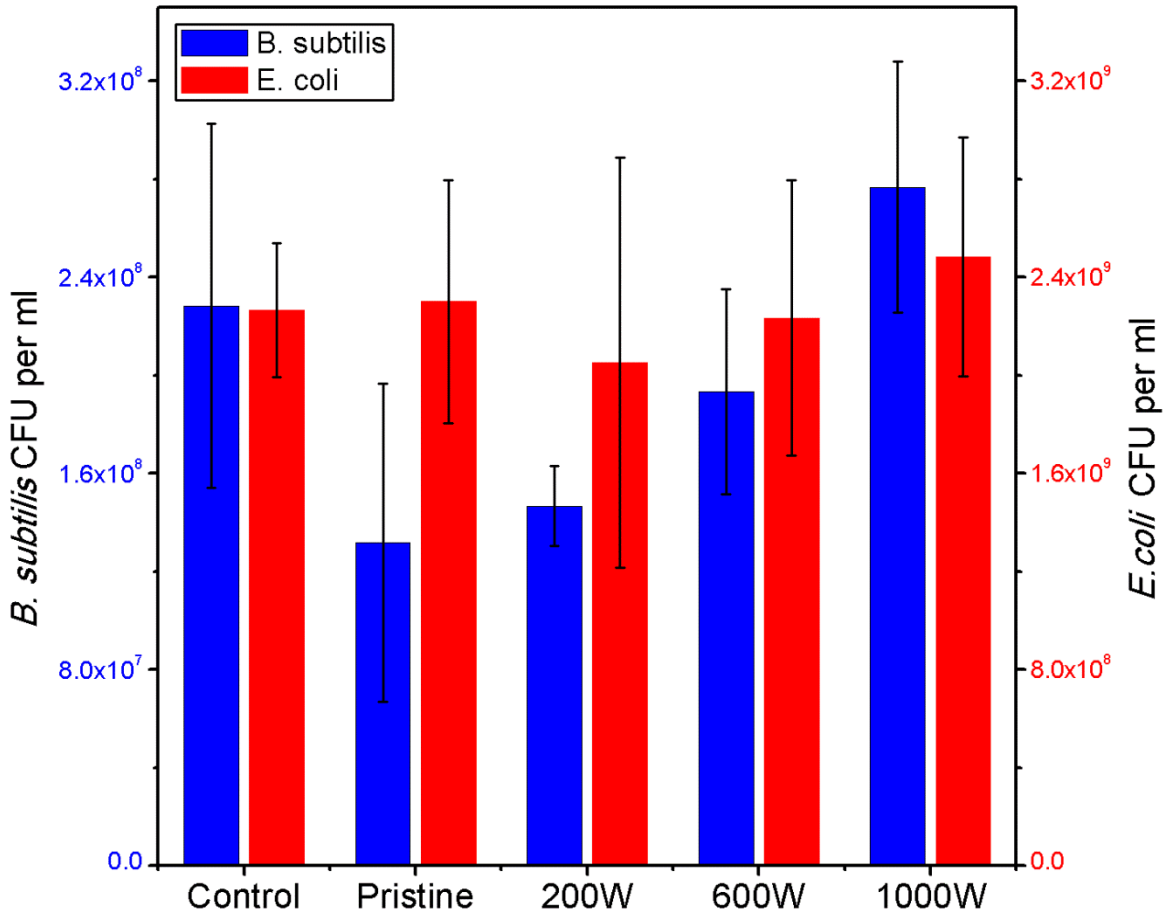

Figure 6.9 *The amount of viable bacteria was quantified using a colony counting method. The blue bars and the y-axis on the left correspond to B. subtilis, whereas the red bars and the y-axis on the right corresponds to E. coli. The control consisted of the bacteria being incubated in the absences of any CNT arrays.*

The biocompatibility of the CNT arrays was further investigated by quantifying the number of colony forming units (cfu) present in the supernatant (SN). This measures the number of viable bacteria within the medium and is sensitive to environmental factors. Therefore, cfu can indirectly reveal the biocompatibility of the different CNT arrays. In order to assess the samples, a control where the bacteria were incubated in the absences of any CNT arrays was also conducted. The cfu for both *B. subtilis* and *E. coli* are plotted as a function against the power used in the plasma treatment process in Figure 6.9.

For the control of *B. subtilis*, a density of 2.3×10^8 cfu/mL was observed. Once the bacteria were exposed to pristine CNT array, the density dropped to 1.3×10^8 cfu/mL. However, as the plasma treatment increased, a higher number of cfu was also observed. At the maximum treatment power

of 1000 W, the supernatant possessed a density of *B. subtilis* similar to the control ($2.8x10^8$ cfu/mL). Interestingly, this trend was not observed with *E. coli*. The density of the control samples reached $2.4x10^9$ cfu/mL after 24 h. However, no statistically significant change was observed when *E. coli* was incubated with either pristine or plasma functionalised CNT arrays ($2.4x10^9$ and $2.5x10^9$ cfu/mL, respectively). This corresponded well to the SEM results presented in Figure 6.8, where the *E. coli* colonies on both pristine and functionalized samples appeared similar but the colonies of *B. subtilis* were affected by the plasma treatment process.

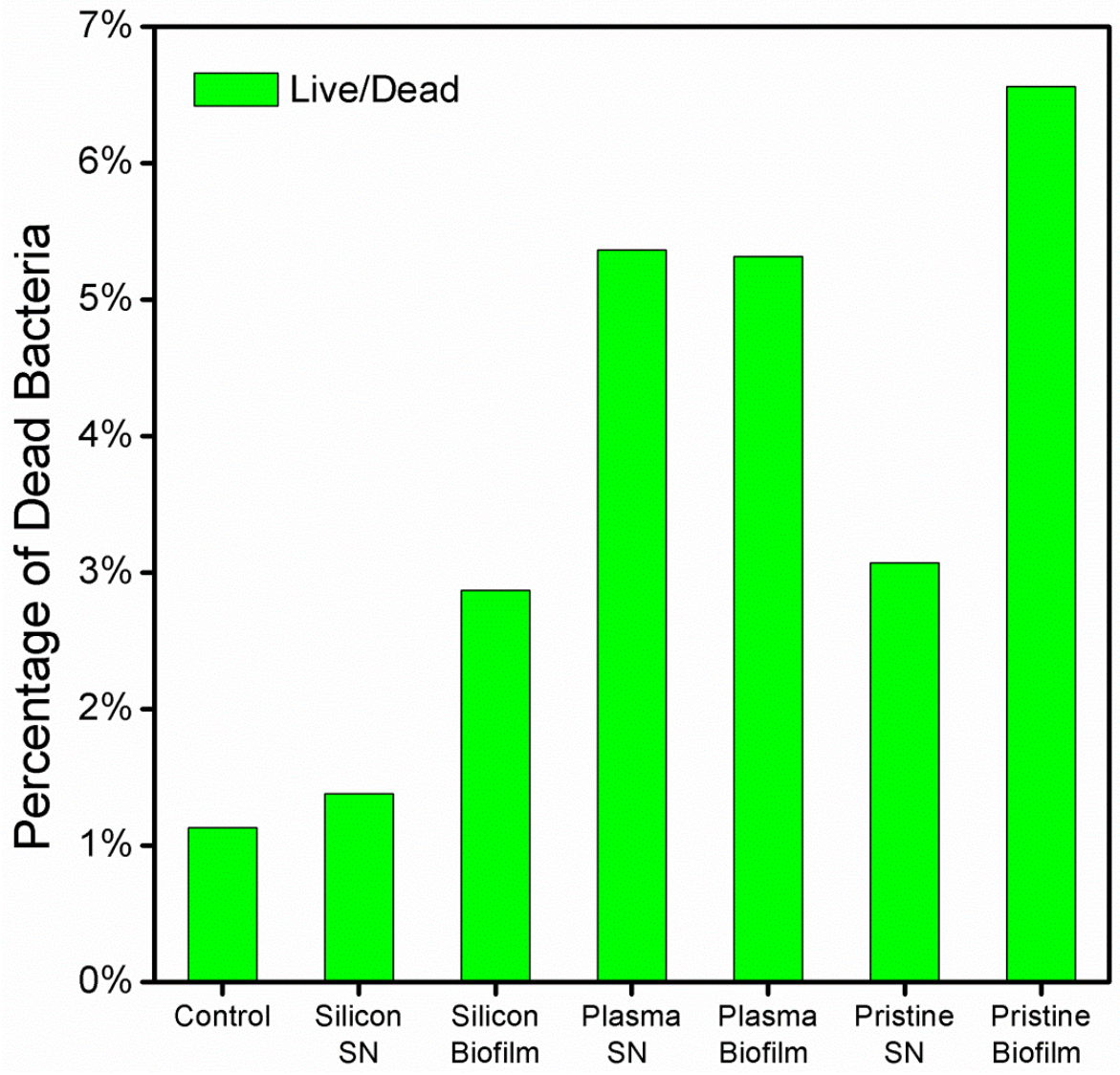

Figure 6.10 *The percentage of dead cells in the supernatant (SN) and biofilm of the B. Subtilise laded samples as established by flow cytometry. Those denoted as "Plasma" refer to CNT arrays treated at 1000 W.*

So far, the results indicated that CNTs are more active against the Gram-positive *B. subtilis* and the antibacterial effect reduces significantly with plasma functionalisation of the CNT arrays. To better

understand the interaction between the CNT arrays and *B. subtilis*, a fluorescent staining technique was used in conjunction with flow cytometry. LIVE/DEAD® BacLight™ (Invitrogen) staining uses the nucleic acid stain Syto 9 to stain the entire cell population green, and the red propidium iodide stain which counter stains cells which possess a compromised cell membrane (dead cells). This allows the bacteria to be sorted according to their viability.

Bacteria samples were obtained from the control, catalyst coated silicon wafer (Silicon), the supernatant (SN) and biofilm from the CNT arrays. As shown in Figure 6.10, there was an observable difference between the biofilms formed on the pristine and plasma treated CNT arrays. In the former, the biofilm showed a larger percentage of dead bacteria on the biofilm as compared to the SN; whereas in the latter, the same percentage of dead bacteria was found on the biofilm and the SN. Interestingly, the percentage of dead cells was less than 7 % in all cases. This is significantly less than what is normally observed in bacteria incubated with suspended CNTs or filtered through bucky paper (porous membranes comprised of CNTs).[19,31]

The results presented above demonstrate the biological effects of plasma treatment on the CNT arrays. Though the presences of the CNT arrays regardless of the plasma treatment did not seem to affect *E. coli*, the plasma treatment did reduce the antibacterial property of the CNT arrays towards *B. subtilis*. The observed results are in contrast to the common toxicological knowledge of CNTs. In general, CNTs have been shown to be cytotoxic and the lethality would increase with functionalisation.[32] To explain the observed results, it is prudent to consider the relevancy of the cytotoxic mechanisms discussed in section 6.1 to CNT arrays.

Previously it was reported that there are primarily three mechanisms which contribute to the cytotoxicity of CNTs. These include frustrated phagocytosis, oxidative stress, and physical piercing. In this study, the occurrence of frustrated phagocytosis is impossible as there were no phagocytes in our samples.

Fatal Oxidative stress was also unlikely as a correlation between the extent of functionalisation and ROS was lacking. This could be seen in Figure 6.9 that as the plasma treatment became more extensive; the biocompatibility of the treated CNT arrays either increased or remained the same. This was striking, as it was a commonly held belief that functionalized CNTs were more capable in ROS generation.[33] However, prior studies have demonstrate CNT are able to quench and scavenge free radicals.[34] Perhaps as the CNTs became more reactive, they were more capable in neutralising ROS. Such mechanism if proven could indeed support the observation that increasing functionalisation resulted in a higher biocompability.

Apart from the CNTs, catalyst particles were also associated with the generation of ROS. Yet, the experimental results presented in Figure 6.10 casted doubt on this assumption. Although the bacteria was incubated on the catalyst coated substrate, the exposure seem inconsequential to the bacteria's survival. This seemingly contradictory observation regarding the toxicity of metallic residue can be explainable by their location. In publications which spoke of the ROS generating ability of metallic residues, they are often located in the intracellular space.[35] Therefore, it is highly likely that their exclusion of the catalyst residues from the intracellular space led to their passivity.

Lastly, the physical interaction between the bacteria and the CNT arrays may provide a plausible explanation to the observed trend. *E. coli* was seen to be much less affected by the CNT arrays as compared to *B. subtilis* (Figure 6.9). This difference may be attributed to the presences of an outer membrane in *E. coli* (Gram negative) that enables a higher resilience to the CNT arrays as compared to *B. subtilis* which lacks such cellular structure.[30,36] Recently, Tu *et. al.* showed that oxygen-functionalised graphene sheets were less capable in degrading the lipid membrane of bacteria as compared to pristine structure.[37] They explained the difference by reasoning that graphitic surface after oxygenation becomes more hydrophobic. Therefore, they are less capable in extract the hydrophobic lipid membrane. Similarly, one could assume a similar mechanism to be present in the interaction between CNT arrays and *B. subtilis* where the physical interactions with functionalised

CNTs were less damaging. Thus, by chemically fucntionalising the CNT arrays (i.e. decreasing their hydrophobicity); they are less able to degrade cell viability. Hence, the biocompatibility of CNT arrays can be enhanced by surface functionalisation.

Yet, the effects of physical piercing and membrane degradation remain ambiguous as only a relatively small number of bacteria (<7 %) exposed to the CNT arrays possessed a compromised membrane (Figure 6.10). This small population stand in contrast to what is commonly observed when bacteria and cells are exposed to CNT suspensions. The differences could perhaps be understood by the mobility exhibited by CNT in suspensions verse CNT within an array. When CNTs are dispersed in a medium, they possess momentum and kinetic energy which allows them to pierce cells.[9] However, upon being fixed to a substrate such mobility is lost, this can significantly mitigate the effectiveness of the physical puncturing mechanism.

What about the antibacterial properties of fixed CNT structures such as bucky paper? There are many publications which attribute their toxicity to piercing mechanism.[31,36] However at this point, it is worth remembering that in these experiments an osmotic pressure created as the solution flows through the membrane. Thus, though the CNT remained fixed the bacteria are pressed against these structures, which results in their penetration and lysis.

In fact, the biocompatibility seen in this work confirms the penetrative ability of CNT is a passive rather than an active mechanism. Indeed, CNT arrays can be thought of as a “bed of nails”, where despite the sharp tips, in the absence of force the bacteria can reside on the surface without being pierced.

Therefore, by examining the interaction between the two groups of bacteria and CNT arrays, it can be seen that the toxicity of CNTs are based on their passive mechanism. Therefore the common perceptions that CNTs are intrinsically cytotoxic due to their high aspect ratio and that chemical functionalisation will make them more lethal need to be reconsidered. Indeed, though CNTs with

high aspect ratio can display enhanced penetrative potential; such property is only relevant if the tube can form a stable dispersion in the medium.[19] As to the correlation between chemical functionalisation and toxicity, this is more likely due to the enhanced dispersibility of CNTs and/or the shortening of the CNTs caused by the treatment.[32,38] These features which facilitate interaction between CNTs with cellular organisms are what lead to adverse cellular response, rather than simply due to the presence of chemical moieties.

6.4 Chapter Conclusion

In summary, the interaction of CNT arrays with bacteria has been presented in this work. Through plasma treatment, the chemical properties of CNTs were altered and their biological relevance were investigated. The work presented demonstrates that the commonly attributed toxicity of CNTs was in fact based on multiple factors rather than just being an intrinsic nature of CNTs. In fact, it seems that the adverse cellular interaction caused by CNTs can be minimised by fixing CNTs onto a substrate. This enables CNTs and CNT-based nanomaterials to be employed in a variety of biological applications. Furthermore, the work shows that the process of functionalisation does not necessarily enhance the toxicity of CNTs. This opens up new avenues for the formation of CNT/biomolecule hybrids with specific properties for novel applications.

6.5 References

[1] Dvir T., Timko B. P., Kohane D. S., Langer R. **Nanotechnological strategies for engineering complex tissues**. *Nat. Nanotechnol.* 2011; 6 (1): 13-22.

[2] Liu Z., Tabakman S. M., Chen Z., Dai H. **Preparation of carbon nanotube bioconjugates for biomedical applications**. *Nat. Protocols*. 2009; 4 (9): 1372-81.

[3] Cai D., Mataraza J. M., Qin Z.-H. *et al.* **Highly efficient molecular delivery into mammalian cells using carbon nanotube spearing**. *Nat Meth*. 2005; 2 (6): 449-54.

[4] Kurkina T., Vlandas A., Ahmad A. *et al.* **Label-Free Detection of Few Copies of DNA with Carbon Nanotube Impedance Biosensors**. *Angew. Chem. Int. Ed.* 2011; 50 (16): 3710-4.

[5] Wallace E. J., Sansom M. S. P. **Blocking of Carbon Nanotube Based Nanoinjectors by Lipids: A Simulation Study**. *Nano Lett.* 2008; 8 (9): 2751-6.

[6] Kostarelos K. **The long and short of carbon nanotube toxicity**. *Nat Biotech*. 2008; 26 (7): 774-6.

[7] Li Y. R., **Free Radical Biomedicine: Principles, Clinical Correlations, and Methodologies**, *Bentham Science Publishers*.

[8] Fisher C., Rider A. E., Han Z. J. *et al.* **Applications and Nanotoxicity of Carbon Nanotubes and Graphene in Biomedicine**. *Journal of Nanomaterials*. 2012; 2012: 19.

[9] Liu S., Wei L., Hao L. *et al.* **Sharper and Faster "Nano Darts" Kill More Bacteria: A Study of Antibacterial Activity of Individually Dispersed Pristine Single-Walled Carbon Nanotube**. *ACS Nano*. 2009; 3 (12): 3891-902.

[10] Shi X., von dem Bussche A., Hurt R. H. *et al.* **Cell entry of one-dimensional nanomaterials occurs by tip recognition and rotation**. *Nat. Nanotechnol.* 2011; 6 (11): 714-9.

[11] Poland C. A., Duffin R., Kinloch I. *et al.* **Carbon nanotubes introduced into the abdominal cavity of mice show asbestos-like pathogenicity in a pilot study**. *Nat. Nanotechnol.* 2008; 3 (7): 423-8.

[12] Zhu L., Chang D. W., Dai L., Hong Y. **DNA Damage Induced by Multiwalled Carbon Nanotubes in Mouse Embryonic Stem Cells**. *Nano Lett.* 2007; 7 (12): 3592-7.

[13] Lindberg H. K., Falck G. C. M., Suhonen S. *et al.* **Genotoxicity of nanomaterials: DNA damage and micronuclei induced by carbon nanotubes and graphite nanofibres in human bronchial epithelial cells in vitro**. *Toxicology Letters*. 2009; 186 (3): 166-73.

[14] Donaldson K., Aitken R., Tran L. *et al.* **Carbon Nanotubes: A Review of Their Properties in Relation to Pulmonary Toxicology and Workplace Safety**. *Toxicological Sciences*. 2006; 92 (1): 5-22.

[15] Pasquini L. M., Sekol R. C., Taylor A. D. *et al.* **Realizing Comparable Oxidative and Cytotoxic Potential of Single- and Multiwalled Carbon Nanotubes through Annealing**. *Environmental Science & Technology*. 2013; 47 (15): 8775-83.

[16] Shvedova A. A., Pietroiusti A., Fadeel B., Kagan V. E. **Mechanisms of carbon nanotube-induced toxicity: Focus on oxidative stress**. *Toxicology and Applied Pharmacology*. 2012; 261 (2): 121-33.

[17] Nel A., Xia T., Mädler L., Li N. **Toxic Potential of Materials at the Nanolevel**. *Science*. 2006; 311 (5761): 622-7.

[18] Kang S., Pinault M., Pfefferle L. D., Elimelech M. **Single-Walled Carbon Nanotubes Exhibit Strong Antimicrobial Activity**. *Langmuir*. 2007; 23 (17): 8670-3.

[19] Chen H., Wang B., Gao D. *et al.* **Broad-Spectrum Antibacterial Activity of Carbon Nanotubes to Human Gut Bacteria**. *Small*. 2013; 9 (16): 2735-46.

[20] Kondyurin A., Levchenko I., Han Z. J. *et al.* **Hybrid graphite film–carbon nanotube platform for enzyme immobilization and protection**. *Carbon*. 2013; 65 (0): 287-95.

[21] Han Z. J., Ostrikov K., Tan C. M. *et al.* **Effect of hydrophilicity of carbon nanotube arrays on the release rate and activity of recombinant human bone morphogenetic protein-2**. *Nanotechnology*. 2011; 22 (29): 295712.

[22] Yick S., Han Z. J., Ostrikov K. **Atmospheric microplasma-functionalized 3D microfluidic strips within dense carbon nanotube arrays confine Au nanodots for SERS sensing**. *Chem. Commun.* 2013; 49 (28): 2861-3.

[23] Martins Ferreira E. H., Moutinho M. V. O., Stavale F. *et al.* **Evolution of the Raman spectra from single-, few-, and many-layer graphene with increasing disorder**. *Phys. Rev. B*. 2010; 82 (12): 125429.

[24] Eckmann A., Felten A., Mishchenko A. *et al.* **Probing the Nature of Defects in Graphene by Raman Spectroscopy**. *Nano Lett.* 2012; 12 (8): 3925-30.

[25] Seo D. H., Han Z. J., Kumar S., Ostrikov K. **Structure-Controlled, Vertical Graphene-Based, Binder-Free Electrodes from Plasma-Reformed Butter Enhance Supercapacitor Performance**. *Adv. Energy Mater.* 2013;10.1002/aenm.201300431: n/a-n/a.

[26] H. Ago, T. Kugler, F. Cacialli *et al.* **Work Functions and Surface Functional Groups of Multiwall Carbon Nanotubes**. *Journal of Physical Chemistry B*. 1999; 103 (38): 8116-21.

[27] Park S.-J., Jung W.-Y. **Effect of KOH Activation on the Formation of Oxygen Structure in Activated Carbons Synthesized from Polymeric Precursor**. *Journal of Colloid and Interface Science*. 2002; 250 (1): 93-8.

[28] Zhang W., Carravetta V., Plekan O. *et al.* **Electronic structure of aromatic amino acids studied by soft x-ray spectroscopy**. *The Journal of Chemical Physics*. 2009; 131 (3): 035103.

[29] V. Datsyuk, M. Kalyva, K. Papagelis *et al.* **Chemical oxidation of multiwalled carbon nanotubes**. *Carbon*. 2008; 46 (6): 833-40.

[30] Nikaido H. **Antibiotic Resistance Caused by Gram-Negative Multidrug Efflux Pumps**. *Clinical Infectious Diseases*. 1998; 27 (Supplement 1): S32-S41.

[31] Brady-Estévez A. S., Kang S., Elimelech M. **A Single-Walled-Carbon-Nanotube Filter for Removal of Viral and Bacterial Pathogens**. *Small*. 2008; 4 (4): 481-4.

[32] Kang S., Mauter M. S., Elimelech M. **Physicochemical Determinants of Multiwalled Carbon Nanotube Bacterial Cytotoxicity**. *Environmental Science & Technology*. 2008; 42 (19): 7528-34.

[33] Chen C.-Y., Jafvert C. T. **Photoreactivity of Carboxylated Single-Walled Carbon Nanotubes in Sunlight: Reactive Oxygen Species Production in Water**. *Environmental Science & Technology*. 2010; 44 (17): 6674-9.

[34] Fenoglio I., Tomatis M., Lison D. *et al.* **Reactivity of carbon nanotubes: Free radical generation or scavenging activity?** *Free Radical Biology and Medicine*. 2006; 40 (7): 1227-33.

[35] Pulskamp K., Diabaté S., Krug H. F. **Carbon nanotubes show no sign of acute toxicity but induce intracellular reactive oxygen species in dependence on contaminants**. *Toxicology Letters*. 2007; 168 (1): 58-74.

[36] Deokar A. R., Lin L.-Y., Chang C.-C., Ling Y.-C. **Single-walled carbon nanotube coated antibacterial paper: preparation and mechanistic study**. *Journal of Materials Chemistry B*. 2013; 1 (20): 2639-46.

[37] Tu Y., Lv M., Xiu P. *et al.* **Destructive extraction of phospholipids from Escherichia coli membranes by graphene nanosheets**. *Nat Nano*. 2013; 8 (8): 594-601.

[38] Balasubramanian K., Burghard M. **Chemically functionalized carbon nanotubes**. *Small*. 2005; 1 (2): 180-92.

7

Future Outlook and Conclusion

As I am penning this conclusion, I do not wish to delude myself or the reader into thinking that the finality of this thesis implies that research in the area of CNT-based hybrid nanomaterials have been exhausted. Truly, as I revisit the work which I had labour over the period of my doctoral candidature I see nothing but of the future which is now made possible. Therefore, the last chapter will comprise of a summary of the work presented follow by suggestions of future work.

In this thesis, I have explored the properties and applications of CNT-based hybrid nanomaterials. The fabrication of CNT-based hybrid nanomaterials was a non-trivial process. As it requires deliberate designed so as to ensure the desired attributes of both materials are maximised and that their coupling are complementary. Thus, in order to achieve this delicate balance, a significant portion of this thesis was dedicated to understand the growth of CNTs and the effects of various modification schemes. Despite the additional considerations required to design hybrid nanomaterials, this work further proved that these efforts were worthwhile. Upon their successful integration, CNT-based hybrid material possesses superior performance in a range of applications as compared to the individual constituents.

Prior to discussing CNT-based hybrid nanomaterials, factors which determined the properties of CNTs were presented in Chapter 2. Specifically, the mechanisms regarding to CNT growth and the factors which control the properties of single-walled CNTs were explored. Based on these concepts, I then demonstrated that the density, chirality and the diameter of single-walled CNT networks could be controlled by engineering the catalyst structure. In particular, this was achieved by controlling

catalyst nanoparticle formation though tuning interlayer diffusion. This work generated numerous areas which need to be further explored in the future. Specifically, a better understanding of the deterministic factors affecting nanoparticles formed from interlayer diffusion needs to be determined. Of particular, the role played by grain boundaries and defects within the Al_2O_3 requires more detailed investigation. Furthermore, it will be interesting to see whether other catalyst materials such as cobalt or nickel could also benefit from this tri-layered design. Recently, there were reports showing that the height of vertically aligned multi-walled CNTs could be controlled by the application of an Fe reservoir underneath an alumina buffer publication.[1] I believe that the current tri-layered catalyst structure could also be promising to tune the physical properties of vertically aligned CNTs, both multi-walled and single-walled.

The first CNT-based hybrid nanomaterial presented was a core-shell structure. Such a configuration utilise the morphology of the CNT as a template. In Chapter 3, this was constructed by depositing palladium onto the surface of CNTs. This Pd-CNT hybrid demonstrated reversible hydrogen sensing in room temperature. Future work in this field will centre on optimising the CNT-metal core-shell structure. For example, it will be interesting to see if lengthening of Pd-CNT core shell structure (i.e. increasing the length of CNTs clad by Pd) could result in an improvement to the device performance. It will also be of interest to design core-shell structures based on other metal. This would be beneficial to a range of resistive sensors as both the high conductivity and large surface area of CNT arrays can be better utilised.

Chapter 4 presented a plasma based chemical functionalisation technique. As compared to the common chemical approaches, the atmospheric-pressure plasma jet allowed the modification to be spatially defined. Furthermore, the absences of a dispersion step allow the microstructure of the CNT arrays to be preserved. The potency of this technique was demonstrated by the maskless fabrication of a patterned SERS sensor on CNT arrays. This was achieved by first creating a pattern on the CNT array with the plasma and then decorating that specific region with Au nanoparticles.

Future work will focus on creating complex patterns of different chemical functionality on CNT arrays using the plasma jet. Additionally, the effectiveness of the said technique on other nanostructures such as vertically aligned graphene nanosheets, plasma polymerized nanofilms, and carbon nanodots will also be of interest.[2-4]

In Chapter 5, a hybrid structure based on the direct growth of CNTs on graphene nanosheets was demonstrated and its supercapacitor performance was studied. The complementary integration of the two materials showed a significant enhancement to the device performance. This could be seen by a high specific capacitance of 278 F g^{-1} at 10 mV s^{-1}, which is superior to value normally obtained from either CNTs or graphene alone. Furthermore, the high stability of the hybrid nanostructure was demonstrated by a capacitance retention of >99% after 8,000 charge/discharge cycles at 100 mV s^{-1}. Future work in this direction will focus on increasing the penetration of the CNTs. Currently, the growth of CNTs was limited to a micron depth of the VGNS. This was due to the fact that the catalyst deposition was carried out by a line-of-sight technique (sputtering) and hence could not effectively penetrate the VGNS. The development of a solution based technique to impregnate the VGNS with catalyst particles is highly desirable. Furthermore, the high specific area, good mechanical performance and good conductivity of the hybrid would also make it attractive for a range of other applications such as lithium-ion battery, chemical detection or gas storage. Thus, application apart from supercapacitor should also be explored.

In Chapter 6, the biocompatibility of CNT arrays towards Gram positive and Gram negative bacteria was presented. The work is significant as it delivered a toxicological study based-on a fixed CNT structure rather than CNT dispersed in medium. The results showed that plasma treatment was able to enhance the biocompatibility of the CNT arrays towards Gram positive bacteria; whereas Gram negative bacteria were not affected. This work also commented on the cytotoxic mechanisms commonly attributed to CNTs and acknowledged that a range of factors contributed to the biocompatibility of CNTs. Future work will involve further investigations on the effects of CNT arrays

on other biological activities of the bacteria. In addition, due to their ability to couple with proteins, the activities of enzyme embedded within the CNT arrays should also be investigated. This could lead to the development of next-generation platforms for bio-reactor and tissue scaffolds.

To end this thesis, perhaps it is wise to reconsider why nanoscience, a discipline that is largely invisible to the naked eye and is governed by laws beyond our world should remain relevant. At times, I have been asked why I concern myself with the nanoscopic when we live in a world filled with macroscopic challenges. At the end, progress in science will continue to be intertwined with nanoscience for the simple fact that the world we observe is due to things interacting on the nanoscopic world. Life is a collection of cellular machines responding to molecules it gathers from the environment. Technology comes from electrons being manipulated by its environment and every aspects of a material comes from its atomic arrangement. It is my belief that by gathering knowledge of the nanoscopic world, we could be better equipped to tackle the challenges we face in the current world. For ultimately, which of the problems faced by us today are not due to molecules, atoms and electrons interacting with the world they see?

References

[1] Shawat E., Mor V., Oakes L. *et al.* What is below the support layer affects carbon nanotube growth: an iron catalyst reservoir yields taller nanotube carpets. *Nanoscale*. 2014; 6 (3): 1545-51.

[2] Vasilev K., Sah V., Anselme K. *et al.* Tunable Antibacterial Coatings That Support Mammalian Cell Growth. *Nano Lett.* 2010; 10: 202.

[3] Wang J., Wang C.-F., Chen S. Amphiphilic Egg-Derived Carbon Dots: Rapid Plasma Fabrication, Pyrolysis Process, and Multicolor Printing Patterns. *Angew. Chem. Int. Ed.* 2012; 51: 9297.

[4] Seo D. H., Kumar S., Ostrikov K. Control of morphology and electrical properties of self-organized graphenes in a plasma. *Carbon*. 2011; 49: 4331.